1999

Application of the FDTD method for the analysis of finite-sized phased array microstrip antennas

Javier Gomez Tagle Rangel
University of Central Florida, javiergomeztagle@icloud.com

APPLICATION OF THE FDTD METHOD FOR THE ANALYSIS OF FINITE-SIZED PHASED ARRAY MICROSTRIP ANTENNAS

by

Javier Gómez Tagle Rangel
B.S. Instituto Tecnológico y de Estudios Superiores de Monterrey, 1990
M.S. University of Central Florida, 1996

A dissertation submitted in partial fulfillment of the requirements
for the degree of Doctor of Philosophy
in the Department of Electrical and Computer Engineering
in the College of Engineering
at the University of Central Florida
Orlando, Florida

Summer Term
1999

Major Professor: Dr. Christos G. Christodoulou

ABSTRACT

The Finite-Difference Time-Domain (FDTD) method has gained tremendous popularity in the past decade as a tool for solving Maxwell's equations. Phased Array Antennas find several applications including mobile communications (cellular, personal communication systems and networks), satellite communications, global positioning system (GPS), aeronautical and radar systems. This dissertation describes the application of the FDTD method for calculating broadband characteristics of finite-sized phased array antennas consisting of microstrip elements fed with coaxial probes.

The characterization of such antennas is dependent upon the development of simulation tools that can accurately model general topologies including wires, dielectrics, conductors, lumped elements and metallic strips. The use of these simulation tools reduces the cost and effort associated with fabricating and testing phased array antennas. The FDTD formulation is inherently broadband, very general, and easily accommodates arbitrary conductor geometry and dielectric configurations.

The FDTD method is implemented and applied to determine the input impedance, radiation-patterns and gain of microstrip antennas. Next, the main contributions of this work are described which include the full time-domain characterization of broadband characteristics of finite-sized phased array antennas for different scan conditions. Active reflection coefficient, gain, scan-element patterns and scanning-array radiation patterns are calculated.

This dissertation is dedicated to my mother, Rosa María Rangel de Gómez Tagle, for her truly unconditional love. She taught me my first lessons in life, she is the one that instilled in me an early love for learning, and has continued to teach me my most valuable lessons every day.

To the love of my life, Conchita, who sacrificed considerably to enable me to pursue this work: without her love, understanding and support, I would have been unable to successfully complete this effort.

I wish I could thank my father, Eduardo Gómez Tagle Orbe, whose memory will remain in my heart forever.

ACKNOWLEDGEMENTS

I would like to express my sincere gratitude to Dr. Christos Christodoulou for his guidance, support, and encouragement throughout this project. I would also like to thank Dr. Parveen Wahid and Dr. Amir Mortazawi for the constant support, technical discussions and insights they provided throughout the duration of this work. In addition to serving on my research committee they have been truly excellent teachers. To my friends David and Nina Freeman, for being my family in the United States. Thanks to Eduardo Rodríguez, José Chaverri, Heather Smith and Guilherme Carvalho, for being such good friends. Thanks also go to my friends at the Computational Electromagnetics and Neural Networks Lab in UCF: Ahmed El Zooghby, Mohua Kar, Adam Martin, Toni Ivanov, Marko Rubelj, Tamara Sprekic, Gregory Turner, Mahbub Mohammed, Riad Mahbub, Mir Abul Faiz, Sean Ortiz, Rizwan Bashirulla, Sameh Tawadrous, Sue Huang, Mahfuzul Haque and Jorge Camacho.

I would also like to gratefully acknowledge the sponsors of this research project, which include CONACYT (Consejo Nacional de Ciencia y Tecnología), the Fulbright-García Robles Program, the Florida-Mexico Institute, University of Central Florida, Banco de México and Raytheon E-Systems. Finally, Tom Miles and Angie Wall from Raytheon for believing in me and giving me the opportunity to develop this challenging research project.

TABLE OF CONTENTS

LIST OF FIGURES

1. INTRODUCTION

1.1 Problem Statement and Motivation

The Finite-Difference Time-Domain (FDTD) method has gained tremendous popularity in the past decade as a tool for solving Maxwell's equations. Phased Array Antennas find several applications including mobile communications (cellular, personal communication systems and networks), satellite communications, global positioning system (GPS), aeronautical and radar systems.

This dissertation describes the application of the FDTD method for calculating broadband characteristics of finite-sized phased array antennas consisting of microstrip elements fed with coaxial probes. The objective will be to investigate phased array microstrip antennas, to suggest new implementations of the Finite Difference Time Domain Method for the analysis of finite-sized phased array microstrip antennas and to develop an integrated phased array antenna CAD (Computer Aided Design) tool.

Microstrip patch antennas are low-profile radiators that are typically lightweight, small in size, and conformable to planar and non-planar surfaces. Since patch elements are fabricated using printed-circuit technology, they can be manufactured in large quantities to reduce cost and are compatible with monolithic microwave integrated circuit

(MMIC) designs. These antennas are well suited to applications where an aerodynamic profile and reliable performance are significant constraints. As a result, patch antennas have found numerous applications in aircraft, spacecraft, satellites and missiles.

Before such antennas are fabricated, it is necessary to perform analysis at several stages so that various candidate antennas can be considered viable. The designer proceeds to select a few of such candidate antennas based on both computer-aided performance analysis and cost of fabrication. The final system may be selected based on a trade-off between cost and performance parameters.

The motivation of the work of this dissertation is to develop a computer-aided analysis technique that can be applied to the design and evaluation of an antenna array system. In order to achieve a good design for an array, it is necessary to compute the active reflection coefficient, gain and far-field radiation patterns. Increased mutual coupling has been found to degrade the transient behavior of phased and adaptive arrays and it also affects the isolation between adjacent beams in multiple-beam arrays. The computation of mutual coupling is generally a difficult task, because there is no simple calculation that can yield reasonably acceptable information. Therefore it will be very important to accurately compute the mutual coupling between array elements.

1.2 Solution Approaches and Past Research

In determining which technique to use in modeling finite-sized phased array antennas, it is useful to consider the different methodologies available. These methods are divided into the following categories: empirical models, semi-empirical models and full-wave models.

The empirical models are generally based on some fundamental simplifying assumptions concerning the radiation mechanism of the antenna. The assumptions are extracted from experimental experience. Phenomena such as surface wave propagation and dispersion are generally not included in these models. The importance of empirical models in providing a qualitative idea about the antenna's behavior and at least a first-order solution to a design problem cannot be denied. Among these models are the Transmission Line Model (TLM) and the Cavity Model.

Semi-empirical models are a hybrid of empirical and full-wave analyses. The analytical and computational complexity involved is more than that of the empirical models and less than the full-wave models, and the effects of surface wave modes are taken into account in many of these models. The various models included in this category are: Variational approach, Generalized variational approach, Dual integral equation approach, Electric surface current model, Hankel transform technique, Reciprocity method and Generalized edge boundary condition technique.

The Full-Wave Analyses include formulations that are electromagnetically rigorous (no empirical or semi-empirical assumptions are made) as well as computationally extensive. The most common numerical techniques are the Method of Moments (MOM), the Finite-Difference technique and the Finite Elements Method (FEM). Each one of these approaches can be implemented in the time-domain and the frequency domain, and can be used to obtain the radiation-pattern, gain and input impedance (for radiation problems), as well as the scattering-pattern, gain and radar cross section (for scattering problems).

For this work, the finite-difference method in the time domain (FDTD) method will be used. Such technique has been chosen for the following reasons:

a) The finite-difference method can accommodate very general and intricate modeling requirements.

b) When the geometrical and material configuration becomes very complex, the algorithm complexity remains low. This is particularly true when modeling highly inhomogeneous dielectric objects.

c) Such algorithm requires O(N) storage for N unknowns. This is in contrast to finite element and moment method techniques which require storing a matrix consisting of $O(N^2)$ entries.

d) This technique does not require a linear system solution (matrix inversion).

e) Because it is a time-domain technique, it can predict the transient response to a system. When this transient data is transformed to the frequency domain, it translates into a wide-band system response.

The advent of high-speed, large-memory personal and supercomputer systems has made possible the development of accurate electromagnetic algorithms such as the FDTD method. This method solves Maxwell's time-dependent equations directly in the time domain by converting them into finite-difference equations. The finite difference-equations are then solved in a time marching sequence by alternately calculating the electric and magnetic field components on an interlaced spatial grid.

Yee introduced the first FDTD algorithm to the electromagnetic community in 1966. Since then, the algorithm has been used in electromagnetic wave scattering both in the time and frequency domains, electromagnetic interactions with biological tissues,

antenna radiation and microwave circuit design, among several other applications. Research efforts in the area of the FDTD method are currently directed toward advancing its capabilities with parallel algorithms that can be used in parallel and distributed computers.

FDTD has gained popularity in the last decade because it is able to deliver results in a wide frequency range in a single program run, unlike the frequency domain methods like MOM and FEM that deliver results on a frequency-by-frequency basis. A lot of research has been focused on the analysis of infinite arrays in the past, using Floquet boundary conditions around a reference element and assuming a periodic structure that is infinite in extent along the axes of the array. However, an infinite array does not account for the edge effects of a small array.

1.3 Main Contributions and Organization of the Dissertation

The emphasis and main contribution of this dissertation is on the use of a full-time domain technique that employs FDTD to analyze finite-sized linear and planar arrays with stacked microstrip elements, linear or circular polarization. Different configurations can be designed, therefore the need to address the design of rectangular and circular geometry, as well as rectangular and triangular lattices for the array shape. The radome covering will be reduced to the case of a dielectric covered microstrip antenna, where the dielectric layer thickness is larger than the cell-size used to divide the FDTD computational domain into discrete cells. Radiation pattern and active impedance calculations for both linear and circular polarization stacked microstrip arrays will be the main focus of this research.

A simple CAD program was created with analysis features that are not present in commercial phased array antenna simulators, being the most significant the broadband analysis of phased array microstrip antennas. The development of an input / output user interface for the simulation tool is very important to allow any engineer to use the software. The interface was designed for visualization purposes and to perform calculations related with the FDTD method. In order to have an "Integrated Phased Array Antenna Analysis Software" two interfaces were developed using MATLAB. The FDTD algorithm was implemented using the C programming language.

The interfaces fulfill two purposes:

a) Create a text file that contains all the parameters the FDTD program needs in order to run. The inputs are given interactively by the user. The interface must be able to translate the geometrical and functional characteristics of the array into the kind of parameters that are used by the FDTD code. This part is labeled as the "pre-processing" module. The fact that the FDTD method is being used becomes transparent to the user.

b) Read the text files created by the FDTD code and display plots of time domain voltages and currents, scattering parameters, input impedance and radiation patterns. This part is called the "post-processing" module.

Moreover, the FDTD program must be easily executed, and must use the computer memory efficiently. This issue becomes more critical when large array antennas are analyzed, since memory size becomes a limitation factor. Dynamic memory allocation and other programming techniques are used to achieve this task.

The computer program is able to perform the following tasks:

1) Analyze rectangular or circular microstrip antennas fed with one or two coaxial probes (up to two microstrip patches and three dielectric layers). Both probes can be active or one can be matched to 50 ohms. The conductors are assumed to be perfect electric conductors, but the dielectric materials can be lossy.

2) Feed the upper or lower microstrip patch.

3) Analyze linear or planar array antennas (either active arrays or feed the reference element and match the other elements to 50 ohms).

4) Rectangular Lattice configuration for planar array.

5) Use "infinite" or finite (truncated) dielectric layers. An infinite ground plane is assumed.

6) Use a full time domain approach to analyze linear, dual linear or circularly polarized phased array microstrip antennas.

7) Calculate broadband radiation characteristics of the phased array antenna from the scan element patterns.

The process of validating the functionality and capability of the simulation tool was a long process, since we had to analyze the quality of the results predicted using the program, compare with measurements, detect errors and possible limitations.

The FDTD simulator uses the three-dimensional FDTD method combined with time domain techniques to solve for the transient electric and magnetic fields in the microstrip antenna, and a Fast Fourier Transform to obtain the frequency response. Broadband results can be obtained in a single computer run. A Discrete Fourier Transform is used to perform the near to far field transformation.

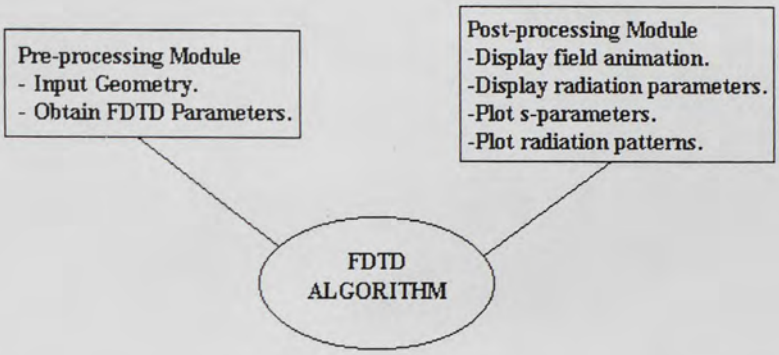

Figure 1. Basic Modules of the Integrated Phased Array Antenna Simulation Tool.

The dissertation is organized into two major parts, each of which represents the subjects that are being studied: microstrip antennas / FDTD, phased array antennas / FDTD. Chapters 2 to 5 represent the work involving the FDTD simulations of the isolated microstrip antenna elements. Chapters 2 and 3 explain the background necessary to understand microstrip antennas, phased arrays and FDTD. Chapter 4 focuses specifically on the FDTD formulation, with special attention given to the contributions for the feed model and the absorbing boundary conditions. Chapter 5 illustrates several comparisons of the FDTD computations with results obtained from measurements. Stacked rectangular or circular microstrip antenna elements can be used, feeding the lower or upper patch, single or dual coaxial feed. The actual application of the full-time domain algorithm to finite-sized phased array antennas is then presented in Chapter 6. This chapter provides computational as well as experimental results for three different array topologies.

Chapter 7 is devoted to the examination of results of the finite-sized phased array antennas. The goal of this chapter is to present a mathematical formulation of the method

and highlight its advantages and disadvantages. Because this algorithm has been explored in conjunction with the infinite array approximation solution, a qualitative comparison of the relative performance of the two techniques will be presented. Computational examples will also be shown which illustrate the accuracy and flexibility of the proposed method.

Finally, Chapter 8 presents conclusions and ideas for future research directions. At the end of this dissertation, detailed appendices are presented to support the developments provided in the chapters.

2. BACKGROUND

2.1 Microstrip Antennas

Microstrip patch antennas can be shaped in a variety of configurations including rectangular, circular, elliptical and triangular. Figure 2 depicts the geometry of a rectangular microstrip patch antenna.

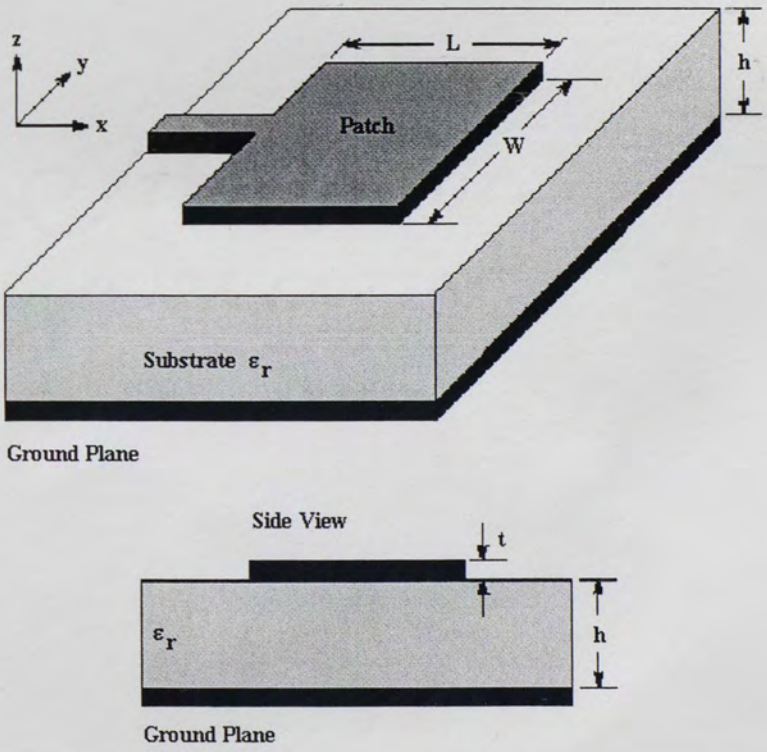

Figure 2. Geometry of a rectangular microstrip patch antenna.

The patch element shown in Figure 2 uses a microstrip line feed. This is one of a number of feed arrangements that can be used with microstrip antennas. Figure 3 illustrates some of the more popular feed arrangements. The offset microstrip line feed eases the task of matching since the offset depth controls the input impedance of the antenna. Additionally, this configuration is simple to fabricate and lends itself well to analytical modeling. However, the feed line radiates and causes pattern and polarization degradation. The coaxial feed reduces spurious feed radiation and is easy to construct and match, although it tends to have a narrow bandwidth and is difficult to model analytically. The aperture-coupled feed isolates the feed mechanism from the radiating element through the use of a ground plane. Energy from the feed line is coupled to the element patch through the aperture slot. Unfortunately, the ground plane makes this feed configuration quite difficult to manufacture. Finally, the proximity-coupled feed removes the ground plane so it is easier to manufacture than the aperture-coupled feed. It has low spurious radiation, is fairly easy to analyze, and provides the largest bandwidth of the feed configurations presented here.

The transmission-line model is the simplest technique and, as a result, the least accurate. The microstrip antenna is modeled as two radiating slots that are separated by a distance L_{eff}, which is essentially the length of the patch L plus an additional distance $2\Delta L$ that accounts for the fact that the patch looks electrically wider due to the fringing fields. The added distance can be calculated from

$$\Delta L = 0.412 \cdot h \cdot \frac{\left(\varepsilon_{reff} + 0.3\right)\left(\frac{W}{h} + 0.12\right)}{\left(\varepsilon_{reff} - 0.258\right)\left(\frac{W}{h} + 0.8\right)} \tag{1}$$

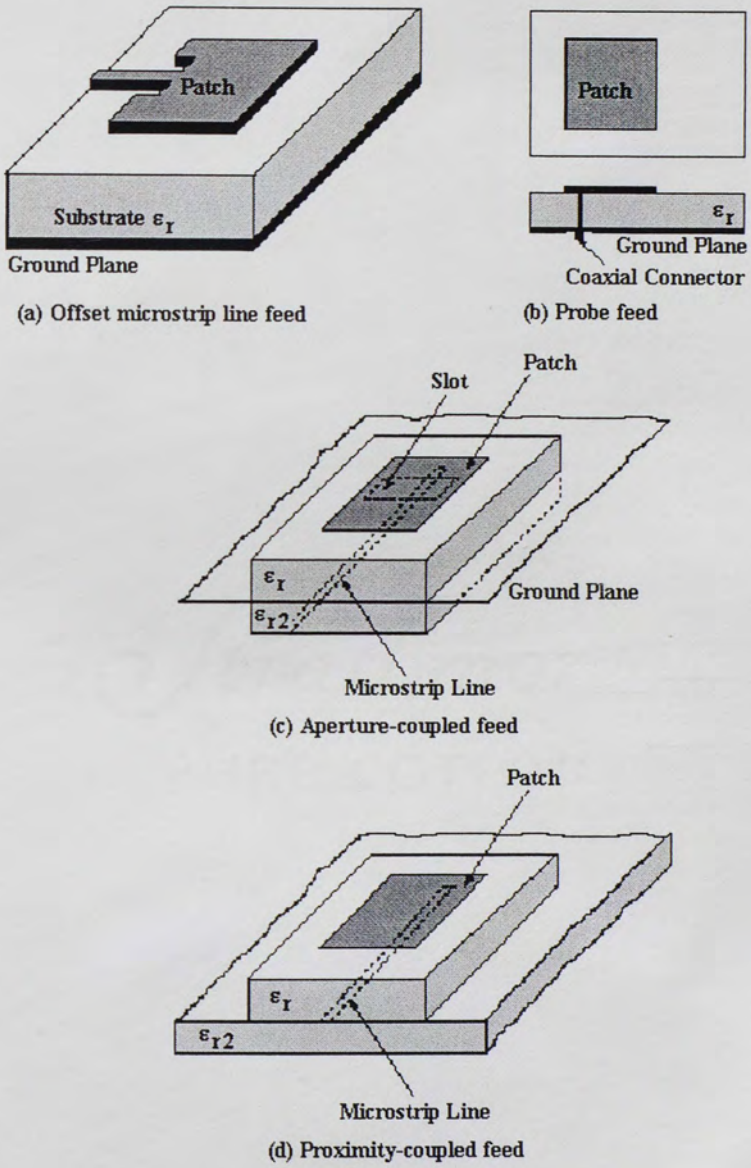

Figure 3. Feed configurations for microstrip patch antenna.

In the above equation, ε_{eff} is the effective dielectric constant of a microstrip transmission line given by [2]

$$\varepsilon_{reff} = \frac{\varepsilon_r + 1}{2} + \frac{\varepsilon_r - 1}{2}\left(1 + 12 \cdot \frac{h}{W}\right)^{-1/2} \tag{2}$$

Thus, the effective distance separating the two radiating slots becomes

$$L_{eff} = L + 2 \cdot \Delta L \tag{3}$$

Finally, this adjusted length is used to calculate the resonant frequency of the antenna where c is the speed of light in a vacuum [2-5].

$$(f_r)_{010} = \frac{c}{2 \cdot L_{eff} \cdot \sqrt{\varepsilon_{eff}}} \tag{4}$$

Since the transmission-line model accounts for the fringing effects at the edges of the patch, it provides a good characterization of the resonant frequency. It also models the input impedance of the antenna fairly accurately. However, it does not account for the affects of a truncated dielectric substrate or a finite ground plane nor does it provide insight into the radiation patterns of the antenna. Additionally, the model breaks down as the height of the dielectric substrate, *h*, becomes a significant portion of a wavelength.

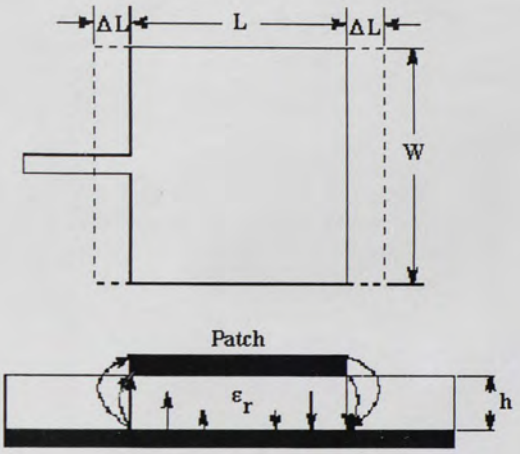

Figure 4. Transmission line model.

In order to gain insight into the radiating mechanism of an antenna, we need to first understand the near-field quantities that are present on the structure. The cavity model aids in this pursuit since it provides a mathematical solution for the electric and magnetic fields of a microstrip antenna. It does so by using a dielectric loaded cavity to represent the antenna. As we can see in Figure 5, this technique models the dielectric material assuming that it is truncated at the edges of the patch. The patch and ground-plane are represented with perfect electric conductors and the edges of the substrate are modeled with perfectly conducting magnetic walls. It should be noted that the cavity model does not include feed effects; the feed is shown in the figure simply for reference.

Assuming that the dielectric is very thin, which means that the electric field is constant along the height of the substrate h, and is nearly normal to the surface of the patch. Therefore, we only need to consider TM_z modes inside the cavity. Now, we can

write an expression for the electric and magnetic fields within the cavity in terms of the vector potential A_z:

$$
\begin{aligned}
E_x &= -j\frac{1}{\omega\mu\varepsilon}\frac{\partial^2 A_z}{\partial x \partial z} & H_x &= \frac{1}{\mu}\frac{\partial A_z}{\partial y} \\
E_y &= -j\frac{1}{\omega\mu\varepsilon}\frac{\partial^2 A_z}{\partial y \partial z} & H_y &= \frac{1}{\mu}\frac{\partial A_z}{\partial x} \\
E_z &= -j\frac{1}{\omega\mu\varepsilon}\left(\frac{\partial^2}{\partial z^2} + k^2\right)A_z & H_z &= 0
\end{aligned}
\tag{5}
$$

Since the vector potential must satisfy the homogeneous wave equation we can use separation of variables to write the following general solution

$$
\begin{aligned}
A_z = &\left[A_1 \cos(k_x x) + B_1 \sin(k_x x)\right] \cdot \left[A_2 \cos(k_y y) + B_2 \sin(k_y y)\right] \\
&\cdot \left[A_2 \cos(k_y y) + B_2 \sin(k_y y)\right]
\end{aligned}
\tag{6}
$$

where k_x, k_y, and k_z are the wave-numbers. Applying the boundary conditions

$$
\begin{aligned}
E_x = 0 \text{ for } 0 \le x \le L,\ 0 \le y \le W,\ z = 0 \\
\text{and } 0 \le x \le L,\ 0 \le y \le W,\ z = h \\
H_x = 0 \text{ for } 0 \le x \le L,\ y = 0,\ 0 \le z \le h \\
\text{and } 0 \le x \le L,\ y = W,\ 0 \le z \le h \\
H_y = 0 \text{ for } x = 0,\ 0 \le y \le W,\ 0 \le z \le h \\
\text{and } x = L,\ 0 \le y \le W,\ 0 \le z \le h
\end{aligned}
\tag{7}
$$

renders a solution for the electric and magnetic fields inside the cavity is:

$$E_x = -j\frac{k_x k_y}{\omega\mu\varepsilon} A_{mnp} \sin(k_x x)\cos(k_y y)\sin(k_z z)$$

$$E_y = -j\frac{k_y k_z}{\omega\mu\varepsilon} A_{mnp} \cos(k_x x)\sin(k_y y)\sin(k_z z)$$

$$E_z = -j\frac{(k^2 - k_z^{\ 2})}{\omega\mu\varepsilon} A_{mnp} \cos(k_x x)\cos(k_y y)\cos(k_z z) \qquad (8)$$

$$H_x = -j\frac{k_y}{\mu} A_{mnp} \cos(k_x x)\sin(k_y y)\cos(k_z z)$$

$$H_y = -j\frac{k_x}{\mu} A_{mnp} \sin(k_x x)\cos(k_y y)\cos(k_z z)$$

$$H_z = 0$$

$$k_x = \frac{m\pi}{L}, m = 0,1,2...$$

$$k_y = \frac{n\pi}{W}, n = 0,1,2... \qquad m = n = p \neq 0 \qquad (9)$$

$$k_z = \frac{p\pi}{h}, p = 0,1,2...$$

and A_{mnp} is the amplitude coefficient. Finally, the resonant frequencies for the cavity are

$$(f_r)_{mnp} = \frac{1}{2\pi\sqrt{\mu\varepsilon}}\sqrt{\left(\frac{m\pi}{L}\right) + \left(\frac{n\pi}{W}\right)^2 + \left(\frac{p\pi}{h}\right)^2} \qquad (10)$$

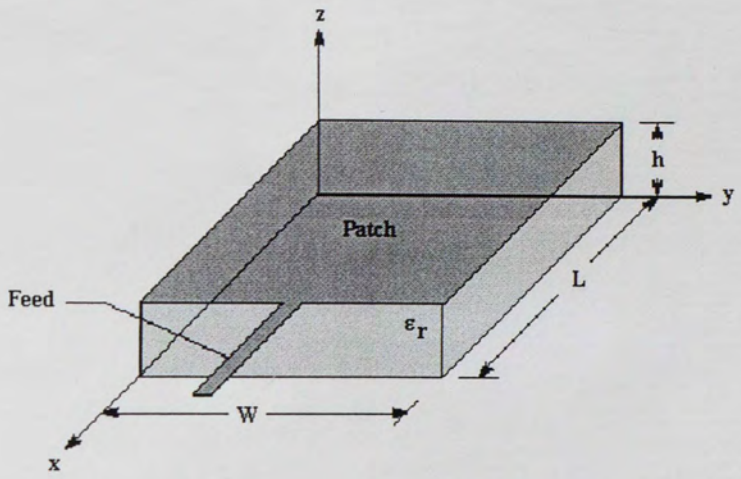

Figure 5. Geometry of cavity model.

Examining the above fields for TM_{100}^{z} dominant mode excitation, we see that $k_y = k_z = 0$ and the field components reduce to

$$E_z = -j\omega A_{100} \cos\left(\frac{\pi}{L}x\right)$$
$$H_y = \frac{\pi}{\mu L} A_{100} \sin\left(\frac{\pi}{L}x\right) \tag{11}$$

We can convert to equivalent electric and magnetic current densities using:

$$\vec{J} = \hat{n} \times \vec{H}$$
$$\vec{M} = -\hat{n} \times \vec{E} \tag{12}$$

where $\hat{n}$ is the outward directed surface normal. The magnetic field is zero along the $x=0$ and $x = L$ walls and is normal to the surface along the $y = 0$ and $y = W$ walls. Therefore, no equivalent electric current density flows on the walls of the cavity. The electric field results in a non-zero magnetic current density on the walls of the cavity. Figure 6 shows both the electric field and corresponding magnetic current densities for the microstrip antenna. The magnetic currents can be broken into a pair of radiating slots and a pair of non-radiating slots. The radiating slots are in phase so they will constructively interfere in the far-field. Thus, these two slots form the primary radiating mechanism for the microstrip antenna. On the other hand, the non-radiating slots are out of phase so they will destructively interfere in the far-field and will not contribute to the radiated fields.

From the above results, it is clear that the cavity model provides excellent insight into the radiating mechanism of a microstrip patch antenna. It provides the field configurations of the radiating and non-radiating slots that can be used to solve for the radiation patterns. Since the antenna is modeled as a cavity, additional work is necessary to accurately model the input impedance.

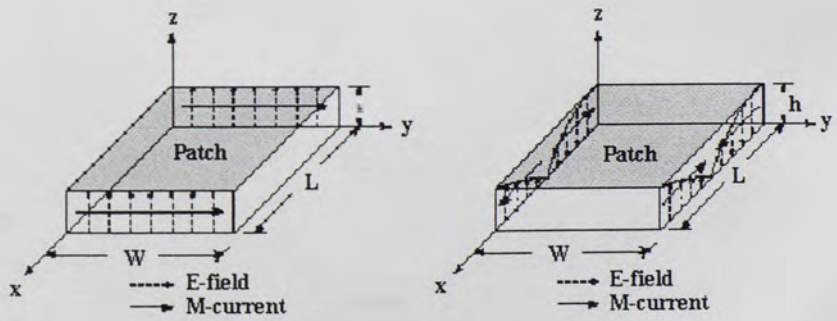

(a) Radiating slots

(b) Non-radiating slots

Figure 6. Field configurations and current densities for microstrip patch.

An effective loss tangent needs to be added to account for the power that is lost to radiation. Alternatively, the radiated energy can be modeled using an impedance boundary condition at the walls [2,4]. Although the cavity model is quite adept at modeling the radiating mechanism for a microstrip antenna, it does have some limitations. First, the cavity model does not model the feed effects. Nor does it model the adverse effects introduced by a finite substrate and ground plane. One way to circumvent these limitations is to employ numerical techniques.

2.2 Phased Array Antennas

A phased array antenna is composed of a group of individual radiators that are distributed in a linear or two-dimensional spatial configuration. The amplitude and phase excitations of each radiator can be individually controlled to form a radiated beam of any desired shape (directive pencil-beam or fan-beam shape). The position of the beam in space is controlled electronically by adjusting the phase of the excitation signals at the individual radiators. Hence, beam scanning is accomplished with the antenna aperture remaining fixed in space without the involvement of mechanical motion in the scanning process [6-15].

The array factor of a two-dimensional array (general case that includes the linear array) may be calculated by summing the vector contribution of each element in the array at each point in space. The array factor can be written in terms of the directional cosines, $cos\alpha_x$ and $cos\alpha_y$ of the spherical coordinate system as [6-15]:

$$E_a(\theta,\phi) = \sum_{m=1}^{M}\sum_{n=1}^{N} i_{mn} e^{jk(m\cdot d_x\cdot cos\alpha_x + n\cdot d_y\cdot cos\alpha_y)}$$
$$cos\alpha_x = sin\theta\, cos\phi \qquad (13)$$
$$cos\alpha_x = sin\theta\, sin\phi$$

Beam scanning with planar arrays is accomplished by linear phasing along both array coordinates. To scan the beam to the angular position corresponding to the directional cosines $cos\alpha_{xo}$ and $cos\alpha_{yo}$, a linear phase taper is introduced at each element so that the excitation at the (m, n) element is given by:

$$i_{mn} = a_{mn} e^{-jk(m\cdot d_x\cdot cos\alpha_{xo} + n\cdot d_y\cdot cos\alpha_{xo})} \qquad (14)$$

$k\cdot d_x\cdot cos\alpha_{xo}$ is the element to element phase shift in the x-direction and $k\cdot d_y\cdot cos\alpha_{yo}$ is the element to element phase shift in the y-direction.

This form of steering phase indicates that the phase of the element (m, n) is the sum of a row phase $m\cdot k\cdot d_x\cdot cos\alpha_{xo}$ and a column phase $n\cdot k\cdot d_y\cdot cos\alpha_{yo}$. For a rectangular planar array with M by N elements, the array factor is [2,6]:

$$E_a(\theta,\phi) = \sum_{m=1}^{M}\sum_{n=1}^{N} i_{mn} e^{jk[m\cdot d_x\cdot(cos\alpha_x - cos\alpha_{xo}) + n\cdot d_y\cdot(cos\alpha_y - cos\alpha_{yo})]} \qquad (15)$$

The array factor of the planar array has an infinite number of grating lobes in the directional cosine space. For example, a local-maximum of E_a occurs whenever its

argument is a multiple of 2π. Since there is a one-to-one correspondence between the directional-cosine-space ($cos\alpha_x$ and $cos\alpha_x$) and the visible-space (θ and ϕ space with the boundary defined by ($cos^2\alpha_x + cos^2\alpha_y = 1$), the number of grating lobes that can be projected from the directional cosine space into the visible space depends upon the parameters $\frac{d_x}{\lambda}$ and $\frac{d_y}{\lambda}$. To avoid the formation of grating lobes in the visible space, the element spacing $\frac{d_x}{\lambda}$ and $\frac{d_y}{\lambda}$ must be chosen so that there is only one maximum from the equation of E_a, namely, the main beam, in the visible space (real space) [2,6].

In the planar array, the element lattice and spacing can be chosen to shape the grating-lobe contour (location pattern of grating lobes) to fit the required scanning volume so that the total required number of elements in the planar array is minimized. To accomplish this optimization, it is more convenient to plot the position of the grating lobes when the main beam is phased for broadside and observe the motion of these lobes as the beam is scanned.

A planar array with rectangular lattice configuration is depicted in Figure 7. The distance between the elements in the y-direction is d_y and the distance in the x-direction is d_x.

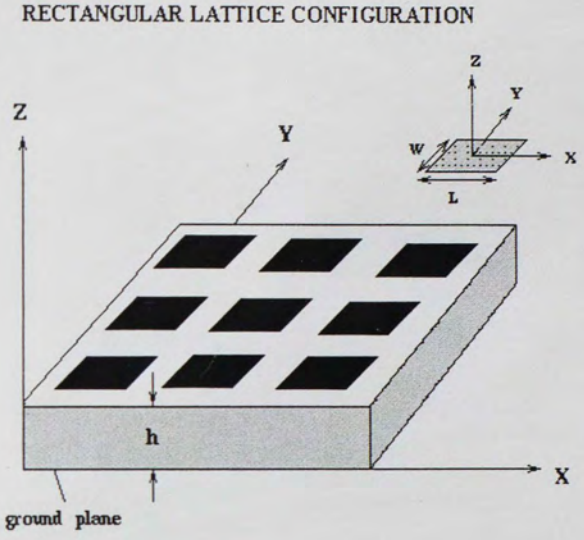

Figure 7. Rectangular Lattice Configuration.

For a *rectangular lattice*, the grating lobes are located at

$$\begin{aligned} cos\alpha_x - cos\alpha_{xo} &= \pm\lambda \cdot \frac{p}{d_x} \\ cos\alpha_y - cos\alpha_{yo} &= \pm\lambda \cdot \frac{q}{d_y} \\ p,q &= 0,1,2... \end{aligned} \tag{16}$$

Only the portion of the pattern inside a unit circle centered at $cos\alpha_x = cos\alpha_y = 0$ lies in visible space. The lobe at $p = q = 0$ is the main beam [6].

A planar array with triangular lattice configuration is depicted in Figure 8. The distance between the elements in the y-direction is d_y and the distance in the *x*-direction is $2d_x$.

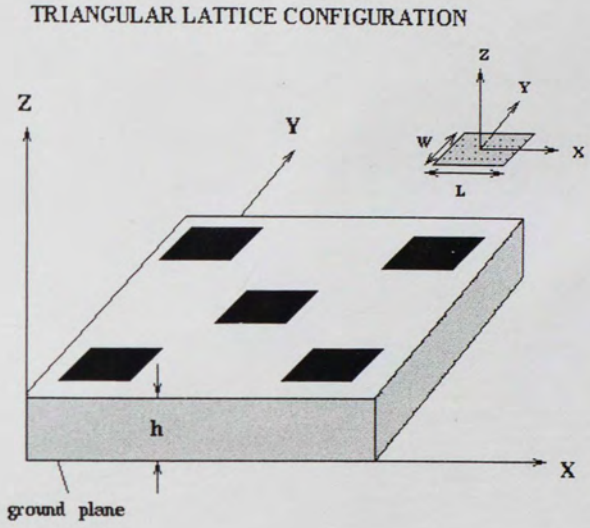

Figure 8. Triangular Lattice Configuration.

For a conical scan volume, the *triangular lattice* is more efficient for the suppression of grating lobes than a rectangular grid, so that for a given aperture size fewer elements are required. If the triangular lattice contains elements at $m \cdot d_x$ and $n \cdot d_y$ where $m + n$ is even, then the grating lobes are located at

$$\begin{aligned} \cos\alpha_x - \cos\alpha_{xo} &= \pm\lambda \cdot \frac{p}{2d_x} \\ \cos\alpha_y - \cos\alpha_{yo} &= \pm\lambda \cdot \frac{q}{2d_y} \\ p + q &= even - number \end{aligned} \tag{17}$$

As the array is scanned away from broadside, each grating lobe (in the directional cosine space) will move a distance equal to the sine of the angle of scan and in a direction that is determined by the plane of scan. To ensure that no grating lobes enter visible space, the element spacing must be chosen so that for the maximum scan angle θ_m the movement of a grating lobe $sin\ \theta_m$ does not bring the grating lobe into visible space.

If a specific scan angle θ_m from broadside is required for every plane of scan, no grating lobe may exist within a circle of radius $1 + sin\ |\theta_m|$. The square lattice that meets this requirement has [6]:

$$\frac{\lambda}{d_x} = \frac{\lambda}{d_y} = 1 + sin|\theta_m| \tag{18}$$

The area per element is $d_x \cdot d_y$. For an equilateral triangular lattice, the requirement is satisfied by [6]

$$\frac{\lambda}{d_y} = \frac{\lambda}{\sqrt{3}d_y} = 1 + sin|\theta_m| \tag{19}$$

The area per element is $2 \cdot d_x \cdot d_y$. Therefore, for the same amount of grating lobe suppression there is a saving in the number of elements for the triangular versus the rectangular lattice, specified by $\frac{1 - A_R}{A_T}$ percent (A_R = Area Rectangular Lattice, A_T =

Area Triangular Lattice). The planar array with rectangular lattice is composed of elements spaced d_x and d_y, while the array with triangular lattice has an element spacing of $2d_x$ in the x-direction (base of the equilateral triangle) and d_y in the y-direction (height of the equilateral triangle).

The array gain of the antenna is given by [6]:

$$G(\theta_o,\phi_o) = \frac{4\pi A \eta \cos\theta_o [1 - |\Gamma(\theta_o,\phi)|^2]}{\lambda^2} \tag{20}$$

The amplitude of the array aperture reflection coefficient at the scan angle (θ_o, ϕ_o) is $|\Gamma(\theta_o,\phi_o)|^2$, A is the physical area of the array and η is the taper efficiency or illumination efficiency.

The discussion given above is for radiators with isotropic patterns. However, the radiation patterns of real radiators are non-isotropic, and the impedance of the radiators varies as a function of scan caused by the mutual coupling between the radiators. In fact, the pattern of an element in the environment of an array is markedly different from the pattern of an isolated element in amplitude, phase and polarization as well.

One of the functions performed by the antenna is to provide a good match between the transmitter and free space. This means that the radiation impedance (driving-point impedance) looking into the radiators in the array environment must be matched to their generator impedances. If the antenna aperture is not matched to free space, power will be reflected back toward the generator, resulting in a loss in radiated power. In

addition, a mismatch produces standing waves on the feed line to the antenna. The voltage at the peaks of these standing waves is $(1 + |\Gamma|)$ times greater than the voltage of a matched line, where Γ is the voltage reflection coefficient of the radiation impedance. This corresponds to an increased power level that is $(1+|\Gamma|)^2$ times as great as the actual incident power. Therefore, while the antenna is radiating less power, individual components must be designed to handle more peak power. In a scanning array, the impedance of a radiating element varies as the array is scanned, and the matching problem is considerably more complicated. In some instances, spurious lobes may appear in the array pattern as a consequence of the mismatch. Furthermore, there are conditions in which an antenna that is well matched at broadside may have some angle of scan at which most of the power is reflected (*blind angle*) [6].

The mutual-coupling effect on the radiation impedance occurs when the coupled vector-signals add to produce a wave traveling toward the generator of the reference element, which appears to be a reflection from that element. As the phases of the neighboring elements are varied to scan the beam, the vector sum of the coupled signals changes and causes an apparent change in the impedance of the reference radiator. For some scan angles, the coupled voltages will tend to add in phase, causing a large reflection and possibly the loss of the main beam. Large reflections often occur at scan angles just prior to the emergence of a grating lobe into visible space, but in some instances such reflections may occur at smaller scan angles.

For an array with independently driven elements, the far-field array pattern at any angle (θ,ϕ) is obtained by vector addition of the contributions from all the elements at

that angle with each single element driven one at a time while the others are terminated in their generator impedances. The far-field *active-array* pattern is given by [6]:

$$E(\theta,\phi) = \sum_{m=1}^{M}\sum_{n=1}^{N} I_{mn} E_{e,mn}(\theta,\phi) e^{jk[m\cdot d_x(\sin\theta\cos\phi - \sin\theta_o\cos\phi_o) + n\cdot d_y(\sin\theta\sin\phi - \sin\theta_o\sin\phi_o)]} \qquad (21)$$

The *active-element pattern* $E_{e,mn}(\theta,\phi)$ is obtained when only the (m, n) element is driven, with all other elements terminated in their usual generator impedance. I_{mn} is the current in amperes that would be flowing in the (m, n) feed line if all other elements were passively terminated in their usual generator impedance. The utility of these definitions arises from the fact that both computationally and experimentally one driven element in a passively terminated array is easier to cope with than all elements simultaneously driven. Furthermore, the active-element pattern has the significance of describing the array gain as a function of beam-scan angle.

The active-element pattern $E_{e,mn}(\theta,\phi)$ is actually the pattern of the entire array when the excitation of the array is that due to the mutual couplings from the (m, n) element to all the neighboring elements. It is a function of the particular radiator configuration and also, of the relative location of the driven radiator with respect to the other elements of the array. The ideal active-element pattern for a perfectly matched array is a cosine pattern. In general, the expressions of the active-element patterns $E_{e,mn}(\theta,\phi)$ for any radiator type are quite complicated, nevertheless they can be individually measured or numerically calculated. Fortunately, this individual active-element pattern

measurement is not usually necessary if the array is regularly spaced. For an infinite array of regularly spaced elements, every element in the array sees exactly the same environment and all the elements have the same active-element pattern. This approximation can be used for arrays with a large number of elements; the reason for this is that, in practice, the mutual coupling between the radiators decays as $1/x^2$ where x is the distance between the radiators. All the elements with the exception of the edge elements in the array behave as though they are in an infinite-array environment. For larger arrays, the effect of edge elements on array performance is negligible [6].

3. FDTD FUNDAMENTALS

The Finite Difference Time Domain (FDTD) Method is rapidly becoming one of the most widely used numerical methods for electromagnetic fields. There are several reasons for this, including the increased availability of low cost but powerful computers, and the relative simplicity of the FDTD fundamentals that are easier to understand than traditional frequency-domain approaches. Yet, FDTD is capable of computing electromagnetic interactions for any complicated geometry including penetrable dielectric and magnetic materials that are extremely difficult to analyze by other methods. Of the many approaches to electromagnetic computation, including the method of moments (MOM), Finite Elements Method (FEM), Geometric Theory of Diffraction (GTD) and Physical Optics (PO), the FDTD technique is applicable to the wider scope [16].

3.1 FDTD Introduction

FDTD is a discrete representation of Maxwell's equations using a central difference scheme in both time and space. To simulate the wave propagation in three dimensions, Yee's original algorithm (also called leapfrog algorithm) can be adopted. Maxwell's equations are replaced by a system of finite difference equations. The differential time domain Maxwell equations needed to specify the field behavior over time of linear, isotropic, non-dispersive materials are [16,17]:

$$\nabla \times \vec{E} = -\frac{\partial \vec{B}}{\partial t} - \vec{J}_m$$
$$\nabla \times \vec{H} = -\frac{\partial \vec{D}}{\partial t} + \vec{J}_e$$
$$\nabla \cdot \vec{D} = \rho \qquad (22)$$
$$\nabla \cdot \vec{B} = 0$$
$$\vec{D} = \varepsilon \vec{E}, \vec{B} = \mu \vec{H}$$

$\vec{E}$ is the electric field vector in volts per meter. $\vec{D}$ is the electric flux density vector in coulombs per square meter. $\vec{H}$ is the magnetic field vector in amperes per meter. B is the magnetic flux density vector in Weber per square meter. $\vec{J}_e$ is the electric conduction current density in Ampere per square meter. $\vec{J}_m$ is the equivalent magnetic conduction current density in Volt per square meter.

The FDTD formulation is based on two coupled-curl-equations in time domain derived from Maxwell's equations [16,17]:

$$\frac{\partial \vec{H}}{\partial t} = -\frac{1}{\mu}\left(\nabla \times \vec{E} + \sigma^* \vec{H}\right)$$
$$\frac{\partial \vec{E}}{\partial t} = -\frac{1}{\varepsilon}\left(\nabla \times \vec{H} + \sigma \vec{E}\right) \qquad (23)$$

Here, μ is the magnetic permeability in henrys per meter, ε is the electric permitivity in farads per meter and σ is the electric conductivity in siemens per meter. The electric current $\vec{J}_e = \sigma \vec{E}$ has used to allow for lossy dielectric materials, and the

magnetic current $\vec{J}_m = \sigma \vec{H}$ has been included to have the possibility of magnetic loss by adding an equivalent magnetic resistivity term σ^* in ohms per meter.

The formulation only treats the electromagnetic fields *E* and *H*, and not the fluxes *D* and *B*. All four constitutive parameters ε, μ, σ, and σ^* are present so that any linear isotropic material property can be specified. It can be easily shown (taking the divergence of the curl equations) that it is only needed to consider the curl equations because the divergence equations are contained in them. While the divergence equations are not part of the FDTD formalism they can be used as a test on the predicted field response, so that after forming $D = \varepsilon E$ and $B = \mu H$ from the predicted fields, the resulting *D* and *B* must satisfy the divergence equations [16,17].

Writing the vector components of the curl operators, yields the following system of six coupled scalar equations equivalent to Maxwell's curl equations in three-dimensional rectangular coordinate system (x, y, z), that form the basis of the FDTD numerical algorithm for electromagnetic wave interactions with general three-dimensional objects [16,17]:

$$\begin{aligned}
\frac{\partial H_x}{\partial t} &= \frac{1}{\mu}\left(\frac{\partial E_y}{\partial z} - \frac{\partial E_z}{\partial y} - \sigma^* H_x\right) \\
\frac{\partial H_y}{\partial t} &= \frac{1}{\mu}\left(\frac{\partial E_z}{\partial x} - \frac{\partial E_x}{\partial z} - \sigma^* H_y\right) \\
\frac{\partial H_z}{\partial t} &= \frac{1}{\mu}\left(\frac{\partial E_x}{\partial y} - \frac{\partial E_y}{\partial x} - \sigma^* H_z\right)
\end{aligned} \tag{24a}$$

$$\frac{\partial E_x}{\partial t} = \frac{1}{\varepsilon}\left(\frac{\partial H_z}{\partial y} - \frac{\partial H_y}{\partial z} - \sigma E_x\right)$$
$$\frac{\partial E_y}{\partial t} = \frac{1}{\varepsilon}\left(\frac{\partial H_x}{\partial z} - \frac{\partial H_z}{\partial x} - \sigma E_y\right) \qquad (24b)$$
$$\frac{\partial E_z}{\partial t} = \frac{1}{\varepsilon}\left(\frac{\partial H_y}{\partial x} - \frac{\partial H_x}{\partial y} - \sigma E_z\right)$$

In 1966, Kane Yee [8] originated a set of finite-difference equations for the time-dependent Maxwell's curl equations system given above. The curl equations can be represented in a discrete form, both in space and in time, employing a second order approximation resulting from the Taylor series expansion described by Yee:

$$\frac{\partial f}{\partial x}(x_o) = \frac{f(x_o + \frac{\Delta}{2}) - f(x_o - \frac{\Delta}{2})}{\Delta} + O(\Delta^2) \qquad (25)$$

As illustrated in Figure 9, the Yee algorithm centers its *E* and *H* components in three-dimensional space so that every *E* component is surrounded by four circulating *H* components and every *H* component is surrounded by four circulating *E* components. This provides a simple picture of three-dimensional space being filled by an inter-linked array of Faraday's Law and Ampere's Law contours. The computational domain is thus obtained by stacking these unit cells into a large problem space. The resulting finite-difference expressions for the time and space derivatives used in the curl operators are central in nature (central-difference) and second-order accurate. For the rectangular Yee mesh, a stepped or "staircase" approximation of the surface and internal geometry of the

structure of interest is made, with a space resolution set by the size of the lattice unit cell. The Yee algorithm also centers its E and H components in time in what is termed a leapfrog arrangement. All of the E computations in the three dimensional space are completed and stored in memory for a particular time point using H data previously stored in the computer memory. Then all of the H computations in the modeled space are completed and stored in memory using the E data just computed. The cycle can begin again with the re-computation of the E components based on the newly obtained H. This leapfrog time-stepping process is fully explicit, thereby completely avoiding the problems involved with simultaneous equations and matrix inversion.

Using Yee's notation, a space point in a uniform, rectangular lattice is denoted as:

$$(i, j, k) = (i\Delta x, j\Delta y, k\Delta z) \tag{26}$$

where Δx, Δy, Δz are the lattice space increments in the x, y, and z coordinate directions and i, j, k are integers [18].

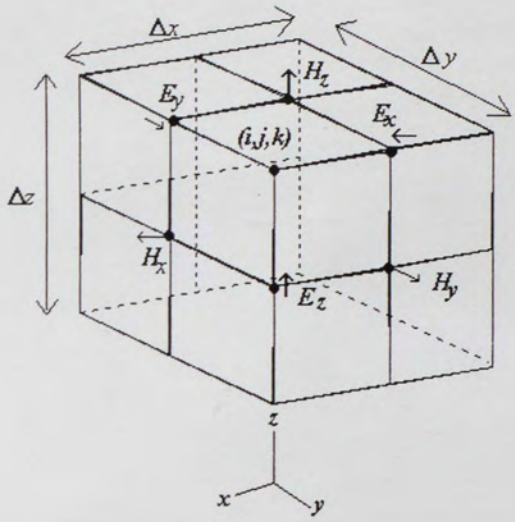

Figure 9. Yee's unit cell. Position of the electric and magnetic field vector components about a cubic unit cell of the Yee space lattice.

Further, let's denote any function u of space and time evaluated at a discrete point in the grid and at a discrete point in time as:

$$u(i\Delta x, j\Delta y, k\Delta z, n\Delta t) = u^{n}_{i,j,k} \tag{27}$$

Using the centered finite difference expressions for the space and time derivatives, yields the desired explicit time-stepping relations for E and H fields in the lossy material formulation as follows [16,17]:

$$E_x\Big|_{i,j,k}^{n+1} = C_a\Big|_{i,j,k} E_x\Big|_{i,j,k}^{n} + C_b\Big|_{i,j,k}\left[\left(\frac{H_z\Big|_{i,j+1/2,k}^{n+1/2} - H_z\Big|_{i,j-1/2,k}^{n+1/2}}{\Delta y}\right) - \left(\frac{H_y\Big|_{i,j,k+1/2}^{n+1/2} - H_y\Big|_{i,j,k-1/2}^{n+1/2}}{\Delta z}\right)\right]$$

$$E_y\Big|_{i,j,k}^{n+1} = C_a\Big|_{i,j,k} E_y\Big|_{i,j,k}^{n} + C_b\Big|_{i,j,k}\left[\left(\frac{H_x\Big|_{i,j,k+1/2}^{n+1/2} - H_x\Big|_{i,j,k-1/2}^{n+1/2}}{\Delta z}\right) - \left(\frac{H_z\Big|_{i+1/2,j,k}^{n+1/2} - H_z\Big|_{i-1/2,j,k}^{n+1/2}}{\Delta x}\right)\right] \quad (28a)$$

$$E_z\Big|_{i,j,k}^{n+1} = C_a\Big|_{i,j,k} E_z\Big|_{i,j,k}^{n} + C_b\Big|_{i,j,k}\left[\left(\frac{H_y\Big|_{i+1/2,j,k}^{n+1/2} - H_y\Big|_{i-1/2,j,k}^{n+1/2}}{\Delta x}\right) - \left(\frac{H_x\Big|_{i,j+1/2,k}^{n+1/2} - H_x\Big|_{i,j-1/2,k}^{n+1/2}}{\Delta y}\right)\right]$$

$$C_a\Big|_{i,j,k} = \frac{1 - \dfrac{\sigma_{i,j,k}\Delta t}{2\varepsilon_{i,j,k}}}{1 + \dfrac{\sigma_{i,j,k}\Delta t}{2\varepsilon_{i,j,k}}}, C_b\Big|_{i,j,k} = \frac{\dfrac{\Delta t}{\varepsilon_{i,j,k}}}{1 + \dfrac{\sigma_{i,j,k}\Delta t}{2\varepsilon_{i,j,k}}} \quad (28b)$$

$$H_x\Big|_{i,j,k}^{n+1/2} = D_a\Big|_{i,j,k} H_x\Big|_{i,j,k}^{n-1/2} + D_b\Big|_{i,j,k}\left[\left(\frac{E_y\Big|_{i,j,k+1/2}^{n} - E_y\Big|_{i,j,k-1/2}^{n}}{\Delta z}\right) - \left(\frac{E_z\Big|_{i,j+1/2,k}^{n} - E_z\Big|_{i,j-1/2,k}^{n}}{\Delta y}\right)\right]$$

$$H_y\Big|_{i,j,k}^{n+1/2} = D_a\Big|_{i,j,k} H_y\Big|_{i,j,k}^{n-1/2} + D_b\Big|_{i,j,k}\left[\left(\frac{E_z\Big|_{i+1/2,j,k}^{n} - E_z\Big|_{i-1/2,j,k}^{n}}{\Delta x}\right) - \left(\frac{E_x\Big|_{i,j,k+1/2}^{n} - E_x\Big|_{i,j,k-1/2}^{n}}{\Delta z}\right)\right] \quad (29a)$$

$$H_z\Big|_{i,j,k}^{n+1/2} = D_a\Big|_{i,j,k} H_z\Big|_{i,j,k}^{n-1/2} + D_b\Big|_{i,j,k}\left[\left(\frac{E_x\Big|_{i,j+1/2,k}^{n} - E_x\Big|_{i,j-1/2,k}^{n}}{\Delta y}\right) - \left(\frac{E_y\Big|_{i+1/2,j,k}^{n} - E_y\Big|_{i-1/2,j,k}^{n}}{\Delta x}\right)\right]$$

$$D_a\Big|_{i,j,k} = \frac{1 - \dfrac{\sigma^{*}_{i,j,k}\Delta t}{2\mu_{i,j,k}}}{1 + \dfrac{\sigma^{*}_{i,j,k}\Delta t}{2\mu_{i,j,k}}}, D_b\Big|_{i,j,k} = \frac{\dfrac{\Delta t}{\mu_{i,j,k}}}{1 + \dfrac{\sigma^{*}_{i,j,k}\Delta t}{2\mu_{i,j,k}}} \quad (29b)$$

The numerical algorithm requires that the time increment Δt have a specific bound relative to the lattice space increments Δx, Δy and Δz. The upper bound on Δt to guarantee numerical stability (known as Courant's stability criterion) is [16,17]:

$$\Delta t \leq \frac{1}{c\sqrt{\left(\frac{1}{\Delta x}\right)^2 + \left(\frac{1}{\Delta y}\right)^2 + \left(\frac{1}{\Delta z}\right)^2}} \tag{30}$$

where c is the maximum velocity of the wave propagating in the media, i.e., light speed in free space.

3.2 Mur's Absorbing Boundary Conditions

For many applications that require to model scattering from an object or a radiating antenna situated in free space, it is desired that the scattered or radiated fields propagate into boundless space. Unfortunately, the FDTD computational space is bounded, and when the scattered or radiated fields arrive at the boundary they will be reflected back into the computation space. That is why it is necessary to have what is called as an Absorbing Boundary Condition (ABC) that absorbs these fields when they arrive at the limits of the FDTD space so that scattering or radiation into boundless free space is at least approximately simulated. A simple, yet very useful, ABC was proposed by Mur; a first order condition looks back one step in time and into the space one cell location; a second order condition looks back two steps in time and inward two cell locations [16,17].

Mur's first order ABC assumes that the waves are normal-incident to the mesh walls. This assumption leads to a simple approximate continuous absorbing boundary condition: the tangential fields at the outer boundaries will obey the one-dimensional wave equation in the direction normal to the mesh wall.

For the wave normal to the x-direction:

$$\left(\frac{\partial}{\partial x} - \frac{1}{c}\frac{\partial}{\partial t}\right)E_{tan} = 0 \tag{31a}$$

For the wave normal to the y-direction:

$$\left(\frac{\partial}{\partial y} - \frac{1}{c}\frac{\partial}{\partial t}\right)E_{tan} = 0 \tag{31b}$$

For the wave normal to the z-direction:

$$\left(\frac{\partial}{\partial z} - \frac{1}{c}\frac{\partial}{\partial t}\right)E_{tan} = 0 \tag{31c}$$

Considering the E_x and E_y components located at $x = i\Delta x$, $y = j\Delta y$ and $z = nz \cdot \Delta z$, the first order Mur estimate at the boundary walls is:

$$\begin{aligned} E_x\Big|_{i,j,nz}^{n+1} &= E_x\Big|_{i,j,nz-1}^{n} + \frac{c\Delta t - \Delta z}{c\Delta t + \Delta z}\left(E_x\Big|_{i,j,nz-1}^{n+1} - E_x\Big|_{i,j,nz}^{n}\right) \\ E_y\Big|_{i,j,nz}^{n+1} &= E_y\Big|_{i,j,nz-1}^{n} + \frac{c\Delta t - \Delta z}{c\Delta t + \Delta z}\left(E_y\Big|_{i,j,nz-1}^{n+1} - E_y\Big|_{i,j,nz}^{n}\right) \end{aligned} \tag{31d}$$

Considering the E_x and E_y components located at $x = i\Delta x$, $y = j\Delta y$ and $z = 0$, the first order Mur estimate at the boundary walls is:

$$E_x\Big|_{i,j,0}^{n+1} = E_x\Big|_{i,j,1}^{n} + \frac{c\Delta t - \Delta z}{c\Delta t + \Delta z}\left(E_x\Big|_{i,j,1}^{n+1} - E_x\Big|_{i,j,0}^{n}\right)$$
$$E_y\Big|_{i,j,0}^{n+1} = E_y\Big|_{i,j,1}^{n} + \frac{c\Delta t - \Delta z}{c\Delta t + \Delta z}\left(E_y\Big|_{i,j,1}^{n+1} - E_y\Big|_{i,j,0}^{n}\right) \qquad (31e)$$

Considering the E_y and E_z components located at $x = nx \cdot \Delta x$, $y = j\Delta y$ and $z = k\Delta z$, the first order Mur estimate at the boundary walls is:

$$E_y\Big|_{nx,j,k}^{n+1} = E_y\Big|_{nx-1,j,k}^{n} + \frac{c\Delta t - \Delta x}{c\Delta t + \Delta x}\left(E_y\Big|_{nx-1,j,k}^{n+1} - E_y\Big|_{nx,j,k}^{n}\right)$$
$$E_z\Big|_{nx,j,k}^{n+1} = E_z\Big|_{nx-1,j,k}^{n} + \frac{c\Delta t - \Delta x}{c\Delta t + \Delta x}\left(E_z\Big|_{nx-1,j,k}^{n+1} - E_z\Big|_{nx,j,k}^{n}\right) \qquad (31f)$$

Considering the E_y and E_z components located at $x = 0$, $y = j\Delta y$ and $z = k\Delta z$, the first order Mur estimate at the boundary walls is:

$$E_y\Big|_{0,j,k}^{n+1} = E_y\Big|_{1,j,k}^{n} + \frac{c\Delta t - \Delta x}{c\Delta t + \Delta x}\left(E_y\Big|_{1,j,k}^{n+1} - E_y\Big|_{0,j,k}^{n}\right)$$
$$E_z\Big|_{0,j,k}^{n+1} = E_z\Big|_{1,j,k}^{n} + \frac{c\Delta t - \Delta x}{c\Delta t + \Delta x}\left(E_z\Big|_{1,j,k}^{n+1} - E_z\Big|_{0,j,k}^{n}\right) \qquad (31g)$$

Considering the E_x and E_z components located at $x = i\Delta x$, $y = ny \cdot \Delta y$ and $z = k\Delta z$, the first order Mur estimate at the boundary walls is:

$$E_x\Big|_{i,ny,k}^{n+1} = E_x\Big|_{i,ny-1,k}^{n} + \frac{c\Delta t - \Delta y}{c\Delta t + \Delta y}\left(E_x\Big|_{i,ny-1,k}^{n+1} - E_x\Big|_{i,ny,k}^{n}\right)$$
$$E_z\Big|_{i,ny,k}^{n+1} = E_z\Big|_{i,ny-1,k}^{n} + \frac{c\Delta t - \Delta y}{c\Delta t + \Delta y}\left(E_z\Big|_{i,ny-1,k}^{n+1} - E_z\Big|_{i,ny,k}^{n}\right) \qquad (31h)$$

Considering the E_x and E_z components located at $x = i\Delta x$, $y = 0$ and $z = k\Delta z$, the first order Mur estimate at the boundary walls is:

$$E_x\Big|_{i,0,k}^{n+1} = E_x\Big|_{i,1,k}^{n} + \frac{c\Delta t - \Delta y}{c\Delta t + \Delta y}\left(E_x\Big|_{i,1,k}^{n+1} - E_x\Big|_{i,0,k}^{n}\right)$$
$$E_z\Big|_{i,0,k}^{n+1} = E_z\Big|_{i,1,k}^{n} + \frac{c\Delta t - \Delta y}{c\Delta t + \Delta y}\left(E_z\Big|_{i,1,k}^{n+1} - E_z\Big|_{i,0,k}^{n}\right) \qquad (31i)$$

In other words, the tangential electric field on the artificial boundary wall can be obtained from the previous value of that field, and the field components one node inside of the mesh wall in the current and next time step.

In order to implement the first order Mur ABC, the normal components of the electric field at the boundary walls are obtained using the regular Yee's algorithm. The tangential components of the electric field at the intersection of two of the terminating planes (boundary walls) are obtained by taking the average of the values of that component around the specific point.

The continuous second order absorbing boundary condition for the wave normal to the x-direction is:

$$\left[\frac{1}{c}\frac{\partial^2}{\partial z \partial t}+\frac{1}{c^2}\frac{\partial^2}{\partial t^2}-\frac{1}{2}\left(\frac{\partial^2}{\partial x^2}-\frac{\partial^2}{\partial y^2}\right)\right]E_{tan}=0 \tag{32}$$

The second order estimate for E_z at the boundary $x = 0$ is:

$$E_z\big|_{0,j,k}^{n+1} = -E_z\big|_{1,j,k}^{n-1} + EQ_1 + EQ_2 + EQ_3 + EQ_4 \tag{32a}$$

$$\begin{aligned}
EQ_1 &= \frac{c\Delta t - \Delta x}{c\Delta t + \Delta x}\left(E_z\big|_{1,j,k}^{n+1} + E_z\big|_{0,j,k}^{n-1}\right)\\
EQ_2 &= \frac{2\Delta x}{c\Delta t + \Delta x}\left(E_z\big|_{0,j,k}^{n} + E_z\big|_{1,j,k}^{n}\right)\\
EQ_3 &= \frac{\Delta x(c\Delta t)^2}{2(\Delta y)^2(c\Delta t + \Delta x)}(C_a + C_b)\\
EQ_4 &= \frac{\Delta x(c\Delta t)^2}{2(\Delta z)^2(c\Delta t + \Delta x)}(C_c + C_d)
\end{aligned} \tag{32b}$$

$$\begin{aligned}
C_a &= E_z\big|_{0,j+1,k}^{n} - 2E_z\big|_{0,j,k}^{n} + E_z\big|_{0,j-1,k}^{n}\\
C_b &= E_z\big|_{1,j+1,k}^{n} - 2E_z\big|_{1,j,k}^{n} + E_z\big|_{1,j-1,k}^{n}\\
C_c &= E_z\big|_{0,j,k+1}^{n} - 2E_z\big|_{0,j,k}^{n} + E_z\big|_{0,j,k-1}^{n}\\
C_d &= E_z\big|_{1,j,k+1}^{n} - 2E_z\big|_{1,j,k}^{n} + E_z\big|_{1,j,k-1}^{n}
\end{aligned} \tag{32c}$$

The second order estimate for E_z at the boundary $x = n\cdot\Delta x$ is:

$$E_z\Big|_{nx,j,k}^{n+1} = -E_z\Big|_{nx-1,j,k}^{n-1} + EQ_1 + EQ_2 + EQ_3 + EQ_4 \tag{32d}$$

$$\begin{aligned} EQ_1 &= \frac{c\Delta t - \Delta x}{c\Delta t + \Delta x}\left(E_z\Big|_{nx-1,j,k}^{n+1} + E_z\Big|_{nx,j,k}^{n-1}\right) \\ EQ_2 &= \frac{2\Delta x}{c\Delta t + \Delta x}\left(E_z\Big|_{nx,j,k}^{n} + E_z\Big|_{nx-1,j,k}^{n}\right) \\ EQ_3 &= \frac{\Delta x(c\Delta t)^2}{2(\Delta y)^2(c\Delta t + \Delta x)}\left(C_a + C_b\right) \\ EQ_4 &= \frac{\Delta x(c\Delta t)^2}{2(\Delta z)^2(c\Delta t + \Delta x)}\left(C_c + C_d\right) \end{aligned} \tag{32e}$$

$$\begin{aligned} C_a &= E_z\Big|_{nx,j+1,k}^{n} - 2E_z\Big|_{nx,j,k}^{n} + E_z\Big|_{nx,j-1,k}^{n} \\ C_b &= E_z\Big|_{nx-1,j+1,k}^{n} - 2E_z\Big|_{nx-1,j,k}^{n} + E_z\Big|_{nx-1,j-1,k}^{n} \\ C_c &= E_z\Big|_{nx,j,k+1}^{n} - 2E_z\Big|_{nx,j,k}^{n} + E_z\Big|_{nx,j,k-1}^{n} \\ C_d &= E_z\Big|_{nx-1,j,k+1}^{n} - 2E_z\Big|_{nx-1,j,k}^{n} + E_z\Big|_{nx-1,j,k-1}^{n} \end{aligned} \tag{32f}$$

The equations needed to determine other field components with second order Mur estimate at other limiting surfaces of the FDTD space, are determined by modification of the above expressions.

One important consideration for implementing the second order Mur ABC, is that because the second order estimate requires field values from adjacent Yee cells, it cannot be used for determining electric field values that are adjacent to the intersection of two of the terminating planes (boundary walls). Therefore, even if second order Mur is being applied, first order Mur must be used for field components located adjacent to the edges of the problem space.

For Mur's absorbing boundary conditions, the farther from the object the outer boundary is located the better the absorption of the outward traveling waves. This is due

to these waves becoming more like plane waves as they travel farther from the structure that radiates them. However, the number of cells that can be placed between the object and the outer boundary is limited by computer memory. Moving the outer boundary too close to the object may cause instabilities the absorbing boundary implementation. Also, some fields that are required for an accurate solution may be absorbed if the outer boundary is too close.

3.3 Source Treatment

In addition to the basic aspects of ABCs, discrete representation and stability of Maxwell's vector-field equations when numerically approximated in a uniform Cartesian FDTD space lattice, it is important to consider the introduction of electromagnetic wave excitations into the FDTD mesh. A "hard source" is specified assigning a desired time function to specific electric or magnetic field components in the FDTD space lattice. Because the total electric field is specified at a certain region i_s without regard to any possible reflected waves in the grid (hence the terminology hard source), the hard source causes a spurious, nonphysical retro-reflection of these waves at i_s back toward the material structure of interest. It prevents the movement of reflected wave energy through the source position, and thereby fails to properly simulate a physical incident wave. A simple way to mitigate the reflective nature of a pulsed hard source is to remove it from the algorithm after the pulse has decayed essentially to zero and apply instead the normal Yee field update [16, 17, 19].

The following hard source on E_z could be established at the grid source location to generate a continuous sinusoidal wave of frequency f_o which is switched on at n = 0:

$$E_z\big|_{i,j,k}^{n} = E_o \sin(2\pi f_o n\Delta t) \tag{33}$$

A second common hard source provides a wide-band Gaussian pulse that provides a smooth roll off in frequency-content and a finite dc-content. The pulse is centered at time step n_o and has a *1/e* characteristic decay of n_{decay} time steps:

$$E_z\big|_{i,j,k}^{n} = E_o e^{-\left(\frac{n-n_o}{n_{decay}}\right)^2} \tag{33a}$$

A third common hard source provides zero dc-component, band-pass Gaussian pulse that has a Fourier spectrum symmetrical about f_o. The pulse is again centered at time step n_o and has a *1/e* characteristic decay of n_{decay} time steps:

$$E_z\big|_{i,j,k}^{n} = E_o e^{-\left(\frac{n-n_o}{n_{decay}}\right)^2} \sin[2\pi f_o(n-n_o)\Delta t] \tag{33b}$$

Although an ideal Gaussian pulse extends infinitely in time, this one must be truncated in the calculations and the effects of this must be considered, as well as the time duration of the pulse so that is has a suitable bandwidth.

The Fourier Transform of the Gaussian pulse is:

$$\Im\left\{ e^{-\left(\frac{n-n_o}{n_{decay}}\right)^2} \right\} = \sqrt{\pi} \cdot n_{decay} \Delta t \cdot e^{-(\pi \cdot f \cdot n_{decay} \Delta t)^2} e^{-j\omega \cdot t_o} \tag{34}$$

Normalizing the magnitude of the above expression, it is possible to choose its minimum value at the maximum frequency of interest. For example, if the minimum magnitude allowed is *–20 dB*, the value of n_{decay} can be obtained from:

$$20 \log\left[e^{-(\pi \cdot f_{max} \cdot n_{decay} \Delta t)^2} \right] = -20dB \tag{35}$$

Finally, under the assumption stated above, the following expressions will yield a desired pulse within a reasonable dynamic range:

$$\begin{aligned} n_{decay} &= \frac{1}{2 f_{max}} \\ n_o &= 4 n_{decay} \end{aligned} \tag{36}$$

where f_{max} is the maximum frequency of interest [6,7].

The value for n_o is obtained as follows. Although an ideal Gaussian pulse extends infinitely in time, ours must be truncated in the calculations, and the effects of this must be considered. We must specify the time duration of the pulse so that it has a suitable

bandwidth. The Gaussian pulse will "exist" from *0* to $2n_o$ time steps, approximated as zero outside this range, and with peak value at n_o. At the truncation points, the Gaussian pulse will have a value of $e^{-\left(\frac{\pm n_o}{n_{decay}}\right)^2}$. So, by choosing $n_o = 4n_{decay}$ the Gaussian pulse is down by e^{-16} or almost –140 dB.

4. MICROSTRIP ANTENNA ANALYSIS USING FDTD

4.1 Coaxial Line and Microstrip Antenna Analysis

In order to make an accurate characterization and modeling of stacked microstrip antennas fed with a coaxial line, a full wave analysis is very important to deliver accurate results in a wide-band frequency region. Using full wave analysis, all the parasitic effects are included in the model, as well as fringing fields, dielectric discontinuities and characteristic impedance of the coaxial line. FDTD meets these characteristics, since it is capable of solving Maxwell's equations directly [20,21].

The FDTD space grid size must be chosen such that over one increment the electromagnetic field does not change significantly. The minimum dimension of the grid must be only a fraction of the minimum wavelength expected in the model; through extensive experimental study it has been determined to be $\lambda/20$ or less for rectangular patches, $\lambda/40$ or less for circular patches. For computational stability, the time stepping is chosen to satisfy the Courant's stability criterion.

At $t = 0$, all the field components are made equal to zero over the entire computational region. Since the frequency spectrum of a Gaussian pulse is also Gaussian and gives a frequency domain information from dc to the desired value of interest by adjusting its width, a Gaussian pulse is used as the excitation of the fields.

The common focuses on the FDTD numerical implementation of the microstrip antenna geometry are the modeling of substrates and the modeling of the discontinuities. Microstrip patch antennas have relatively small substrate thickness as compared to the patch resonant length width. Since the substrate thickness has a major effect on the antenna characteristics, it is necessary for this substrate thickness to be modeled by at least three cells to take into account the effect of substrate material [20-26].

4.1.1 Conductor Treatment

The conductor treatment is not difficult. However, one must be very careful to make sure that the electric and magnetic fields are interleaved in space and set to the correct value at the specified node. Refer to Yee's cell to clarify this concept.

Assuming perfect electric conductors, the tangential component of the electric field and the normal component of the magnetic field are equal to zero on the ground plane, on conducting patches and on microstrip line conductors. This is the procedure used throughout this dissertation [22-24].

To take into account the singularity near the metallic edge, the known asymptotic field behavior can be employed to modify the finite-difference approximations of the *H*-fields near the metallic edge. Using this procedure, it can be concluded and shown that the standard finite-difference equations can still represent the accurate field behavior near the metallic edge, providing the metallic structure is properly placed so that its edge exceeds the node space by the amount of $0.191 \cdot \Delta x$.

4.1.2 Dielectric Interface Treatment

In the FDTD modeling of the object, material parameters are directly assigned to each unit cell, or more specifically, assigned to each related field component. However, at the interface between two different materials, the material parameters are not well defined. Thus, it is necessary to find the proper material parameters at the interface.

Consider a dielectric interface separating two media of permitivity ε_1 and ε_2. The tangential E field component can be carried out via Maxwell's equations in the two media as [22-24]:

$$\begin{aligned} \varepsilon_1 \frac{\partial E_x^1}{\partial t} &= \frac{\partial H_y^1}{\partial z} - \frac{\partial H_z^1}{\partial y} \\ \varepsilon_2 \frac{\partial E_x^2}{\partial t} &= \frac{\partial H_y^2}{\partial z} - \frac{\partial H_z^2}{\partial y} \end{aligned} \tag{37}$$

Based on the boundary conditions, the tangential E-field and the normal derivative of the H-field components must maintain continuity. Thus, adding the above equations and applying the continuity property yields:

$$\frac{\varepsilon_1 + \varepsilon_2}{2} \frac{\partial E_x}{\partial t} = \frac{\partial H_y}{\partial z} - \frac{1}{2}\left(\frac{\partial H_z^1}{\partial y} + \frac{\partial H_z^2}{\partial y} \right) \tag{38}$$

Numerical experience shows that the average of the normal derivatives of H_z with respect to y in the above equation is not necessary because there is only very little

difference between these two H_z derivatives. Therefore, the fields behave just as if the permitivity were

$$\varepsilon = \frac{\varepsilon_1 + \varepsilon_2}{2} \tag{39}$$

The dielectric constant on the interface of two different materials is thus modeled as an average of these two dielectric constants. This result can also be understood intuitively from the idea that the discrete fields located at the interface region are actually representing the continued fields within this region. Therefore, in the microstrip antenna case, the interface plane between two dielectric materials is modeled as one zero-thickness dielectric surface that has the dielectric constant of the average of the two dielectric constants.

4.1.3 Coaxial Feed Models

There are at least three different coaxial feed models that can be used in combination with the FDTD method. The first model, proposed by Reineix and Jecko, is a simple gap feed model in terms of total-field voltage and current; it was later modified by Luebbers and Langdon [22,27]. The second one, proposed by Jensen and Rahmat-Samii, involves simulating a coaxial feeding cable [28]. The third one, proposed by Wu and Litva, involves the explicit insertion of the coaxial feed in the FDTD lattice [29, 30].

4.1.3.1 The Gap Feed Model

The gap feed model, which turns out to be the simplest one, consists of a feeding structure realized as a voltage generator with an internal resistor placed at a small gap between the patch and ground plane. This model works well assuming that the coaxial probe is very thin. An added internal resistor can provide an additional loss mechanism to decrease the current amplitude rapidly and then reduce the required simulation steps. A larger resistance can provide more loss and further reduce the time steps required for convergence. However, it has been shown through numerical experiments that the resistance cannot be too large, otherwise the accuracy level is not satisfied, and instabilities might occur due to neglecting the displacement current through the FDTD cell containing the source. The value of the internal source resistance is generally chosen as the system characteristic impedance to physically mimic the system. Since all the microwave equipment are set to 50 ohms, the source resistance is thus chosen to be 50 ohms [22,27].

The FDTD implementation of this voltage source with an internal resistor can be illustrated by its equivalent circuit representation: a voltage source V_s^n in series with the internal resistor $R_s = 50\Omega$. The voltage source can be any of the source types used with FDTD (Gaussian, etc). The voltage at the feed point V_z^n is represented in the FDTD simulation by an imposed E-field at the feed point (if, jf, kf) as

$$E_z\big|^n_{if,jf,kf} = -\frac{V_s^n - R_s I_s^n}{\Delta z} \tag{40}$$

The current I_s^n through the source can be determined by applying Ampere's law, taking the line integral of the H field around the source location at every time step,

$$I_s^{n+1/2} = \frac{H_x\big|_{i,j,k}^{n+1/2} - H_x\big|_{i,j+1,k}^{n+1/2}}{\Delta x} + \frac{H_y\big|_{i+1,j,k}^{n+1/2} - H_y\big|_{i,j,k}^{n+1/2}}{\Delta y} \tag{41}$$

The time offset of $\Delta t/2$ between the source voltage and current can be generally neglected since it is assumed to be small.

It is worth noting that the connecting wire with infinitesimal diameter in the model of the feeding structure is actually modeled in the FDTD problem space by setting to zero the tangential component of the electric field, i.e., E_z.

This simple model can also be used to simulate a microstrip feeding structure. However, since the wire is a non-physical structure for the microstrip feed, a series inductance needs to be removed from the final results during the post-processing. The inductance introduced by the connecting wire can be found by a calibration run, which is done by comparing a known result with the FDTD simulation result. It has been determined empirically that the wire has an approximate inductance of 0.01 μH/cm.

4.1.3.2 Wire Model

This model involves simulating a coaxial wire feed. The inner conductor radius r_a, outer conductor radius r_b and permitivity ε within the coaxial line are chosen to

represent the desired characteristic impedance. A gap voltage is introduced in the coaxial center conductor, and the standard FDTD relations are used within the coax to propagate the fields toward the antenna [28].

At the end of the coax, special interfacing relations are required to update the radial electric and circumferential magnetic fields. The circumferential magnetic field is located half cell over the ground plane in the FDTD lattice. Its relation is derived using the integral forms of Maxwell's equations and assuming a $1/\rho$ dependence of the fields. Using this approach, the modified time-stepping equation assumes the form:

$$H_x\Big|_{i,j,k}^{n+1/2} = H_x\Big|_{i,j,k}^{n-1/2} + \frac{\Delta t}{\mu_{i,j,k}}\left[\frac{E_y\Big|_{i,j,k}^{n} - \Psi E_y\Big|_{i,j,k-1}^{n}}{\Delta z} - \frac{E_z\Big|_{i,j,k}^{n} - E_z\Big|_{i,j-1,k}^{n}}{(\Delta y/2)\ln(\Delta y/r_a)}\right] \tag{42}$$

$$\Psi = \frac{r_b \ln(r_b/r_a)}{\Delta y \ln(\Delta y/r_a)}$$

The tangential electric field $E_y\Big|_{i,j,k-1}^{n+1}$ at the coax-antenna interface can be calculated using the standard FDTD relations with the modification that $H_x\Big|_{i,j,k}^{n+1/2}$ is substituted by $(\Delta y/r_b)H_x\Big|_{i,j,k}^{n+1/2}$ to align $H_x\Big|_{i,j,k}^{n+1/2}$ (antenna region) with $H_x\Big|_{i,j,k-1}^{n+1/2}$ (coax region).

Similar relations can be derived for the other circumferential magnetic and radial electric fields at the interface.

The feed point voltage is obtained from the computed radial electric field using

$$V_s^n = \frac{r_b}{2} ln\left(\frac{r_b}{r_a}\right) E_y\Big|_{i,j,k-1}^n \tag{43}$$

The current in the wire can be obtained from the discretized form of Ampere's Law. Because reverse propagating modes in the coax are excited by the source voltage and by reflections from the coax-antenna transition, it is essential to terminate the coax with an absorbing boundary condition. A first-order accuracy boundary condition works well assuming that the propagating mode in the coax is transverse electromagnetic.

In the antenna region, the circumferential magnetic fields in the cells immediately adjacent to the wire, over the coax-antenna transition and towards the microstrip patch, can be calculated using an expression similar to equation (42) but with $\Psi = 1$. The term $E_z\Big|_{i,j,k-1}^{n+1}$ will be set to zero for a perfectly conducting wire (it could also be forced to some functional form if it is to be a source point). The computation of the other field components and for the fields not adjacent to the wire can be accurately performed with the standard FDTD equations.

4.1.3.3 Explicit Coaxial Feed Model

This is a rigorous, explicit feed model. We need a simple feed model that does not introduce a very large computational overhead, that can be used to simulate thick coaxial probes and that can be used in a microstrip array environment. In this explicit coaxial feed model, the computational space is divided into two regions. One is the coaxial line region and the other is the antenna region. If the coaxial structure is defined with a small

number of FDTD cells, thus the processing time spent in the coaxial line region is very small compared to that spent in the antenna region [29,30].

The space increments $\Delta x, \Delta, \Delta z$ of the FDTD lattice in the coax region are chosen to be equal to those of the antenna region. Since the characteristic impedance of a SMA connector and its coaxial line is about *50* ohms, a calibration run is needed to make sure that the numerical characteristic impedance of the coaxial line is equal to *50* ohms over the frequency range of interest. Figure 10 illustrates the coaxial line feed and how it is merged into the antenna.

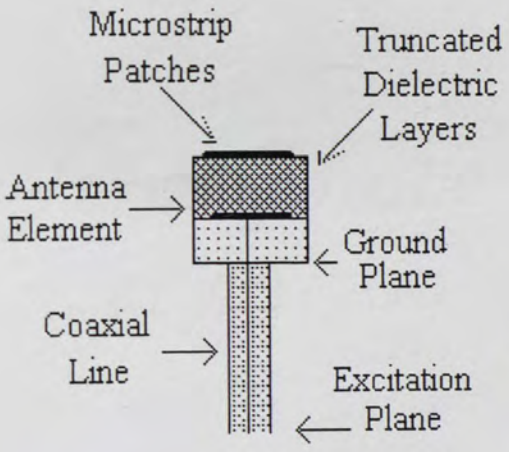

Figure 10. Rigorous Coaxial Feed Model. The computational domain for the feed used for the simulations is *7x7x70* and $\varepsilon_r = 2.5$.

Given that a coaxial line can excite TEM modes up to a predictable cutoff frequency, it can be assumed that the electric field will be traveling perpendicular to the coax-antenna transition and to the excitation plane. Thus, the model will be valid below

this cutoff frequency and Mur's First Order ABC can be used in the coaxial region, as long as the coax-line length is kept long enough to account for the decay of any higher-order modes that could be present in the numerical model. The non-TEM modes that are excited by the nonphysical excitation will decay after propagating at most a few lattices. The only mode that is able to propagate down the coaxial line is the TEM mode.

A radial field distribution is specified at the excitation plane, projected to the Cartesian components of the FDTD lattice,

$$
\begin{aligned}
V_s^n &= -E_{feed}\Big|_{i,j,k}^n \Delta x \\
E_{x-feed}\Big|_{i,j,k}^n &= E_\rho\Big|_{i,j,k}^n \cos\phi \\
E_{y-feed}\Big|_{i,j,k}^n &= E_\rho\Big|_{i,j,k}^n \sin\phi \\
\phi &= tan^{-1}\left(\frac{\Delta\rho_y}{\Delta\rho_x}\right)
\end{aligned}
\tag{44}
$$

The increments $\Delta\rho_x, \Delta\rho_y$ represent the distance from the point being evaluated to the center of the coaxial line. The electric field $E_\rho\Big|_{i,j,k}^n$ takes on the values of the Gaussian-excitation. Mur's first order ABC is applied at the excitation plane once the Gaussian Pulse has completely departed from that plane. It is also used at the end of the coaxial line for the calibration run. The curved-boundary of the inner and outer conductor of a coaxial line can be approximated with a staircase, although a square coaxial line works well as long as it preserves the desired electrical characteristics (TEM excitation and characteristic impedance).

The radial electric and circumferential magnetic fields are merged at the coax-antenna transition. The radial electric field components are located at the coax-antenna interface, and therefore it is enough to set the continuity condition of the tangential electric fields at this interface,

$$E_x\Big|^n_{ic,jc,kc} = E_x\Big|^n_{i,j,0}$$
$$E_y\Big|^n_{ic,jc,kc} = E_y\Big|^n_{i,j,0} \tag{45}$$

The index (i_c, j_c, k_c) is used in the coax-region while the index (i, j, k) is used in the antenna-region. The standard FDTD equations can be used for the circumferential magnetic fields and for the rest of the fields in the computational space.

4.2 The Perfectly Matched Layer

Since the computation domain cannot include the whole space, the computational domain must be truncated. For the microstrip geometry, rather than extending the FDTD lattice out beyond the dielectric material edge, the lattice can be terminated as close as possible to the antenna using an absorbing medium.

The numerical algorithm must simulate the propagation of the outgoing waves using absorbing boundary conditions. In the case of the coax-fed stacked antennas, Mur's second order absorbing boundary conditions have been shown to be accurate enough. In order to avoid instabilities of Mur's boundary condition, the computational domain must be made large enough, and the computation must be carried out over a certain limited

period over which useful information can been obtained [31]. However, for an array of stacked microstrip antennas, it is necessary to have a boundary condition that can absorb all the waves coming in every direction towards the boundary walls.

In 1994 Berenger introduced the Perfectly Matched Layer (PML), a technique based on the use of an absorbing layer especially designed to absorb the electromagnetic waves without reflection [32-39].

PML splits all six Cartesian field vector components and introduces the electric and magnetic conductivity (σ and σ^*) to cause the decay of propagating fields, yielding 12 equations as follows [37]:

$$\frac{\partial H_{xy}}{\partial t} = -\frac{1}{\mu}\left[\frac{\partial (E_{zx} + E_{zy})}{\partial y} - \sigma_y^* H_{xy}\right]$$
$$\frac{\partial H_{xz}}{\partial t} = \frac{1}{\mu}\left[\frac{\partial (E_{yx} + E_{yz})}{\partial z} - \sigma_z^* H_{xz}\right] \quad (46a)$$

$$\frac{\partial H_{yz}}{\partial t} = -\frac{1}{\mu}\left[\frac{\partial (E_{xy} + E_{xz})}{\partial z} - \sigma_z^* H_{yz}\right]$$
$$\frac{\partial H_{yx}}{\partial t} = \frac{1}{\mu}\left[\frac{\partial (E_{zx} + E_{zy})}{\partial x} - \sigma_x^* H_{yx}\right] \quad (46b)$$

$$\frac{\partial H_{zx}}{\partial t} = -\frac{1}{\mu}\left[\frac{\partial (E_{yx} + E_{yz})}{\partial x} - \sigma_x^* H_{zx}\right]$$
$$\frac{\partial H_{zy}}{\partial t} = \frac{1}{\mu}\left[\frac{\partial (E_{xy} + E_{xz})}{\partial y} - \sigma_y^* H_{zy}\right] \quad (46c)$$

$$\frac{\partial E_{xy}}{\partial t} = \frac{1}{\varepsilon}\left[\frac{\partial (H_{zx} + H_{zy})}{\partial y} - \sigma_y E_{xy}\right]$$
$$\frac{\partial E_{xz}}{\partial t} = -\frac{1}{\varepsilon}\left[\frac{\partial (H_{yx} + H_{yz})}{\partial z} - \sigma_z H_{xz}\right] \quad (46d)$$

$$\frac{\partial E_{yz}}{\partial t} = \frac{1}{\varepsilon}\left[\frac{\partial (H_{xy} + H_{xz})}{\partial z} - \sigma_z E_{yz}\right]$$
$$\frac{\partial E_{yx}}{\partial t} = -\frac{1}{\varepsilon}\left[\frac{\partial (H_{zx} + H_{zy})}{\partial x} - \sigma_x E_{yx}\right] \qquad (46e)$$

$$\frac{\partial E_{zx}}{\partial t} = \frac{1}{\varepsilon}\left[\frac{\partial (H_{yx} + H_{yz})}{\partial x} - \sigma_x E_{zx}\right]$$
$$\frac{\partial E_{zy}}{\partial t} = -\frac{1}{\varepsilon}\left[\frac{\partial (H_{xy} + H_{xz})}{\partial y} - \sigma_y E_{zy}\right] \qquad (46f)$$

Using the centered finite difference expressions for the space and time derivatives, yields the desired time-stepping relations for E and H fields as follows:

$$H_{xy}\Big|_{i,j,k}^{n+1/2} = D_{y1}\Big|_{i,j,k} H_{xy}\Big|_{i,j,k}^{n-1/2} - D_{y2}\Big|_{i,j,k}\left(\frac{E_z\Big|_{i,j+1/2,k}^{n} - E_z\Big|_{i,j-1/2,k}^{n}}{\Delta y}\right)$$
$$H_{xz}\Big|_{i,j,k}^{n+1/2} = D_{z1}\Big|_{i,j,k} H_{xz}\Big|_{i,j,k}^{n-1/2} - D_{z2}\Big|_{i,j,k}\left(\frac{E_y\Big|_{i,j,k+1/2}^{n} - E_y\Big|_{i,j,k-1/2}^{n}}{\Delta z}\right) \qquad (47a)$$

$$H_{yz}\Big|_{i,j,k}^{n+1/2} = D_{z1}\Big|_{i,j,k} H_{yz}\Big|_{i,j,k}^{n-1/2} - D_{z2}\Big|_{i,j,k}\left(\frac{E_x\Big|_{i,j,k+1/2}^{n} - E_x\Big|_{i,j,k-1/2}^{n}}{\Delta z}\right)$$
$$H_{yx}\Big|_{i,j,k}^{n+1/2} = D_{x1}\Big|_{i,j,k} H_{yx}\Big|_{i,j,k}^{n-1/2} - D_{x2}\Big|_{i,j,k}\left(\frac{E_z\Big|_{i+1/2,j,k}^{n} - E_z\Big|_{i-1/2,j,k}^{n}}{\Delta x}\right) \qquad (47b)$$

$$H_{zx}\Big|_{i,j,k}^{n+1/2} = D_{x1}\Big|_{i,j,k} H_{zx}\Big|_{i,j,k}^{n-1/2} - D_{x2}\Big|_{i,j,k}\left(\frac{E_y\Big|_{i+1/2,j,k}^{n} - E_y\Big|_{i-1/2,j,k}^{n}}{\Delta x}\right)$$
$$H_{zy}\Big|_{i,j,k}^{n+1/2} = D_{y1}\Big|_{i,j,k} H_{zy}\Big|_{i,j,k}^{n-1/2} - D_{y2}\Big|_{i,j,k}\left(\frac{E_x\Big|_{i,j+1/2,k}^{n} - E_x\Big|_{i,j-1/2,k}^{n}}{\Delta y}\right) \qquad (47c)$$

$$E_{xy}\Big|_{i,j,k}^{n+1} = C_{xy1}\Big|_{i,j,k} E_{xy}\Big|_{i,j,k}^{n} - C_{xy2}\Big|_{i,j,k}\left(\frac{H_z\Big|_{i,j+1/2,k}^{n+1/2} - E_z\Big|_{i,j-1/2,k}^{n+1/2}}{\Delta y}\right)$$

$$E_{xz}\Big|_{i,j,k}^{n+1} = C_{xz1}\Big|_{i,j,k} E_{xz}\Big|_{i,j,k}^{n} - C_{xz2}\Big|_{i,j,k}\left(\frac{H_y\Big|_{i,j,k+1/2}^{n+1/2} - H_y\Big|_{i,j,k-1/2}^{n+1/2}}{\Delta z}\right) \tag{47d}$$

$$E_{yz}\Big|_{i,j,k}^{n+1} = C_{yz1}\Big|_{i,j,k} E_{yz}\Big|_{i,j,k}^{n} - C_{yz2}\Big|_{i,j,k}\left(\frac{H_x\Big|_{i,j,k+1/2}^{n+1/2} - H_x\Big|_{i,j,k-1/2}^{n+1/2}}{\Delta z}\right)$$

$$E_{yx}\Big|_{i,j,k}^{n+1} = C_{yx1}\Big|_{i,j,k} E_{yx}\Big|_{i,j,k}^{n} - C_{yx2}\Big|_{i,j,k}\left(\frac{H_z\Big|_{i+1/2,j,k}^{n+1/2} - H_z\Big|_{i-1/2,j,k}^{n+1/2}}{\Delta x}\right) \tag{47e}$$

$$E_{zx}\Big|_{i,j,k}^{n+1} = C_{zx1}\Big|_{i,j,k} E_{zx}\Big|_{i,j,k}^{n} - C_{zx2}\Big|_{i,j,k}\left(\frac{H_y\Big|_{i+1/2,j,k}^{n+1/2} - H_y\Big|_{i-1/2,j,k}^{n+1/2}}{\Delta x}\right)$$

$$E_{zy}\Big|_{i,j,k}^{n+1} = C_{zy1}\Big|_{i,j,k} E_{zy}\Big|_{i,j,k}^{n} - C_{zy2}\Big|_{i,j,k}\left(\frac{H_x\Big|_{i,j+1/2,k}^{n+1/2} - H_x\Big|_{i,j-1/2,k}^{n+1/2}}{\Delta y}\right) \tag{47f}$$

$$\begin{aligned} E_x\Big|_{i,j,k}^{n} &= E_{xy}\Big|_{i,j,k}^{n} + E_{xz}\Big|_{i,j,k}^{n} \\ E_y\Big|_{i,j,k}^{n} &= E_{yx}\Big|_{i,j,k}^{n} + E_{yz}\Big|_{i,j,k}^{n} \\ E_z\Big|_{i,j,k}^{n} &= E_{zx}\Big|_{i,j,k}^{n} + E_{zy}\Big|_{i,j,k}^{n} \end{aligned} \tag{47g}$$

$$\begin{aligned} H_x\Big|_{i,j,k}^{n+1/2} &= H_{xy}\Big|_{i,j,k}^{n+1/2} + H_{xz}\Big|_{i,j,k}^{n+1/2} \\ H_y\Big|_{i,j,k}^{n+1/2} &= H_{yx}\Big|_{i,j,k}^{n+1/2} + H_{yz}\Big|_{i,j,k}^{n+1/2} \\ H_z\Big|_{i,j,k}^{n+1/2} &= H_{zx}\Big|_{i,j,k}^{n+1/2} + H_{zy}\Big|_{i,j,k}^{n+1/2} \end{aligned} \tag{47h}$$

$$C_{xy1}\Big|_{i,j,k} = \frac{\dfrac{\varepsilon_x\Big|_{i,j,k}}{\Delta t} - \dfrac{\sigma_y\Big|_{i,j,k}}{2}}{\dfrac{\varepsilon_x\Big|_{i,j,k}}{\Delta t} + \dfrac{\sigma_y\Big|_{i,j,k}}{2}} \qquad (48a)$$

$$C_{xy2}\Big|_{i,j,k} = \frac{1}{\dfrac{\varepsilon_x\Big|_{i,j,k}}{\Delta t} + \dfrac{\sigma_y\Big|_{i,j,k}}{2}}$$

$$C_{xz1}\Big|_{i,j,k} = \frac{\dfrac{\varepsilon_x\Big|_{i,j,k}}{\Delta t} - \dfrac{\sigma_z\Big|_{i,j,k}}{2}}{\dfrac{\varepsilon_x\Big|_{i,j,k}}{\Delta t} + \dfrac{\sigma_z\Big|_{i,j,k}}{2}} \qquad (48b)$$

$$C_{xz2}\Big|_{i,j,k} = \frac{1}{\dfrac{\varepsilon_x\Big|_{i,j,k}}{\Delta t} + \dfrac{\sigma_z\Big|_{i,j,k}}{2}}$$

$$C_{yz1}\Big|_{i,j,k} = \frac{\dfrac{\varepsilon_y\Big|_{i,j,k}}{\Delta t} - \dfrac{\sigma_z\Big|_{i,j,k}}{2}}{\dfrac{\varepsilon_y\Big|_{i,j,k}}{\Delta t} + \dfrac{\sigma_z\Big|_{i,j,k}}{2}} \qquad (48c)$$

$$C_{yz2}\Big|_{i,j,k} = \frac{1}{\dfrac{\varepsilon_y\Big|_{i,j,k}}{\Delta t} + \dfrac{\sigma_z\Big|_{i,j,k}}{2}}$$

$$C_{yx1}\Big|_{i,j,k} = \frac{\dfrac{\varepsilon_y\Big|_{i,j,k}}{\Delta t} - \dfrac{\sigma_x\Big|_{i,j,k}}{2}}{\dfrac{\varepsilon_y\Big|_{i,j,k}}{\Delta t} + \dfrac{\sigma_x\Big|_{i,j,k}}{2}} \qquad (48d)$$

$$C_{yx2}\Big|_{i,j,k} = \frac{1}{\dfrac{\varepsilon_y\Big|_{i,j,k}}{\Delta t} + \dfrac{\sigma_x\Big|_{i,j,k}}{2}}$$

$$C_{zx1}\Big|_{i,j,k} = \frac{\dfrac{\varepsilon_z\Big|_{i,j,k}}{\Delta t} - \dfrac{\sigma_x\Big|_{i,j,k}}{2}}{\dfrac{\varepsilon_z\Big|_{i,j,k}}{\Delta t} + \dfrac{\sigma_x\Big|_{i,j,k}}{2}}$$

$$C_{zx2}\Big|_{i,j,k} = \frac{1}{\dfrac{\varepsilon_z\Big|_{i,j,k}}{\Delta t} + \dfrac{\sigma_x\Big|_{i,j,k}}{2}} \qquad (48e)$$

$$C_{zy1}\Big|_{i,j,k} = \frac{\dfrac{\varepsilon_z\Big|_{i,j,k}}{\Delta t} - \dfrac{\sigma_y\Big|_{i,j,k}}{2}}{\dfrac{\varepsilon_z\Big|_{i,j,k}}{\Delta t} + \dfrac{\sigma_y\Big|_{i,j,k}}{2}}$$

$$C_{zy2}\Big|_{i,j,k} = \frac{1}{\dfrac{\varepsilon_z\Big|_{i,j,k}}{\Delta t} + \dfrac{\sigma_y\Big|_{i,j,k}}{2}} \qquad (48f)$$

$$D_{x1}\Big|_{i,j,k} = \frac{\dfrac{\mu_o}{\Delta t} - \dfrac{\sigma^*_x\Big|_{i,j,k}}{2}}{\dfrac{\mu_o}{\Delta t} + \dfrac{\sigma^*_x\Big|_{i,j,k}}{2}}$$

$$D_{x2}\Big|_{i,j,k} = \frac{1}{\dfrac{\mu_o}{\Delta t} + \dfrac{\sigma^*_x\Big|_{i,j,k}}{2}} \qquad (48g)$$

$$D_{y1}\Big|_{i,j,k} = \frac{\dfrac{\mu_o}{\Delta t} - \dfrac{\sigma^*_y\Big|_{i,j,k}}{2}}{\dfrac{\mu_o}{\Delta t} + \dfrac{\sigma^*_y\Big|_{i,j,k}}{2}}$$

$$D_{y2}\Big|_{i,j,k} = \frac{1}{\dfrac{\mu_o}{\Delta t} + \dfrac{\sigma^*_y\Big|_{i,j,k}}{2}} \qquad (48h)$$

$$D_{z1}\Big|_{i,j,k} = \frac{\frac{\mu_o}{\Delta t} - \frac{\sigma^*_z\Big|_{i,j,k}}{2}}{\frac{\mu_o}{\Delta t} + \frac{\sigma^*_z\Big|_{i,j,k}}{2}}$$

$$D_{z2}\Big|_{i,j,k} = \frac{1}{\frac{\mu_o}{\Delta t} + \frac{\sigma^*_z\Big|_{i,j,k}}{2}} \tag{48i}$$

The attenuation to outgoing waves afforded by a PML medium is so rapid that standard Yee-time-stepping cannot be used, especially for structures whose transient fields do not decay appreciably with time (for example, structures electrically large or antennas with high dielectric constants) [37]. The constants given above must be modified to include an explicit exponential-difference time advance as follows:

$$C_{xy1}\Big|_{i,j,k} = e^{-\frac{\sigma_y\Big|_{i,j,k}\Delta t}{\varepsilon_x\Big|_{i,j,k}}}$$

$$C_{xy2}\Big|_{i,j,k} = \frac{1-e^{-\frac{\sigma_y\Big|_{i,j,k}\Delta t}{\varepsilon_x\Big|_{i,j,k}}}}{\sigma_y\Big|_{i,j,k}} \tag{49a}$$

$$C_{xz1}\Big|_{i,j,k} = e^{-\frac{\sigma_z\Big|_{i,j,k}\Delta t}{\varepsilon_x\Big|_{i,j,k}}}$$

$$C_{xz2}\Big|_{i,j,k} = \frac{1-e^{-\frac{\sigma_z\Big|_{i,j,k}\Delta t}{\varepsilon_x\Big|_{i,j,k}}}}{\sigma_z\Big|_{i,j,k}} \tag{49b}$$

$$C_{yz1}\Big|_{i,j,k} = e^{-\frac{\sigma_z|_{i,j,k}\,\Delta t}{\varepsilon_y|_{i,j,k}}}$$

$$C_{yz2}\Big|_{i,j,k} = \frac{1-e^{-\frac{\sigma_z|_{i,j,k}\,\Delta t}{\varepsilon_y|_{i,j,k}}}}{\sigma_z|_{i,j,k}} \tag{49c}$$

$$C_{yx1}\Big|_{i,j,k} = e^{-\frac{\sigma_x|_{i,j,k}\,\Delta t}{\varepsilon_y|_{i,j,k}}}$$

$$C_{yx2}\Big|_{i,j,k} = \frac{1-e^{-\frac{\sigma_x|_{i,j,k}\,\Delta t}{\varepsilon_y|_{i,j,k}}}}{\sigma_x|_{i,j,k}} \tag{49d}$$

$$C_{zx1}\Big|_{i,j,k} = e^{-\frac{\sigma_x|_{i,j,k}\,\Delta t}{\varepsilon_z|_{i,j,k}}}$$

$$C_{zx2}\Big|_{i,j,k} = \frac{1-e^{-\frac{\sigma_x|_{i,j,k}\,\Delta t}{\varepsilon_z|_{i,j,k}}}}{\sigma_x|_{i,j,k}} \tag{49e}$$

$$C_{zy1}\Big|_{i,j,k} = e^{-\frac{\sigma_y|_{i,j,k}\,\Delta t}{\varepsilon_z|_{i,j,k}}}$$

$$C_{zy2}\Big|_{i,j,k} = \frac{1-e^{-\frac{\sigma_y|_{i,j,k}\,\Delta t}{\varepsilon_z|_{i,j,k}}}}{\sigma_y|_{i,j,k}} \tag{49f}$$

$$D_{x1}\Big|_{i,j,k} = e^{-\frac{\sigma^*_x|_{i,j,k}\,\Delta t}{\mu_o}}$$

$$D_{x2}\Big|_{i,j,k} = \frac{1-e^{-\frac{\sigma^*_x|_{i,j,k}\,\Delta t}{\mu_o}}}{\sigma^*_x|_{i,j,k}} \tag{49g}$$

$$D_{y1}\Big|_{i,j,k} = e^{-\frac{\sigma_y^*\big|_{i,j,k}\Delta t}{\mu_o}}$$

$$D_{y2}\Big|_{i,j,k} = \frac{1-e^{-\frac{\sigma_y^*\big|_{i,j,k}\Delta t}{\mu_o}}}{\sigma_y^*\Big|_{i,j,k}} \tag{49h}$$

$$D_{z1}\Big|_{i,j,k} = e^{-\frac{\sigma_z^*\big|_{i,j,k}\Delta t}{\mu_o}}$$

$$D_{z2}\Big|_{i,j,k} = \frac{1-e^{-\frac{\sigma_z^*\big|_{i,j,k}\Delta t}{\mu_o}}}{\sigma_z^*\Big|_{i,j,k}} \tag{49i}$$

At the interfaces between normal FDTD and PML regions, it is desired that waves can propagate through without any reflections. Once waves enter the PML region, they will get attenuated and absorbed. If η_1 and η_2 are the wave impedances in the FDTD and PML region respectively, they can be expressed by the following equations, assuming normal incidence [32],

$$\eta_1 = \frac{\eta_o}{\sqrt{\varepsilon_r}}$$

$$\eta_2 = \sqrt{\frac{\mu_o + \frac{\sigma^*}{j\omega}}{\varepsilon_o\varepsilon_r + \frac{\sigma}{j\omega}}} = \frac{\eta_o}{\sqrt{\varepsilon_r}}\sqrt{\frac{1+\frac{\sigma^*}{j\omega\mu_o}}{1+\frac{\sigma}{j\omega\varepsilon_o\varepsilon_r}}} \tag{50}$$

where η_o is the characteristic impedance of free space and ω is the frequency of the incident wave. The necessary condition for no reflection as waves propagate through the interface is the impedance matching between these two regions, $\eta_1 = \eta_2$, which yields

$$\frac{\sigma}{\varepsilon} = \frac{\sigma^*}{\mu} \tag{51}$$

If ψ represents any component of a plane wave propagating in a two-dimensional PML medium, TE case, Berenger shows that with the matching condition given above, ψ can be expressed as

$$\begin{aligned} \psi &= \psi_o e^{j\omega\left(t - \frac{x\cos\phi + y\sin\phi}{v}\right)} e^{-\frac{\sigma_x \cos\phi}{\varepsilon_o \varepsilon_r v} x} e^{-\frac{\sigma_y \sin\phi}{\varepsilon_o \varepsilon_r v} y} \\ Z &= \frac{\eta_o}{\sqrt{\varepsilon_r}} \end{aligned} \tag{52}$$

where ψ_o is the magnitude of that component, ϕ is the angle with the y axis, and v is the wave velocity in the medium. This equation shows that the wave in the PML region travels at exactly the same speed as that in the normal FDTD region, but decays exponentially along the x and y directions. These results can be extended to the three dimensional case [32].

When a wave propagates in the x-direction only, σ_x and σ_x^* are matched according to the matching condition, $\sigma_y = \sigma_y^* = 0$ and $\sigma_z = \sigma_z^* = 0$. Similarly, when a

wave propagates in the y or z-direction only, the conductivity values that are not in the direction of propagation are set equal to zero. At the corner regions where there is overlap of two PML lattices, four losses are non-zero (for example, σ_x, σ_x^* and σ_y, σ_y^*). At the corner regions where there is overlap of three PML lattices, six losses are non-zero (σ_x, σ_x^*, σ_y, σ_y^* and σ_z, σ_z^*).

A PML layer is defined by three parameters: the number of cells (thickness), the kind of conductivity scaling and the theoretical reflection coefficient at normal incidence, $R(0)$.

4.2.1 Conductivity Scaling

In the above equations, the electric and magnetic conductivity values satisfy the matching impedance condition. With that treatment, theoretically there is no reflection at the vacuum-layer interface. Nevertheless, the layer does have a reflection since the outgoing waves are reflected by the perfectly conducting conditions set on its outer boundary and they can return into the vacuum. So for a plane wave, an apparent reflection is defined which is a function of the layer thickness δ and a conductivity profile $\sigma(\rho)$. This conductivity is either σ_x in a layer normal to x, σ_y in a layer normal to y, or σ_z in a layer normal to z [33,34].

The reflection factor at an angle of incidence θ is

$$R(\theta) = [R(0)]^{\cos\theta}$$
$$R(0) = e^{-\frac{2\delta\varepsilon_r}{\varepsilon_o c}<\sigma_i>} \tag{53}$$
$$<\sigma_i> = \frac{1}{\delta}\int_0^{\delta}\sigma(\rho)d\rho$$

From these equations, the average conductivity is:

$$<\sigma_i> = -\frac{\varepsilon_o c\, ln(R(0))}{2\sqrt{\varepsilon_r}\delta} \tag{53a}$$

Theoretically, one can obtain reflection factors as short as required by increasing the thickness δ or the conductivity $\sigma(\rho)$, or both. In practice, a small amount of numerical reflection occurs which depends on the choice of δ and $\sigma(\rho)$.

For the microstrip geometry, ε_r is inhomogeneous, causing an ambiguity in the above equation. This problem can be solved applying quasi-static theory to determine the effective dielectric constant of the structure. Therefore ε_r represents the effective dielectric constant of a multi-layer space.

4.2.1.1 Polynomial Scaling

For a polynomial scaling of the conductivity [33,34],

$$\sigma(\rho) = \sigma_o(\rho/\delta)^n \tag{54}$$

Typically, n in the range between 2 and 4 has been found to be suitable for the analysis of microstrip antennas. For an N-cell layer, the reflection coefficient factor at normal incidence is

$$R(0) = e^{-\frac{2\sigma_o \varepsilon_r \delta}{\varepsilon_o c(n+1)}} \tag{55}$$

The conductivity σ_o can be obtained from the above equation as follows:

$$\sigma_o = -\frac{\varepsilon_o c(n+1)}{2\sqrt{\varepsilon_r}\delta} \ln R(0) \tag{56}$$

The conductivity at the mesh points is implemented as the average value in the cell around the index location. At index i, the

$$\sigma_n(i) = \frac{1}{\Delta} \int_{\rho(i)-\Delta/2}^{\rho(i)+\Delta/2} \sigma(u) du \tag{57}$$

Therefore:

$$\begin{aligned} \sigma_n(0) &= -\frac{\varepsilon_o c \ln(R(0))}{2^{n+2}\Delta \cdot N^{n+1}} \\ \sigma_n(i>0) &= \sigma_n(0)\left[(2i+1)^{n+1} - (2i-1)^{n+1}\right] \end{aligned} \tag{58}$$

Berenger showed that for solving wave-structure interaction problems, the PML layer must satisfy two constraints. First, the FDTD conductivity $\sigma_n(0)$ is bounded by

$$\sigma_n(0) < \frac{2\pi\varepsilon_o}{D_c} \tag{59}$$

where D_c is the duration of the computation (number of time steps times Δt); second, the ratio of successive conductivity values must be lower than a value S, i.e.:

$$\frac{\sigma_n(i+1/2)}{\sigma_n(i)} \leq S \tag{60}$$

For polynomial scaling, the above ratio is not constant and depends on the position in the PML layer. Therefore, polynomial scaling is not an optimum profile of conductivity since it could result in a needlessly thickness of the PML layer.

Nevertheless, since all its parameters can be determined easily, the FDTD simulation can be set to run at least for a time

$$D_c = \frac{2\pi\varepsilon_o}{\Theta \cdot \sigma_n(0)} \tag{61}$$

The value Θ has been determined empirically to be about 10 for a parabolic conductivity profile (polynomial scaling with $n=2$).

4.2.1.2 Geometrical Scaling

To reduce the numerical reflections from the PML-interface, layers with conductivity increasing geometrically can be used. Denoting by Δ the spatial increment of the FDTD mesh and σ_o the conductivity in the vacuum-layer interface, such conductivity profiles are [33,34]:

$$\sigma(\rho) = \sigma_o (g^{\frac{1}{\Delta}})^{\rho} \tag{62}$$

so that the conductivity increases by the factor g from one cell to the next. For an N-cell layer, the reflection coefficient factor at normal incidence is

$$R(0) = e^{-\frac{2}{\varepsilon_o c}\frac{g^N - 1}{\ln(g)}\sigma_o \varepsilon_r \Delta} \tag{63}$$

The conductivity σ_o can be obtained from N, g and $R(0)$ as follows:

$$\sigma_o = -\frac{\varepsilon_o c}{2\sqrt{\varepsilon_r}\Delta}\frac{\ln(g)}{g^N - 1}\ln R(0) \tag{64}$$

The conductivity at the mesh points is implemented as the average value in the cell around the index location. Therefore:

$$\sigma_n(0) = \sigma_o \frac{\sqrt{g} - 1}{ln(g)}$$
$$\sigma_n(i > 0) = \sigma_o \frac{g - 1}{\sqrt{g}\, ln(g)} g^i \tag{65}$$

The ratio S of equation (60) is constant and equal to $\sqrt{g}$. Therefore, for solving wave-structure interaction problems, geometrical scaling is the optimum profile of conductivity. Once g is known, an approximate number for the duration of the simulation can be obtained from equation (61).

4.2.1.3 PML parameter selection

From equation (53), it is clear that inside the PML region the field decays as $e^{-\delta/d}$ where $d = \frac{\varepsilon_o c}{2 < \sigma_i > \sqrt{\varepsilon_r}}$. The cell size in the PML region is chosen to be a fraction m of this decay length d. Thus, $d = m \cdot \Delta$.

Therefore, the average conductivity becomes:

$$< \sigma_i > = \frac{\varepsilon_o c}{2\sqrt{\varepsilon_r} m \cdot \Delta} \tag{66}$$

Using the above equation and equation (53a) yields

$$m = -\frac{N}{\Delta} \tag{67}$$

A reasonable value for m has been obtained through extensive experimental study. In a broad range of applications, an optimal choice for a 10 cell thick PML is $R(0) \approx e^{-16}$. Therefore, $m \approx 10/16$. The larger the value of m, the thicker the PML will be. Typically, m takes a value of 1.

Based upon the desired reflectivity $R(0)$ and the value of m, $<\sigma_i>$ is calculated in equation (66) and it is straightforward to show from equation (53) that the length of the PML in meters is determined to be:

$$\delta = -\frac{\varepsilon_o c \cdot ln(R(0))}{2\sqrt{\varepsilon_r}<\sigma_i>} \tag{68}$$

therefore, the PML will have a thickness $N = \delta/\Delta$ cells. Typically, PML has a thickness of 7, 9 or 16 layers.

Using equation (53), it can be shown that for polynomial scaling, the maximum conductivity obtained is:

$$\sigma_o = (n+1)<\sigma_i> \tag{69}$$

And for geometrical scaling, the maximum conductivity is:

$$\sigma_o = \frac{N\,ln(g)}{g^N - 1} < \sigma_i > \tag{70}$$

The value of g can be calculated solving simultaneously the above equation with (61) and (65), yielding:

$$\frac{g^N - 1}{\sqrt{g} - 1} = N < \sigma_i > \frac{\Theta \cdot D_c}{2\pi\varepsilon_o} \tag{71}$$

Although at this point the duration of the computation is unknown, a first-order estimate can be obtained assuming that it is equal to that of the parabolic profile.

4.3 Circular Elements

The Cartesian FDTD method uses a spatial division in discrete cells such that the electrical properties are constant throughout the individual grid cells, and changes in these properties can be represented as discrete changes at the grid cell boundaries. Since all conductor boundaries are defined along the grid cells, curved surfaces cannot be represented precisely and can be typically approximated by a 'staircase' boundary.

Abarbanel and Ditkowski [19] proposed an approach known as the simultaneous approximation term (SAT) method, which adds a penalty term that accounts for the shape of the body. For normal 'stair-casing', the grid cells at the bounding contours can have portions outside of the domain of integration, whereas for SAT all of the grid cells are entirely within the computational domain. Through experimental study, it is determined

that as the mesh is refined, the 'normal stair-casing' technique yields only first-order accuracy. However, the SAT approach can reach almost third-order accuracy. The error of the SAT scheme is usually about 1/100 or less of the error due to 'stair-casing'.

So, in this dissertation the circular boundaries are approximated using 'stair-casing', but making sure that all the grid cells representing an electric conductor are entirely within the circular area covered by the patch.

4.4 Radome Coverings

A radar dome, or radome, is a protective dielectric housing for a microwave or millimeter wave antenna. The function of the radome is to protect the antenna from adverse environments in ground-based, shipboard, airborne and aerospace applications while having insignificant effect on the electrical performance of the enclosed antenna or antennas. The frequency band of application for radomes is approximately from 1 to 1000 GHz [6].

Radomes are generally composed of low-loss dielectrics of thickness comparable to a wavelength which are shaped to cover the antenna and, if necessary, to conform to aerodynamic streamlining.

A multi-layered antenna can be modeled using the FDTD method (Figure 11). It is important to study the radome covering to a) determine the effects of the superstrate on the resonance and input impedance on a single stacked element and b) build an accurate model for a single element before the array environment is tackled.

In this dissertation, the radome covering is reduced to the case of a dielectric covered microstrip antenna, assuming that the dielectric layer thickness is larger than the cell-size used to divide the FDTD computational domain into discrete cells.

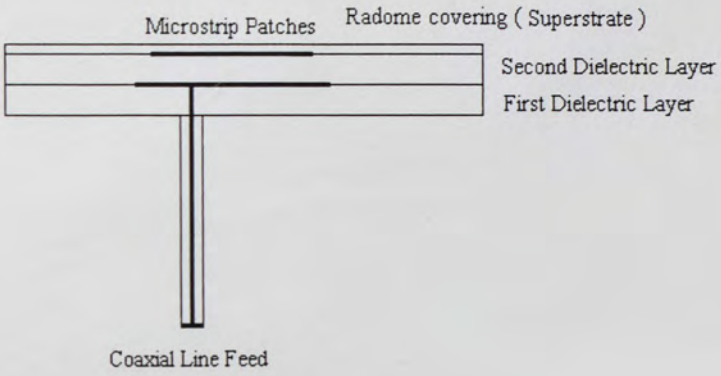

Figure 11. Single microstrip stacked element with a superstrate.

4.5 Radiation Pattern Analysis

The fields calculated with FDTD are only within the computational space and therefore the FDTD calculations only produce information of the electromagnetic fields that are adjacent of within the radiating object. However, FDTD can also be applied to analyze radiation from antennas, with the desired results being the far zone scattered or radiated fields that lie outside the FDTD space. This can be accomplished through the use of the equivalence principle, where the near field information is used to obtain the equivalent tangential electric and magnetic currents. These currents are then transformed into the far field region to obtain the radiated field [40-46].

There are four near-zone to far-zone transformations that can be used to obtain the radiation pattern of an antenna:

1) Single-frequency far-zone calculations. With a sinusoidal time-harmonic source being specified, the FDTD calculations are stepped through time until steady-state conditions are reached. The complex time-harmonic electric and magnetic currents flowing on a closed surface surrounding the object are then obtained. This involves very little computer storage, being four complex tangential fields (two electric fields and two magnetic fields) or surface currents for each Yee cell face on the closed surface. If these complex fields or currents are written to disk, then in post-processing the far zone radiated fields can be calculated in any direction. This is a good method to apply when far zone radiation or scattering patterns are desired at only one frequency [16].
2) Multiple-frequencies hybrid approach. It uses pulsed excitation for the FDTD calculations, but supplies frequency domain far zone fields. For each frequency of interest a running discrete Fourier transform (DFT) of the time harmonic tangential fields (surface currents) on a closed surface surrounding the FDTD geometry is updated at each time step. The running DFT provide the complex frequency domain currents for any number of frequencies using pulse excitation for the FDTD calculation. This is more efficient than using time harmonic excitation, which requires a separate FDTD calculation for each frequency of interest. It requires no more computer storage (per frequency) for the complex surface currents than the frequency domain far zone transform described above, and like it, provides frequency

domain far zone fields at any far zone angle. If far zone results are desired at a few frequencies, then the running DFT approach seems to be the optimum choice [16].

3) Full time domain approach. This is the most straightforward approach, it requires saving the time domain tangential fields (surface currents) over a closed surface containing the FDTD geometry for all time steps. Transient far zone fields can be computed in post-processing for all angles, and frequency domain results are computed using Fast Fourier Transforms (FFT) for all frequencies at all angles. This method is extremely versatile, it provides all possible far zone results available from the FDTD calculation; however, except for a very small geometry (thin plates or wires), a large amount of computer storage is required to save all the surface current components at all the time steps. Therefore, it does not seem to be a practical approach.

4) Transient far-zone fields for discrete angles. In many situations, transient and/or broadband frequency domain results are required at a limited number of angles, for example, transient antenna radiation for a limited number of pattern cuts. For these situations it is better to directly compute the transient far zone fields at each angle of interest as a running summation. This approach requires storing transient results for each time step for six far zone far zone vector potentials per far zone angle rather than four tangential field components (surface currents) per cell face on the transformation surface. If frequency domain results are desired they can be efficiently obtained from the far zone transient results with application of the FFT. In this way one FDTD computation using pulse excitation along with an FFT produces wide-band far zone scattering or radiation results at one specific angle [16,40,41].

The all-frequency-domain method described above is less efficient than the running DFT if results at more than one frequency (at all angles) are desired. The running DFT method requires more computational effort than the all-time-domain approach if far zone results are desired at more than a few frequencies and at all angles. The transient approach at discrete angles is much more efficient in its use of memory than the full-transient approach, if a broadband response is necessary for only a few discrete angles [16].

In this dissertation, the DFT approach described above has been chosen because of its ability to deliver results at all angles for desired frequency values. The frequency values chosen are the center frequency and two lateral bands within the operational bandwidth of the microstrip antenna.

The Fourier Transform of a complex and single-valued function $f(t)$ is defined as [17]

$$F(\omega) = \int_{-\infty}^{\infty} f(t) e^{-j\omega t} dt \tag{72}$$

where t and ω are real variables and j is the imaginary unit. If t designates the time in seconds, then ω designates the angular frequency in radians per second. The Discrete Fourier Transform (DFT) is obtained evaluating the integral at N discrete points $\{f_o, f_1, \ldots, f_{N-1}\}$ resulting in a sequence of complex values $\{F_o, F_1, \ldots, F_{NF}\}$ where NF is the desired number of frequency values:

$$F_k(k\Delta\omega) \approx \Delta t \sum_{n=0}^{N-1} f_n(n\Delta t) e^{-j \cdot k\Delta\omega \cdot n\Delta t}$$
$$k = 0,1,\ldots, NF \tag{73}$$

Using $\Delta\omega = 2\pi\Delta f$ and $\Delta f = \frac{1}{N\Delta t}$, this summation can also be written as:

$$F_k(k\Delta\omega) \approx \Delta t \sum_{n=0}^{N-1} f_n(n\Delta t) e^{-j\frac{2\pi \cdot k \cdot n}{N}} \tag{74}$$

The function $f_n(\Delta t)$ represents the discrete time-domain field values obtained through the FDTD computations, n is the time step index, N is the length of the DFT summation, $\Delta\omega$ and Δt are the frequency and time resolutions respectively, k is the frequency index. The transformation $F_k(k\Delta\omega)$ is the complex quantity that provides the magnitude and phase information at the frequency $k \cdot \Delta\omega$. The value $N = \frac{1}{\Delta f \Delta t}$ must be greater than or equal to N_{FDTD}, the number of time steps of the FDTD computation.

The frequency resolution $\Delta\omega$ is chosen to be consistent with the sampling-theorem. If $N \cdot \Delta t$ is the total time duration, then a frequency resolution of $\Delta\omega \leq \frac{\pi}{N\Delta t}$ must be used to obtain an alias-free spectrum.

In order to obtain the near-field data for the microstrip antennas, the DFT summation given above is updated at every FDTD time step, and the final values are normalized by the DFT of the incident pulse. The complex value $F_k(k\Delta\omega)$ must be

stored for every field components at each frequency of interest and at every cell where the frequency response is calculated. For single frequency calculation, the storage overhead for pulsed FDTD is smaller than for continuous wave (CW) FDTD. The overhead for pulsed FDTD increases linearly with the number of frequencies.

It is worth noting that the DFT algorithm is more efficient than the Fast Fourier Transform (FFT) algorithm for computing the frequency response from pulsed FDTD when only a limited number of available frequencies are of interest. Since N must always be greater or equal to the number of FDTD time steps, therefore in all far-field computations N is taken equal to the FDTD time step.

The frequency domain near zone to far zone transformation is a well-known procedure [17]. If the radiating object is surrounded by a closed surface S', and if $\hat{n}$ is a unit vector normal to the surface, then the time harmonic equivalent surface electric and magnetic currents are $\vec{J}_s(\omega) = \hat{n} \times \vec{H}(\omega)$ and $\vec{M}_s(\omega) = -\hat{n} \times \vec{E}(\omega)$, where $\vec{H}(\omega)$ and $\vec{E}(\omega)$ are the radiated magnetic and electric fields at the surface.

The time harmonic far zone electric fields can be obtained as follows:

$$E_\theta(\theta,\phi) = j\frac{e^{-jkr}}{2\lambda_o r}\left(-\eta N_\theta + L_\phi\right)$$
$$E_\phi(\theta,\phi) = j\frac{e^{-jkr}}{2\lambda_o r}\left(-\eta N_\phi + L_\theta\right) \qquad (75)$$

where η is the impedance of free space, r is the distance from the origin to the far zone field point, λ_o is the wavelength at the frequency of interest, k is the wave number and, $N(\omega)$ and $L(\omega)$ are two time harmonic vector potentials defined as:

$$\vec{N}(\omega) = \iint_S \vec{J}_s(\omega) e^{jkr'\cos\psi} dS'$$
$$\vec{L}(\omega) = \iint_S \vec{M}_s(\omega) e^{jkr'\cos\psi} dS' \tag{76}$$

$$N_\theta(\theta,\phi) = \iint_S \left[J_x \cos\theta \cos\phi + J_y \cos\theta \sin\phi - J_z \sin\theta\right] e^{jkr'\cos\psi} dS'$$
$$N_\phi(\theta,\phi) = \iint_S \left[-J_x \sin\phi + J_y \cos\phi\right] e^{jkr'\cos\psi} dS'$$
$$L_\theta(\theta,\phi) = \iint_S \left[M_x \cos\theta \cos\phi + M_y \cos\theta \sin\phi - M_z \sin\theta\right] e^{jkr'\cos\psi} dS' \tag{77}$$
$$L_\phi(\theta,\phi) = \iint_S \left[-M_x \sin\phi + M_y \cos\phi\right] e^{jkr'\cos\psi} dS'$$

where S' is the closed surface surrounding the antenna.

Determining the tangential fields and surface currents can be illustrated by considering the contribution from a single FDTD cell. This cell lies on an arbitrary virtual closed boundary surface S', which separates the exterior infinite region and the interior region containing the antenna. The closed surface S' is chosen rectangular in shape to conform to the distinct planes of the FDTD lattice. Due to the nature of the Yee cell, the field values are not specified at the same surface of the cell. To determine the field values at the center of the cell faces on the integration surface, appropriate field values including those from nearby cells are spatially averaged.

As an example consider the electric field component E_x^n tangential to the transformation surface S' and at the center of a particular (i, j, k) Yee cell face. The field E_x^n must be found by appropriate spatial averaging of the E_x^n values at cell (i, j, k) and from adjacent cells. Assume that part of the integration surface under consideration has an outward unit normal vector $\hat{n} = \hat{a}_y$ (x-z plane). Then, at the center of the cell

$$E_x^n = \frac{E_x\big|_{i,j+1,k}^n + E_x\big|_{i,j+1,k+1}^n}{2} \tag{78}$$

The magnetic field components at the same point would require averaging four terms. The electric field component obtained above will produce the magnetic surface current

$$\bar{M}_s = -\hat{a}_y \times E_x^n \hat{a}_x = E_x^n \hat{a}_z \tag{79}$$

Therefore E_x^n on this cell contributes only to M_z, the surface of integration is $\Delta x \cdot \Delta z$ and the value of E_x^n is assumed constant over this surface. In order to keep track of the relative phase delay for each cell face on the integration surface, a spatial reference (i_c, j_c, k_c) must be located (the center of the Cartesian computational space would be an appropriate reference point). The vector from the reference cell to the center of the Yee cell face on the integration surface is

$$\vec{r}' = (i - i_c)\Delta x\hat{a}_x + (j + \frac{1}{2} - j_c)\Delta y\hat{a}_y + (k - k_c)\Delta z\hat{a}_z \qquad (80)$$

The value of $1/2$ is added because the integration surface of the (i, j, k) cell face under consideration is offset by $1/2$ cell in the y-direction away from the cell center. Similarly, a $\pm 1/2$ cell contribution must be considered for all the cell faces on the S' integration surface.

The complete structure far field data can be obtained by summing similar contributions from all the tangential field components on all of the cell walls lying on the integration surface.

4.6 Multiple Feeds for Circular Polarization

The rectangular and circular patches radiate primarily linearly polarized waves if conventional feeds are used with no modifications. However, circular and elliptical polarizations can be obtained using various feed arrangements or slight modifications made to the elements [47,48].

Circular polarization can be obtained if two orthogonal modes are excited with a 90° time-phase difference between them. This can be accomplished by adjusting the physical dimensions of the patch and using either single or two or more feeds, using rectangular or circular patches. Multiple feed schemes using coaxial probes are studied in this dissertation [47,48].

For a circular patch, circular polarization is achieved by using two feeds with proper angular separation. With an arrangement of two coaxial probes, each probe is always positioned at a point where the field generated by the other probe exhibits a null; therefore there is very little mutual coupling between the two probes. To achieve circular polarization, it is required that the two feeds are fed in such a manner that there is 90° time-phase difference between the fields of the two; this is achieved through the use of a 90° hybrid, as shown in Figure 12. A shorting pin is placed at the center of the patch to ground the patch to the ground plane; this is not necessary for circular polarization, however it is used to suppress modes with no ϕ variations and it may also improve the quality of the circular polarization [47,48].

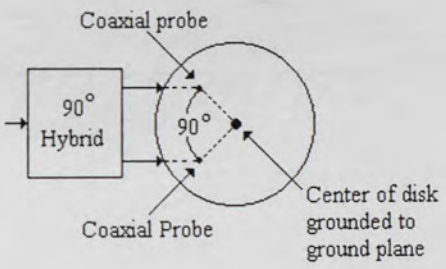

Figure 12. Circular patch fed with two coaxial probes.

For the dominant mode (TM^z_{110}) and for higher order modes (TM^z_{210}, TM^z_{010}, TM^z_{310}, TM^z_{410}, TM^z_{510}, TM^z_{610}, etc.), the spacing between the two feeds to achieve circular polarization is different. Furthermore, as it is seen in Figure 13, two additional feed probes located diametrically opposite to the original poles are usually recommended, in order to preserve symmetry and minimize cross polarization, especially for relatively thick substrates. The additional probes are used to suppress the neighboring (adjacent)

modes which usually have the next highest magnitudes. For the even modes (TM^z_{210} and TM^z_{410}), the four feed probes should have phases of 0°, 90°, 0° and 90°, while for the odd modes (TM^z_{110} and TM^z_{310}) they should have phases of 0°, 90°, 180° and 270° [47].

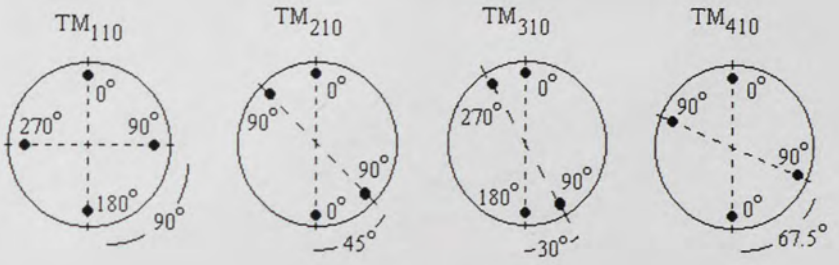

Figure 13. Circular patch feed arrangements for the dominant and higher-order modes.

In this dissertation, the focus will be kept on the dominant mode TM^z_{110} of the circular patch. A very simple and practical way of achieving circular polarization with a circular patch is by making it slightly elliptical or by adding small tabs on the perimeter (four tabs, 90° spaced from each other).

From the point of view of the FDTD geometry, this implies a more complicated structure and therefore more complexity and memory use. While feeding one coaxial line, the other probes must be terminated by an absorbing boundary condition in order to simulate the 50 ohms termination that is used in the experimental setup. Special care must be taken to simulate the holes that are made on the lower patch, when the inner conductors of the coaxial probes are feeding the upper patch. It is also necessary to model the shorting pin that is placed at the center of the patch to ground the patch to the ground plane, as well as the tabs that are used to achieve a better circular polarization.

5. RESULTS FOR MICROSTRIP ANTENNA ELEMENTS

In this section, the validation of the FDTD model discussed in the previous chapters is made. Several simulations were performed on different antennas that can be used in an array environment. Some representative results are presented here.

5.1 Rectangular Microstrip Patches

5.1.1 Single Layer Microstrip Patches

To demonstrate the validity of the coaxial feed model, a simulation has been performed on a single-layer microstrip patch consisting of a rectangular metal patch ($W = 25.1\ mm$, $L = 17.72\ mm$) on an infinite substrate ($\varepsilon_r = 2.33$, $h = 2.35\ mm$). The feed is located $4.86\ mm$ from the center of the antenna. The antenna was taken from [29].

For these calculations a nine-layer PML was used, geometrical conductivity scaling with $g = 4.0$ and a reflection coefficient at normal incidence $R(0) = 10^{-4}$. The computational grid size was $\Delta x = \Delta y = 0.432195\ mm$, $\Delta z = 0.391667\ mm$. The coaxial line length was 70 cells long and the voltage sampling point was located 10 cells away from the ground plane. The results are shown in Figures 14 through 17.

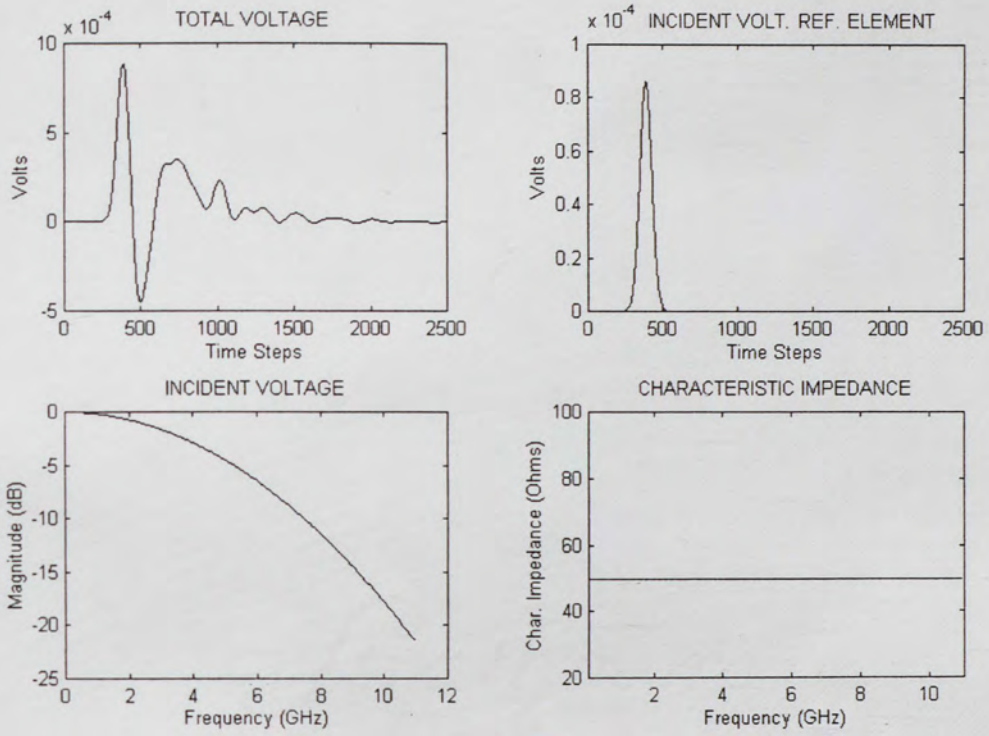

Figure 14. Single Layer Rectangular Patch: Coax-Feed Analysis.

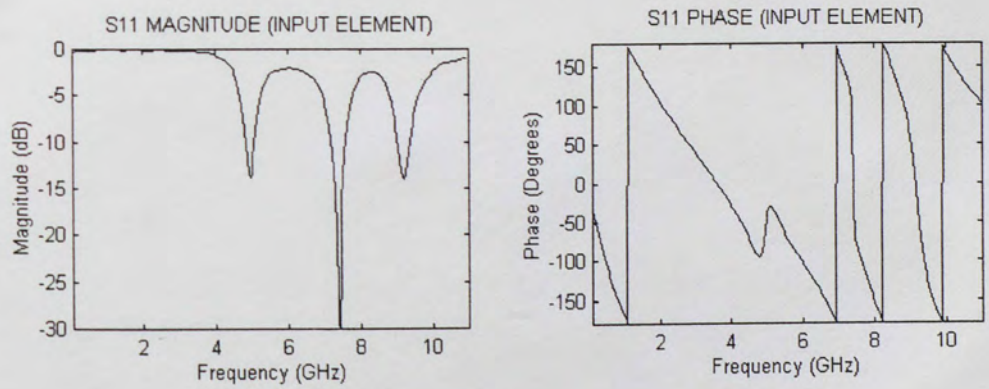

Figure 15. Single Layer Rectangular Patch: S_{11} Analysis.

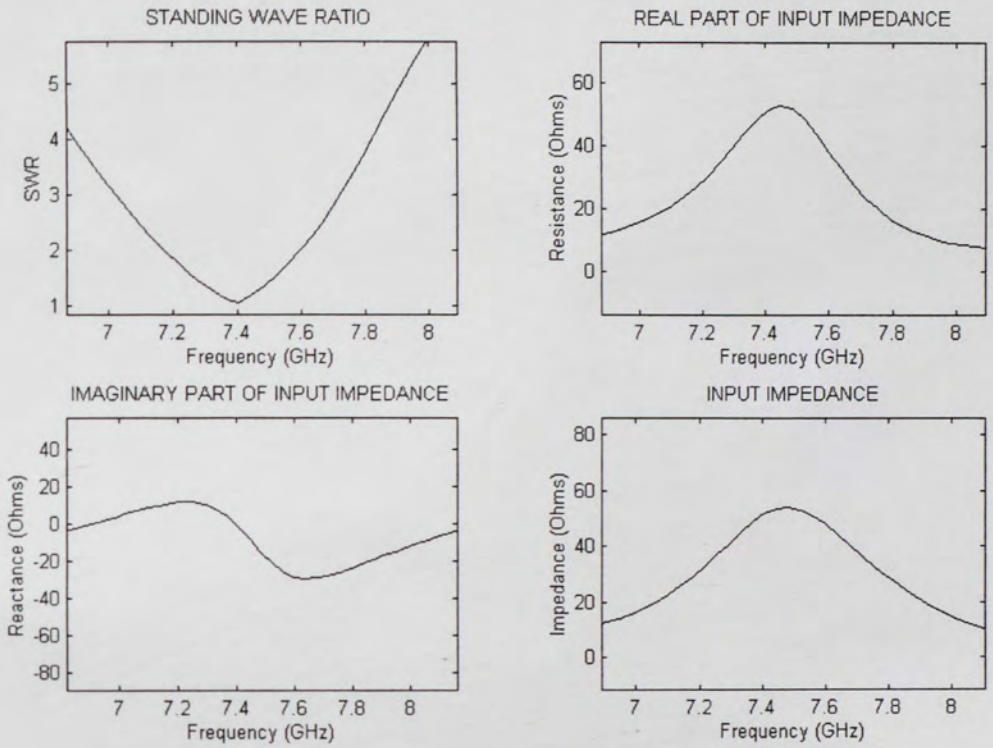

Figure 16. Single Layer Rectangular Patch: Impedance Analysis.

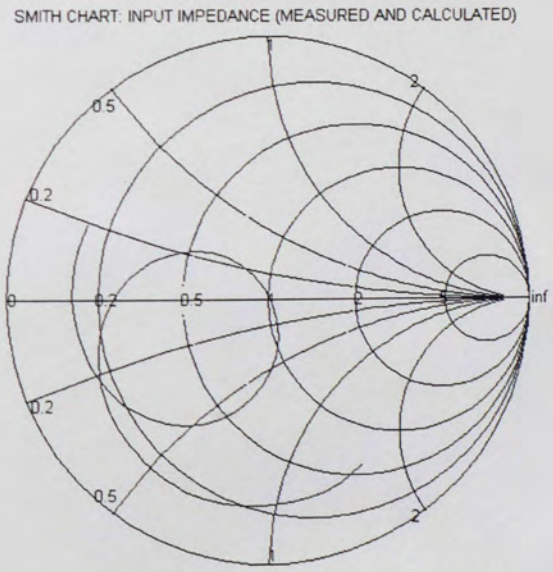

Figure 17. Single Layer Rectangular Patch: Impedance Analysis.

5.1.2 Stacked Microstrip Patches

Measurements were performed on a stacked antenna consisting of two square metal patches and a foam layer *($\varepsilon_r = 1.1$)* on top of a Rexolite substrate *($\varepsilon_r = 2.53$, tan $\delta = 0.00066$)*, with truncated dielectric layers. The coaxial probe is connected to the lower patch and the upper patch (parasitic) is excited through coupling from the main radiating patch. Figure 18 depicts a cross section of this antenna [49].

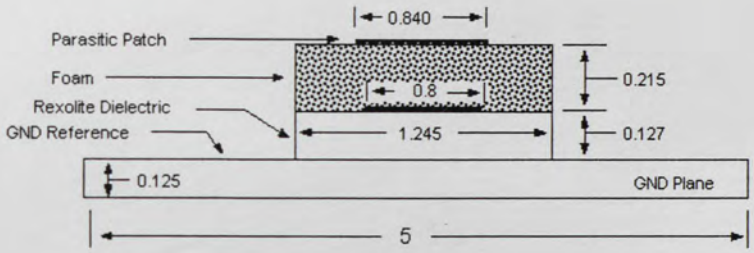

Figure 18. Layout of the antenna element used for the linear and planar array.

For these calculations a nine-layer PML was used, geometrical conductivity scaling with $g = 4.0$ and a reflection coefficient at normal incidence $R(0) = 10^{-4}$. The computational grid size was $\Delta x = \Delta y = 1.016\ mm$, $\Delta z = 0.80645\ mm$. The coaxial line length was 70 cells long and the voltage sampling point was located 10 cells away from the ground plane. Excellent agreement can be obtained in predicting the scattering parameters of the antenna. Figures 19 through 22 depict the comparison between the predicted and the measured results.

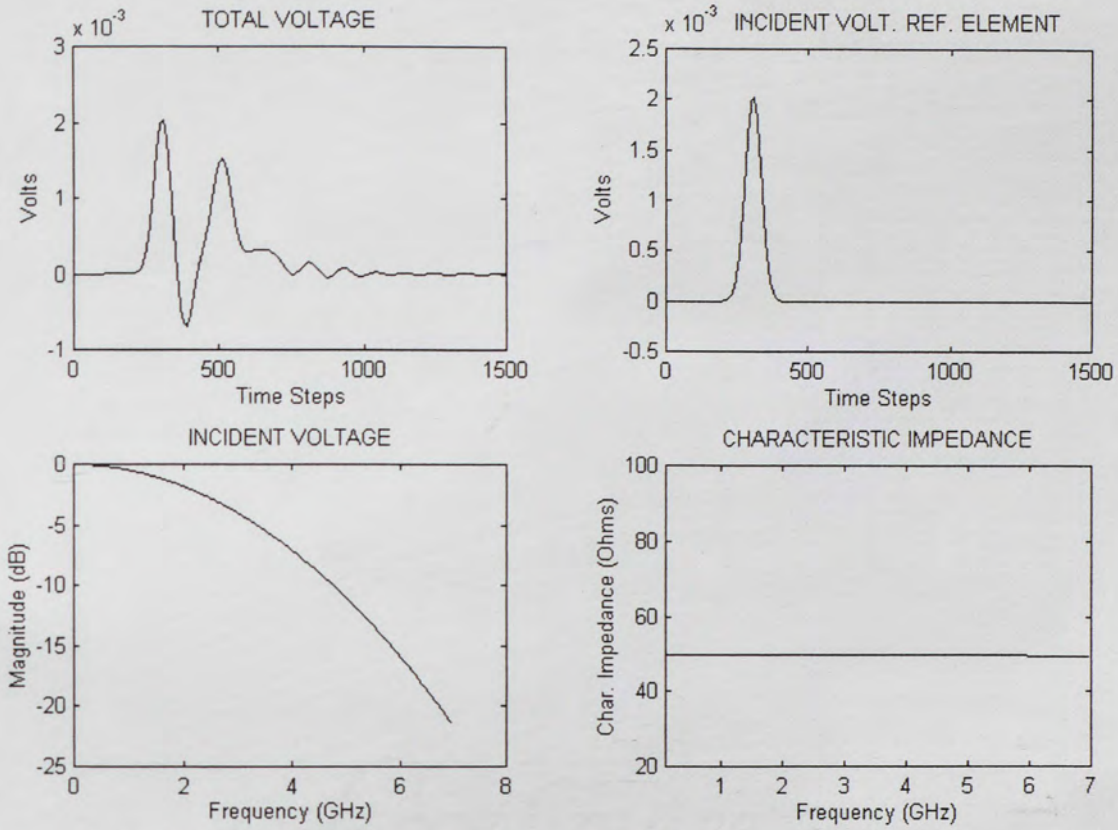

Figure 19. Stacked Rectangular Patches: Coax-Feed Analysis.

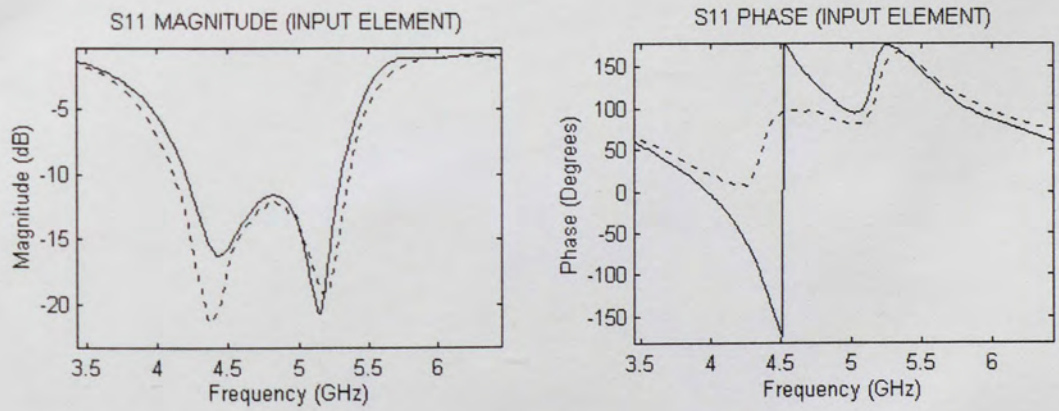

Figure 20. Stacked Rectangular Patches: S_{11} Analysis.

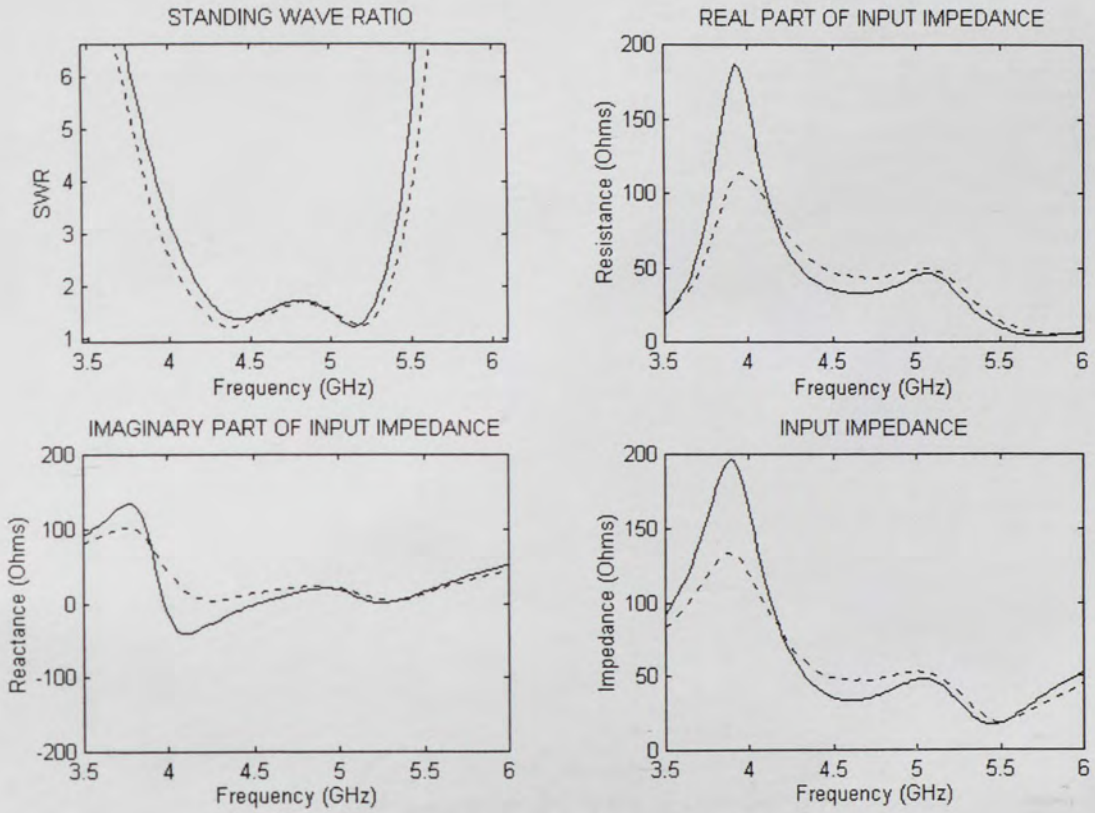

Figure 21. Stacked Rectangular Patches: Impedance Analysis.

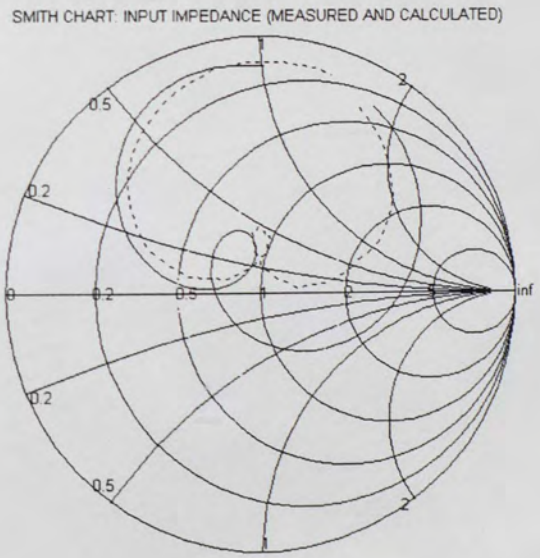

Figure 22. Stacked Rectangular Patches: Smith Chart Analysis.

5.2 Circular Microstrip Patches

A simulation was performed on a stacked antenna consisting of two circular metal patches and three dielectric layers. The bottom layer has $\varepsilon_r = 2.45$, $h = 1.5218$ *mm*. The middle layer has $\varepsilon_r = 1.22$, $h = 3.1759$ *mm*. The top layer has $\varepsilon_r = 2.45$, $h = 0.7609$ *mm*. The coaxial probe is connected to the lower patch and the upper patch (parasitic) is excited through coupling from the main radiating patch. The third dielectric layer is on top of the upper circular patch. The feed is located *7.9398 mm* from the center of the antenna [50].

For these calculations a nine-layer PML was used, parabolic conductivity scaling and a reflection coefficient at normal incidence $R(0) = 10^{-6}$. The computational grid size was $\Delta x = \Delta y = 0.378086$ *mm*, $\Delta z = 0.38045$ *mm*. The coaxial line length was 70 cells long and the voltage sampling point was located 10 cells away from the ground plane. Figures 23 through 26 depict the comparison between FDTD and Moment Method results.

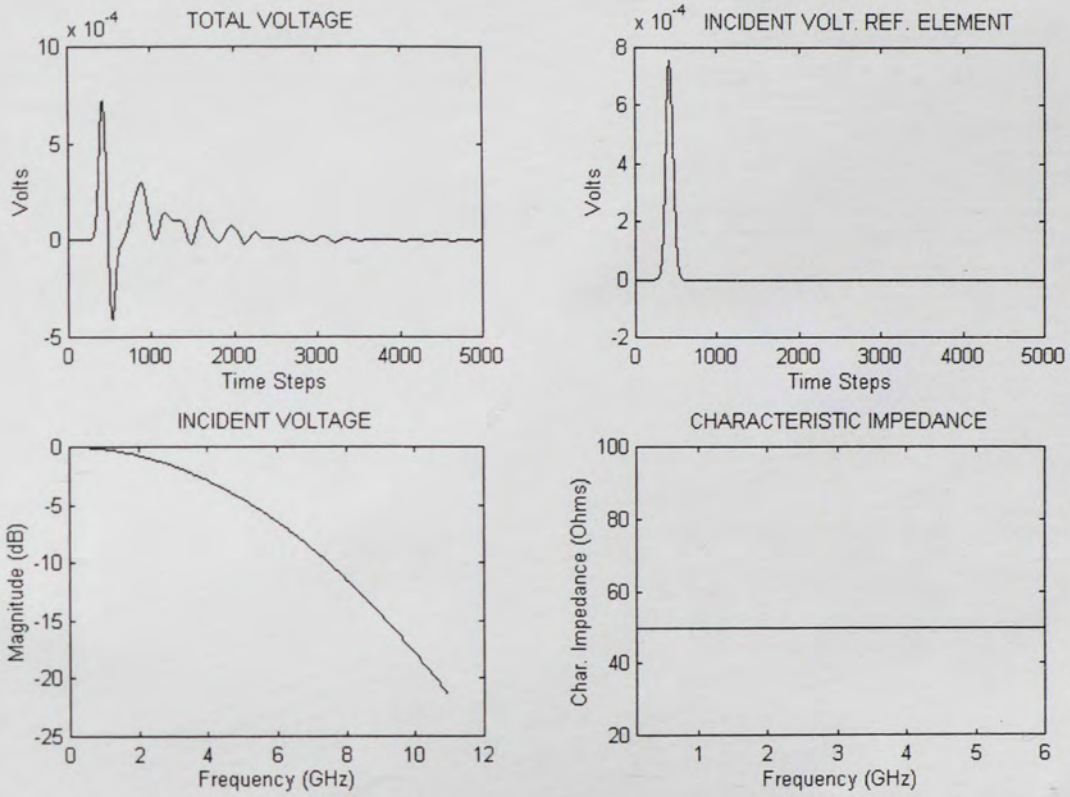

Figure 23. Stacked Circular Patches: Coax-Feed Analysis.

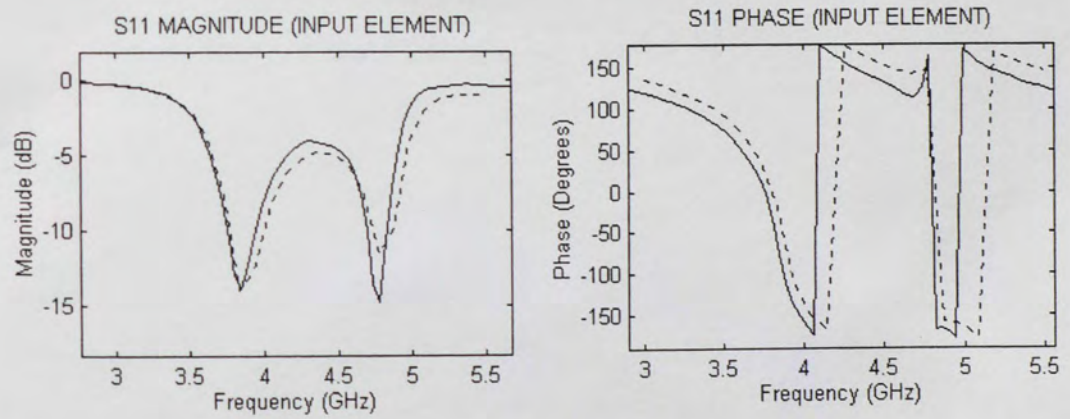

Figure 24. Stacked Circular Patches: S_{11} Analysis.

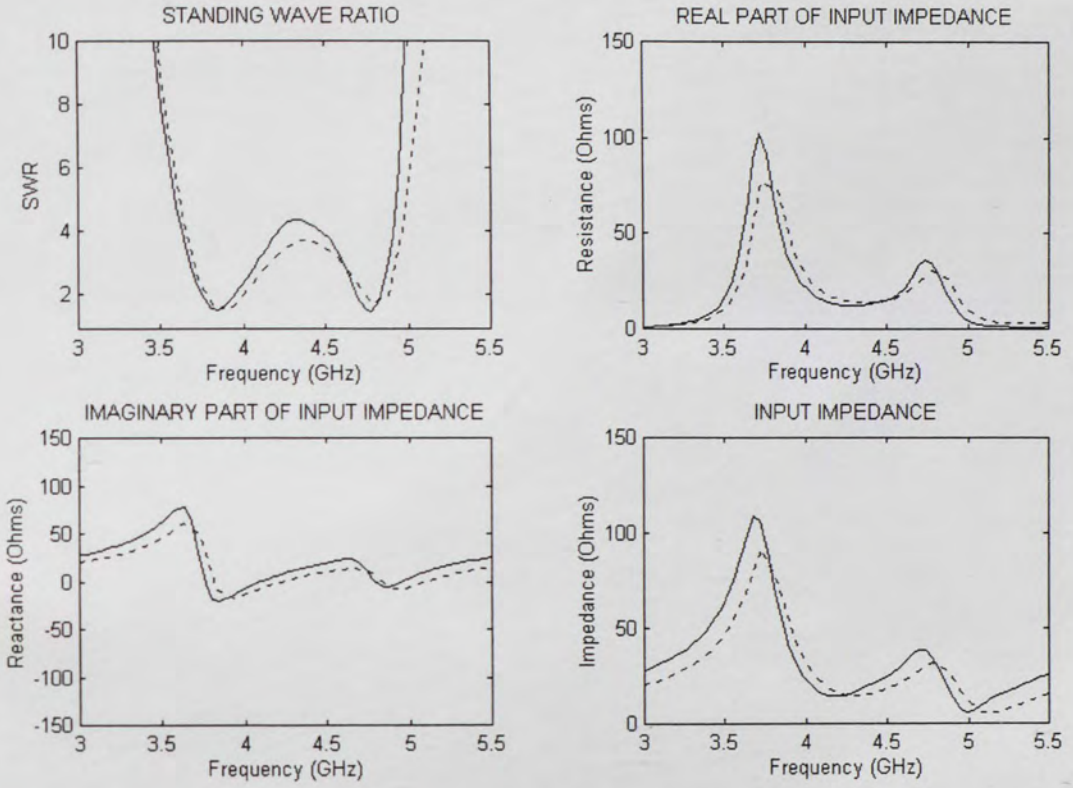

Figure 25. Stacked Circular Patches: Impedance Analysis.

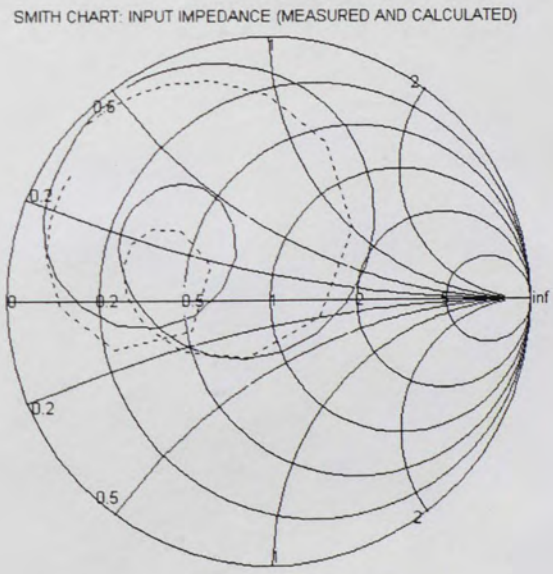

Figure 26. Stacked Circular Patches: Smith Chart Analysis.

5.3 Dual Coaxial Probe Feed

When a dual feed antenna is designed, the feed probe coupling cannot be neglected. The addition of a second probe results in an increase in the cross-polarization level. If an antenna is going to have dual-polarization, it is a common practice to place the probe with horizontal polarization in the null of the field distribution of the probe with vertical polarization, and vice versa. However, coupling is a complex phenomenon and it is not very easy to achieve the mentioned requirement. Usually, a coupling level of about -20 dB is acceptable.

5.3.1 S-Band Stacked Microstrip Element

The first simulation has only one feed. The results obtained for this antenna are presented here because the antenna will be modified to include two probes in the next section. The simulation was performed on a stacked antenna consisting of two stacked square patches; the dimensions are *40.005 mm* for the lower patch and *40.64 mm* for the upper patch. The bottom layer is made of Rexolite ($\varepsilon_r = 2.5,\ h = 6.35\ mm$). A foam layer ($\varepsilon_r = 1.05,\ h = 12.7\ mm$) is placed on top. The coaxial probe is connected to the lower patch and the upper patch (parasitic) is excited through coupling from the main radiating patch. The feed is located *18.0975 mm* from the center of the antenna [51-52].

For these calculations a nine-layer PML was used, parabolic conductivity scaling and a reflection coefficient at normal incidence $R(0) = 10^{-6}$. The computational grid size was $\Delta x = \Delta y = 1.6002\ mm$, $\Delta z = 1.5875\ mm$. The coaxial line length was 70 cells long

and the voltage sampling point was located 10 cells away from the ground plane. Figures 27 through 30 depict the results predicted with FDTD.

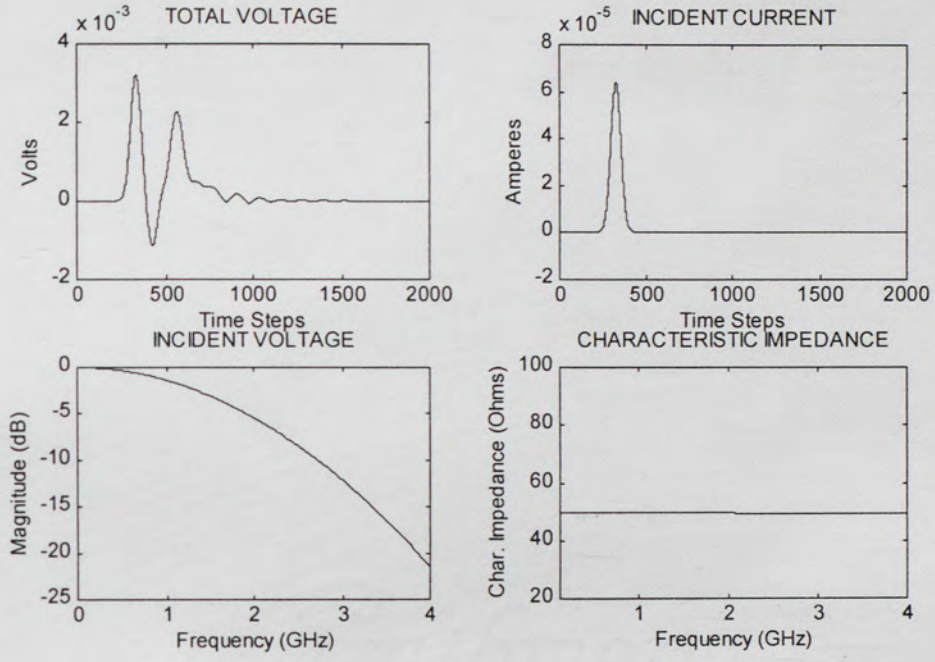

Figure 27. S-band Stacked Square Patches: Coax-Feed Analysis.

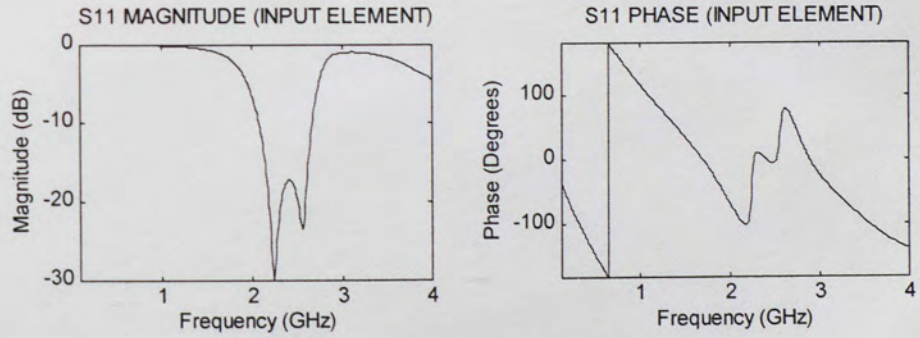

Figure 28. S-band Stacked Square Patches: S_{11} Analysis.

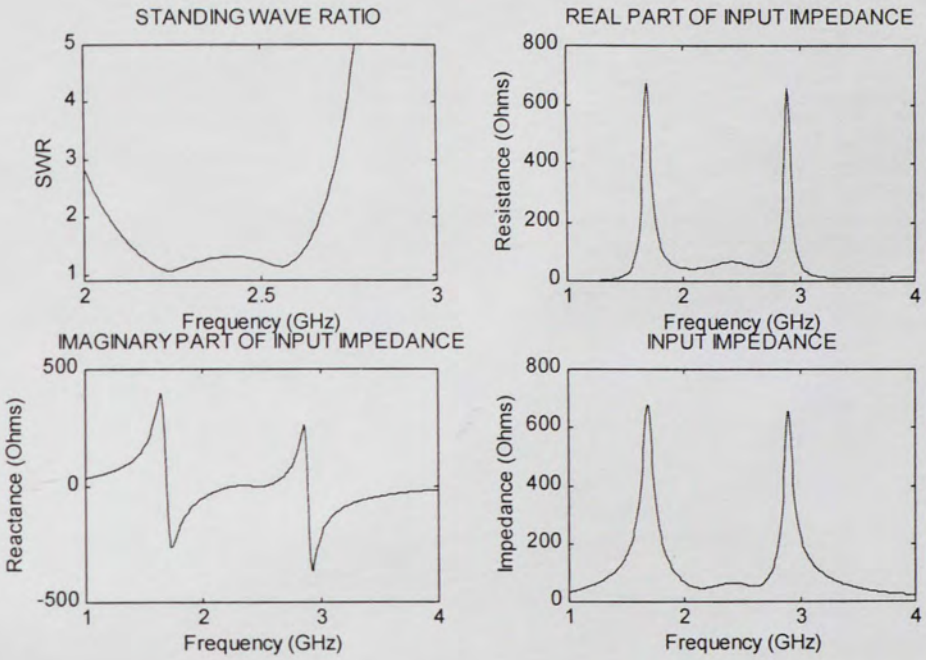

Figure 29. S-band Stacked Square Patches: Impedance Analysis.

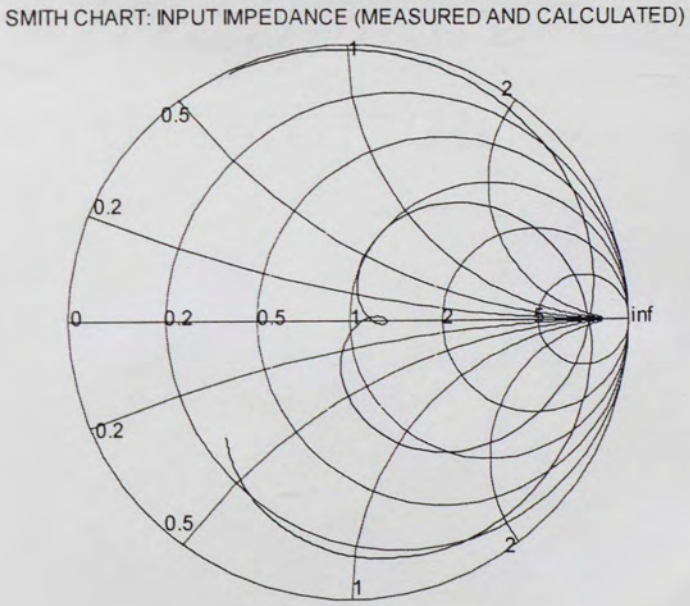

Figure 30. S-band Stacked Square Patches: Smith Chart Analysis.

5.3.2 Dual-Feed S-Band Rectangular Microstrip Antenna

The antenna described above was modified to include an additional feed for dual linear polarization. A way to reduce coupling between probes is to try to separate them. If a circular patch were to be used, it would require that the probes be separated 90 degrees for orthogonal polarization. If the probes were moved along the circumference, the requirement for dual orthogonal polarization would not be met. With a square patch, the probes can be moved laterally since there are no field variations in that dimension; therefore, coupling between probes can be drastically reduced, as well as the cross-polarization level. In this case, the probes are offset from the center of the patch by 0.045 inch. The results are depicted in Figure 31 and compare very well with measurements.

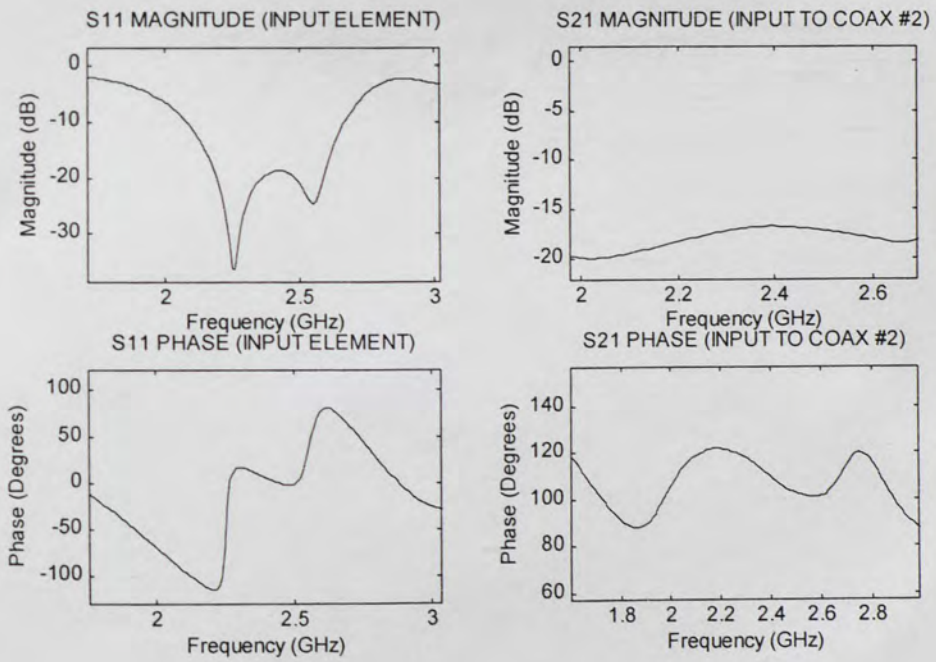

Figure 31. Dual-Feed Rectangular Patch: S_{11} and coupling between probes.

5.3.3 Dual-Feed L-Band Circular Microstrip Antenna

Finally, a simulation was performed on a stacked antenna consisting of two circular metal patches and two coaxial probes for circular polarization. The probe is connected to the upper patch through a hole in the lower patch. This is the kind of configuration used for dual-frequency operation. Both dielectric layers have $\varepsilon_r = 6$ and $\tan \delta = 0.0018$. The thickness of the lower layer is $6.35\ mm$, and $2.54\ mm$ for the upper layer. The feed is located $7.493\ mm$ from the center of the antenna [51,52].

For these calculations a nine-layer PML was used, parabolic conductivity scaling and a reflection coefficient at normal incidence $R(0) = 10^{-6}$. The computational grid size was $\Delta x = \Delta y = 0.732367\ mm$, $\Delta z = 0.635\ mm$. The coaxial line length was 70 cells long and the voltage sampling point was located 10 cells away from the ground plane. The results are shown in Figures 32 and 33.

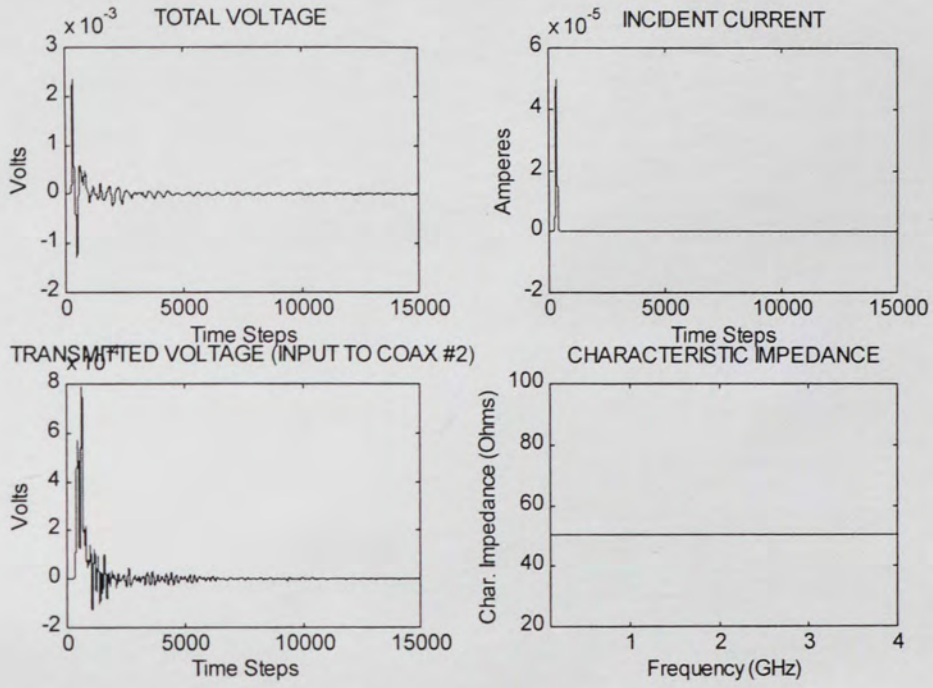

Figure 32. Dual-Feed Circular Patches: Coax-Feeds Analysis.

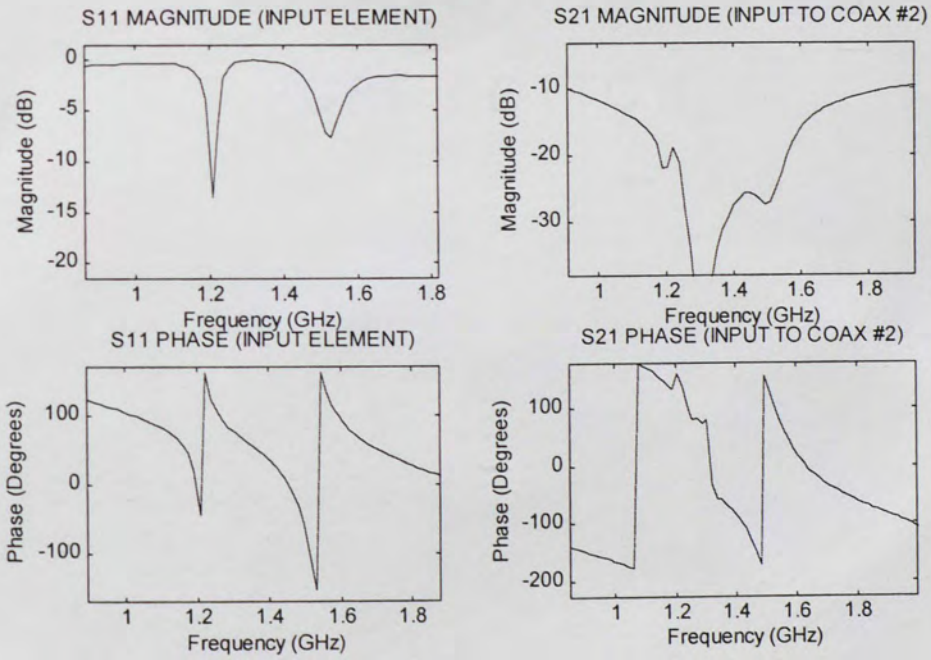

Figure 33. Dual-Feed Circular Patches: S_{11} Analysis.

6. RESULTS FOR MICROSTRIP ARRAYS

6.1 Mutual Coupling in Microstrip Array Antennas

It is very important to study the mutual coupling effects in Phased Array Antennas, especially when the array is going to be scanning. When an antenna is placed next to other antennas in an array environment, complex interactions occur between them. The current distribution of the antenna changes compared to the case when the antenna is isolated in free space. The current distributions vary on all of the array elements due to their mutual coupling, therefore changing the driving point impedance of each element. Coupling is also responsible of increased sidelobe levels, main beam squint, filled or shifted nulls, grating lobes and array blindness at some scan angles, and even improvement in sidelobe levels if tapering of the array distribution function occurs [53-66].

The calculation of mutual coupling among array elements is done using standard two-port network techniques. The scattering parameters are found by exciting one of the antennas and terminating the driving point of the others with 50 ohms. The S-parameters for an *N*-port network are defined as:

$$S_{ij} = \left. \frac{b_i}{a_j} \right|_{a_k=0, k=1..N, k\neq j} \tag{60}$$

where b_i is the reflected wave from port i and a_j is the incident wave at port j. The energy that is being coupled from element j into element i is represented by S_{ij}.

Using the explicit coaxial feed model described in Chapter 4, the 50 ohms matching for the passive array elements is accomplished through the use of an absorbing boundary condition at their excitation planes.

The FDTD Method is applied to analyze two 8-elements Linear Arrays (E-plane and H-plane configuration) as well as one 25-elements Planar Array. The arrays consist of Coax-fed Stacked Microstrip Antennas; they were built and tested in Raytheon E-Systems Inc. Figure 34 depicts the layout of the antenna element used for these arrays. This is one of the antennas that were studied in Chapter 5, and is repeated here.

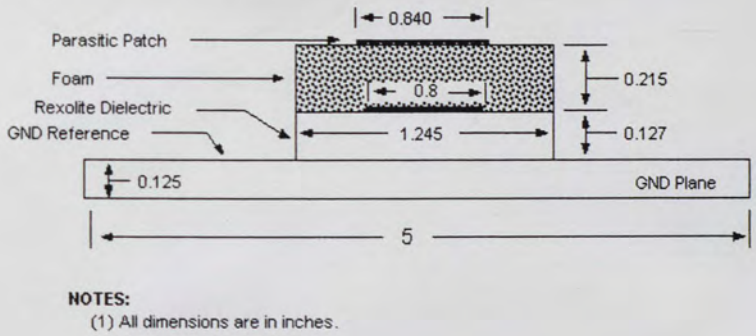

Figure 34. Layout of the antenna element used for the linear and planar array.

For these calculations, a nine-layer PML was used. The conductivity was varied using geometrical scaling with $g = 4.0$, and a reflection coefficient at normal incidence

$R(0) = 10^{-4}$. The computational grid size was $\Delta x = \Delta y = 1.016\ mm$, $\Delta z = 0.80645\ mm$. The coaxial line length was 70 cells long and the voltage sampling point was located 10 cells below the ground plane, inside the coaxial line. The S-parameters and input impedance are calculated and compared with measurements for the linear and planar arrays [53-57].

Figure 35 depicts the layout of the Linear Array configurations that were simulated. Figure 36 is the photograph of the actual array that was built. The results in Figures 37 through 41 are for the H-Plane configuration, and in Figures 42 through 44 for the E-Plane configuration. For the results that are shown, an incident Gaussian pulse is sent through element #4, while all other elements are terminated with an ABC. The voltage at element #5 is sampled. Therefore, S_{45} (the coupling from element #5 into element #4) is obtained.

Figure 45 depicts the layout of the Planar Array configuration that was simulated. Figure 46 is the photograph of the actual array that was built. An incident Gaussian pulse is sent through element #12, while all other elements are terminated with an ABC. The voltage at element #13 is sampled. Therefore, $S_{12\text{-}13}$ (the coupling from element #13 into element #12) is obtained. The results are shown in Figures 47 through 50.

Figure 35. Top view of: (a) Eight-element Linear Array (E-Plane configuration) (b) Eight-element Linear Array (H-Plane configuration).

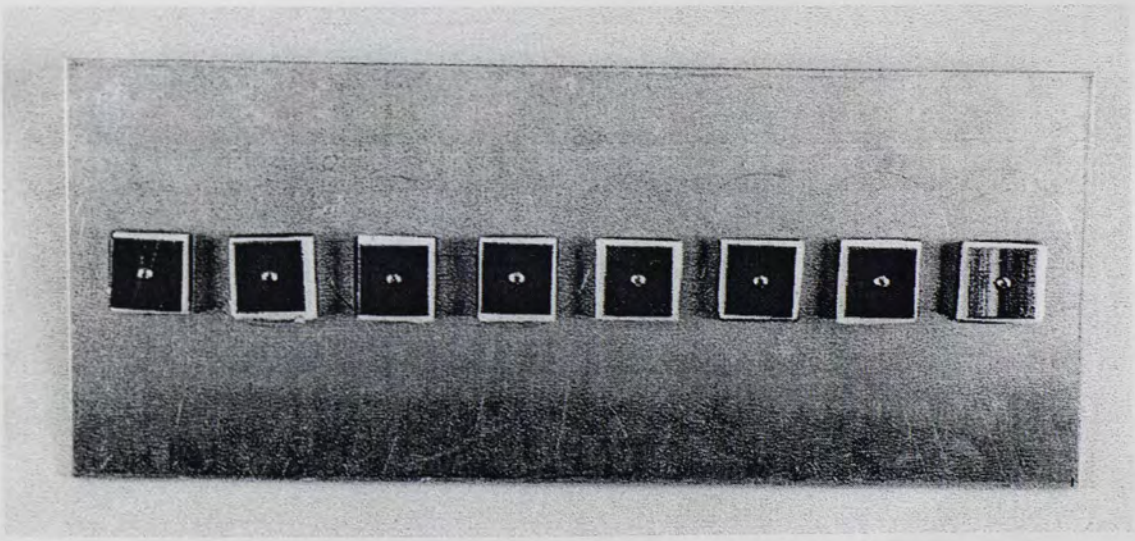

Figure 36. Photograph of the Eight-element Linear Array.

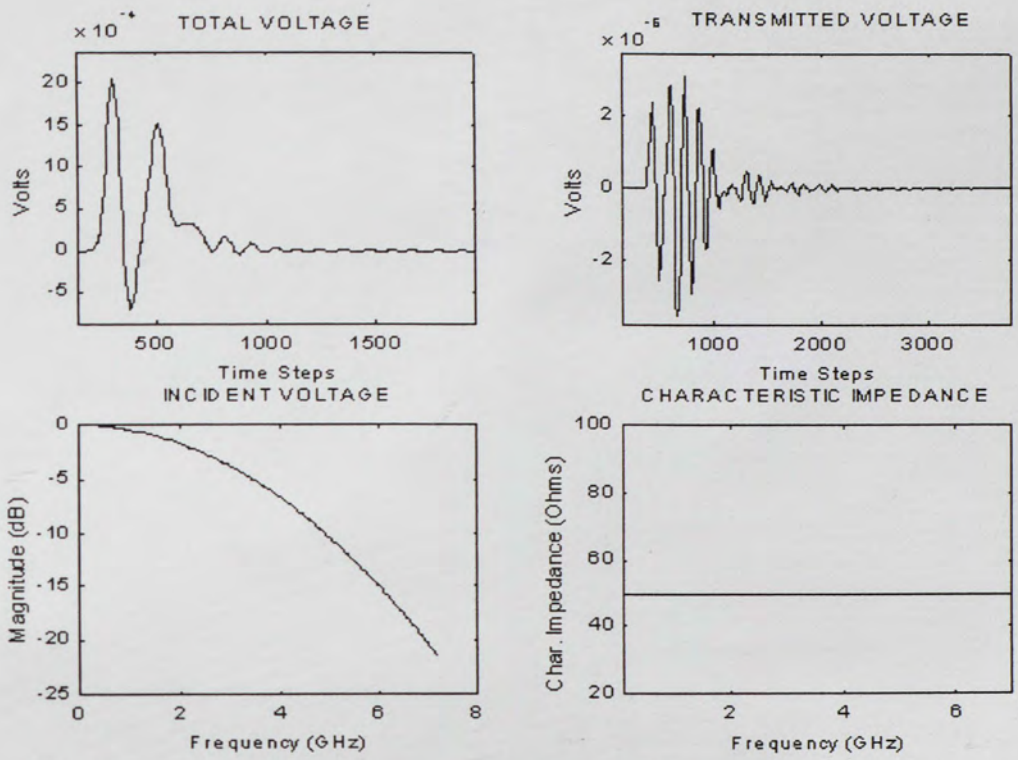

Figure 37. H-Plane Array Configuration: Coax-feed Analysis, elements #4 and #5.

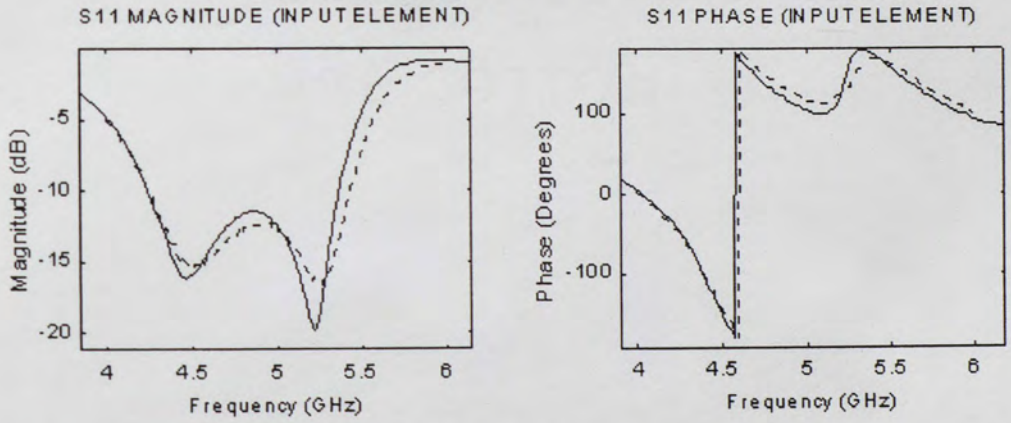

Figure 38. H-Plane Array configuration: S_{44} Analysis.

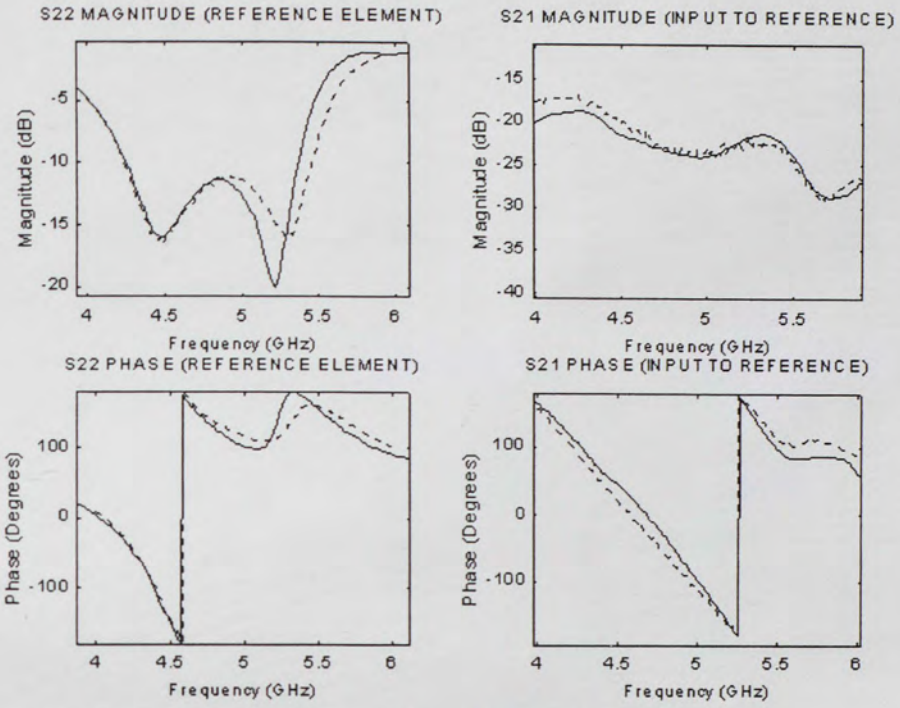

Figure 39. H-Plane Array configuration: S_{55} and S_{45} Analysis.

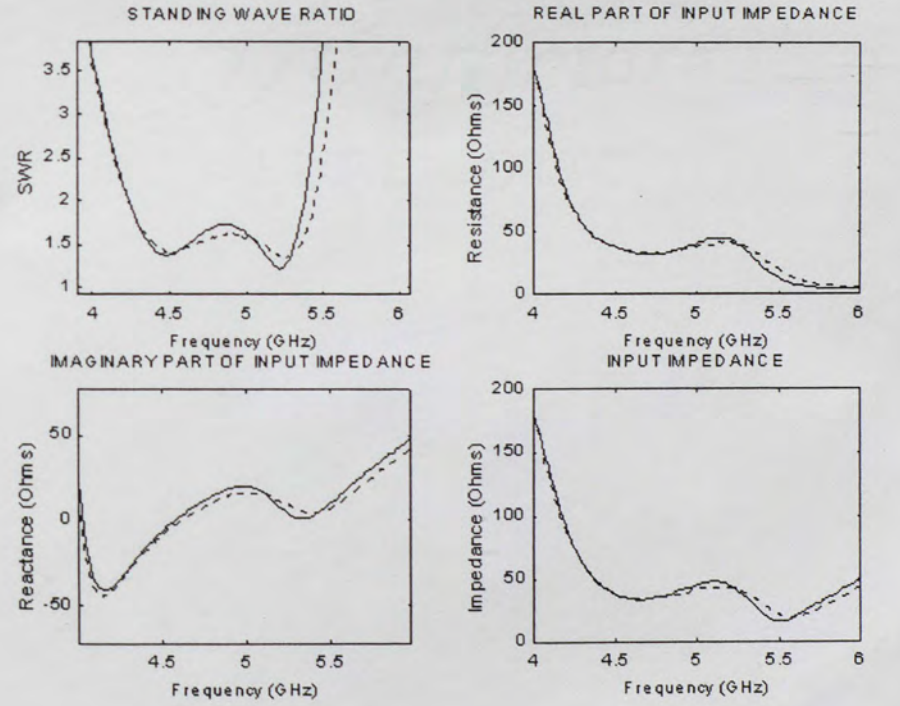

Figure 40. H-Plane Array configuration: Impedance Analysis, element #4.

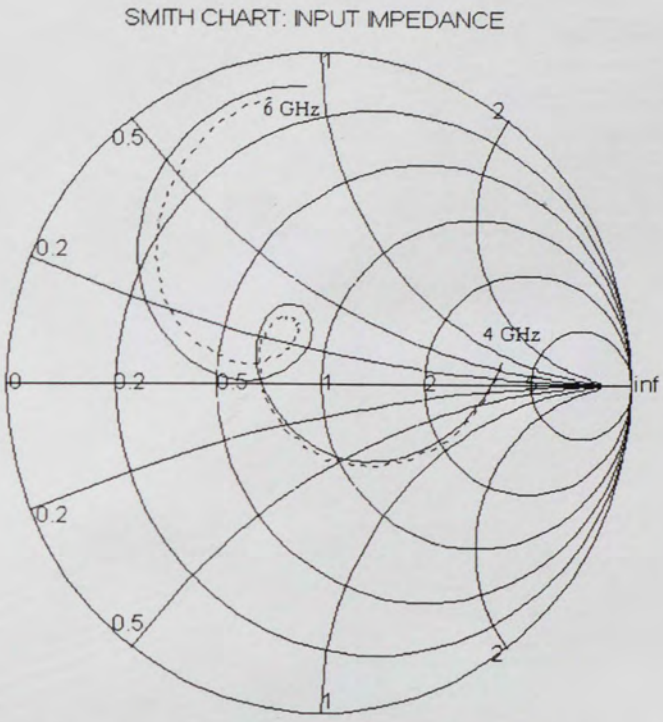

Figure 41. H-Plane Array configuration: Smith Chart Analysis, element #4.

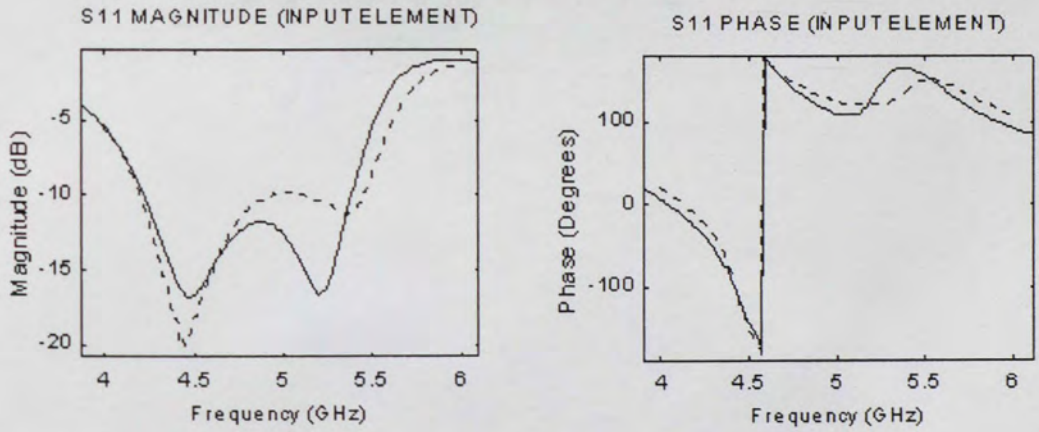

Figure 42. E-Plane Array configuration: S_{44} Analysis, element #4.

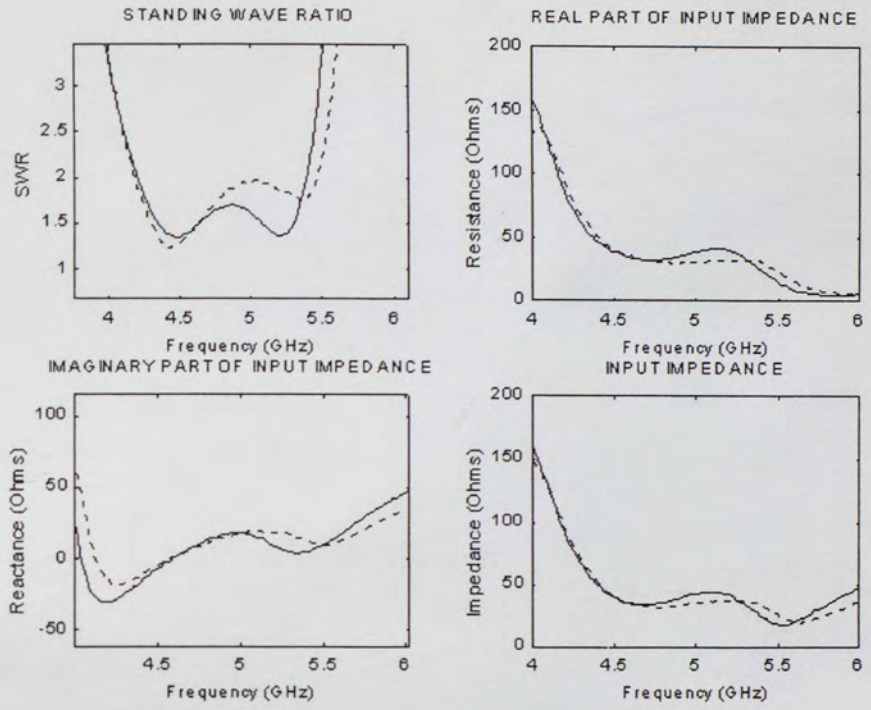

Figure 43. E-Plane Array configuration: Impedance Analysis, element #4.

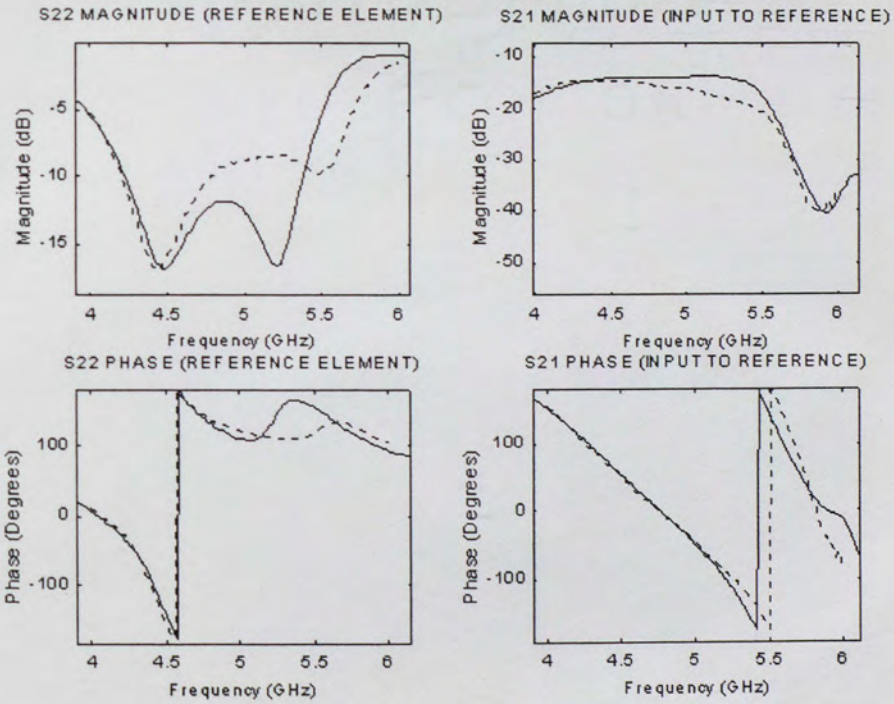

Figure 44. E-Plane Array configuration: S_{55} and S_{45} Analysis.

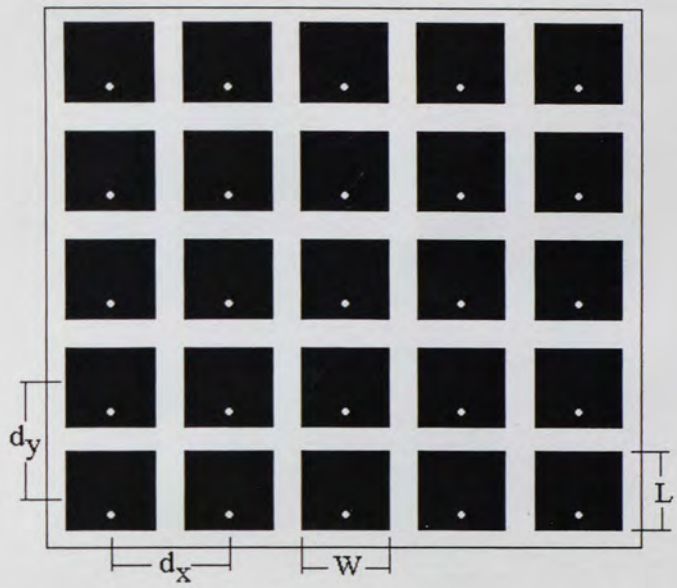

Figure 45. Top view of a twenty-five elements planar array configuration.

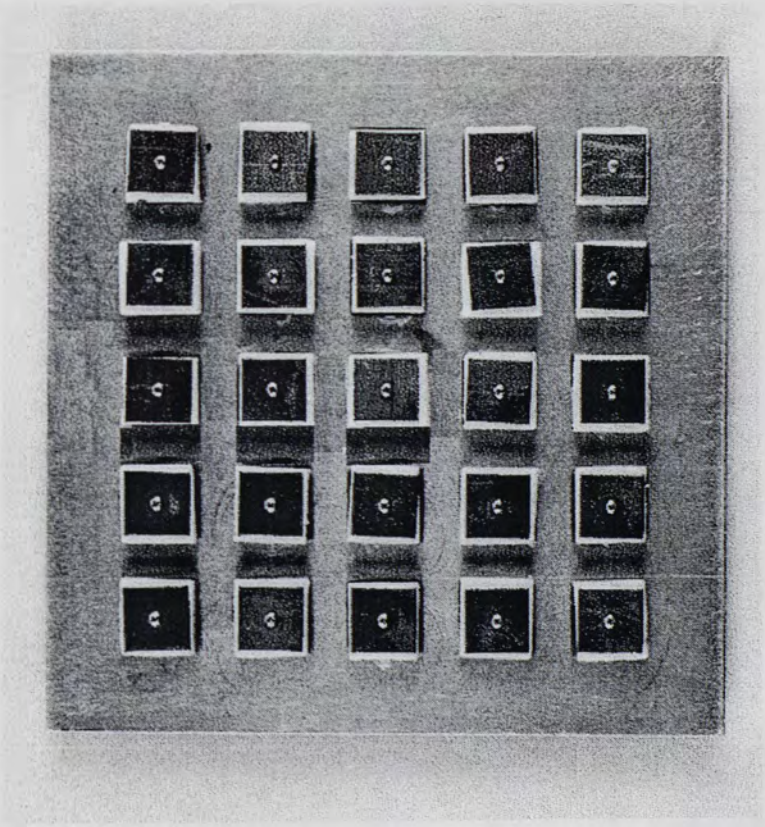

Figure 46. Photograph of the 25-elements Planar Array.

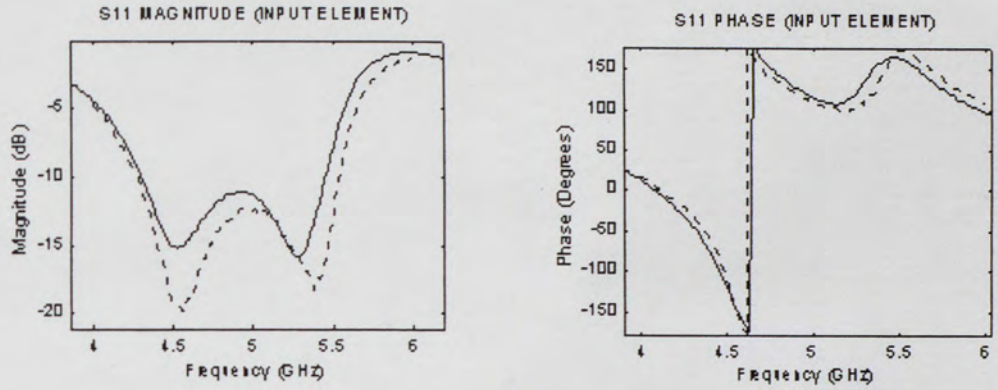

Figure 47. Planar Array Configuration: $S_{12\text{-}12}$ Analysis.

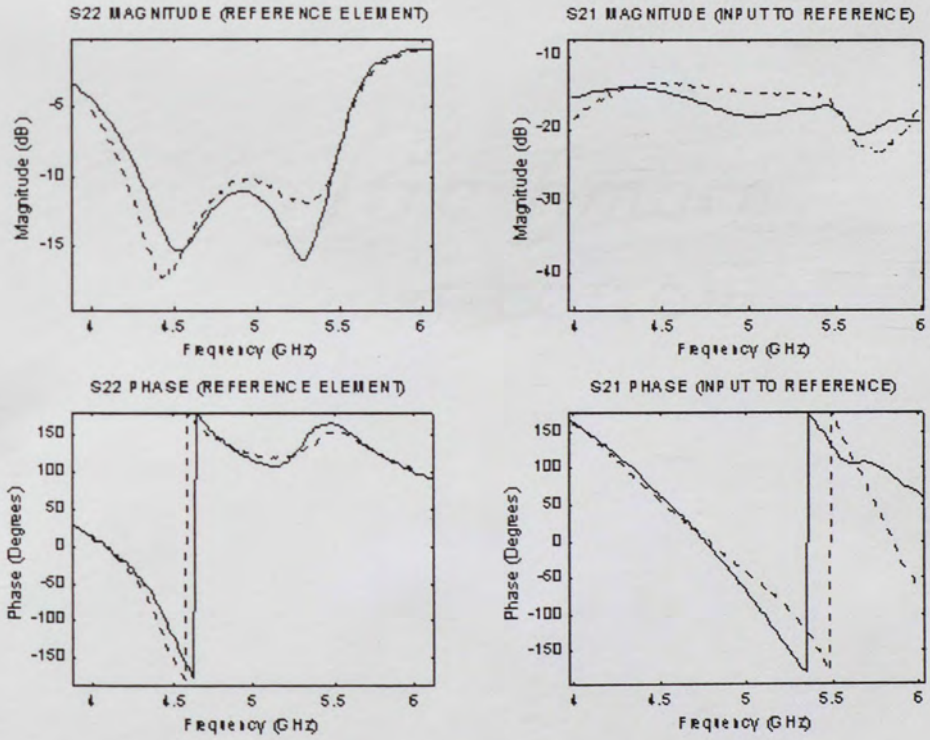

Figure 48. Planar Array configuration: $S_{13\text{-}13}$ and $S_{12\text{-}13}$ Analysis.

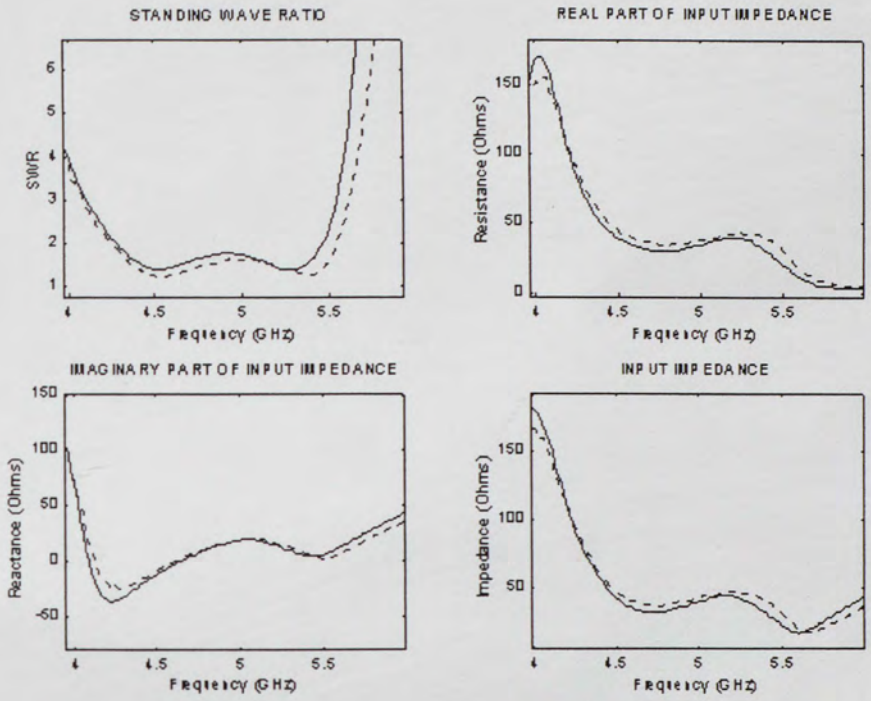

Figure 49. Planar Array Configuration: Impedance Analysis, element #12.

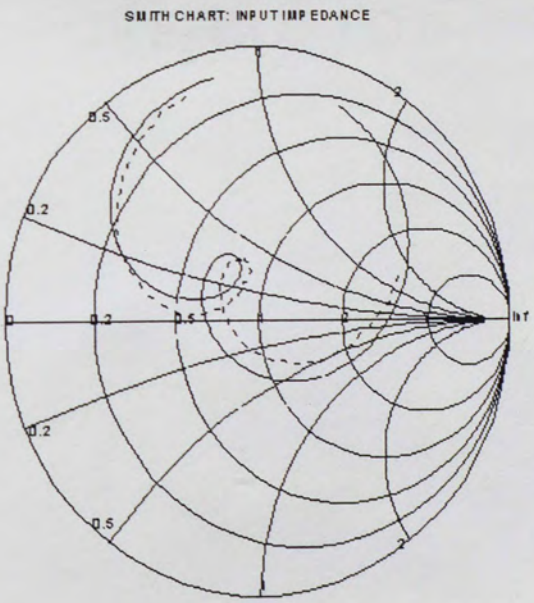

Figure 50. Planar Array configuration: Smith Chart Analysis, element #12.

7. RESULTS FOR PHASED ARRAY MICROSTRIP ANTENNAS

Large Phased Array Antennas are usually analyzed using an infinite array approximation. Even not so large arrays can be modeled reasonably as infinite. There is a very important justification for this kind of approximation: the complexity of the solution is reduced, only one element of the array is modeled and therefore the memory and computational effort is decreased. The infinite array approximation is usually done using Floquet boundary conditions around a reference element and assuming a periodic structure that is infinite in extent along the axes of the array [67-74].

An infinite array approximation includes the effect of mutual coupling between elements and predicts the variation of the scan impedance with the scan angle; however, it does not account for the edge effects that occur in a Finite Array. Furthermore, Finite Arrays excite surface waves on the dielectric substrate, which also contribute to scan blindness [75-76]; the infinite array approximation cannot provide this information, since it cannot support surface waves, except perhaps at a scan blindness angle.

The preferred method for the analysis of Phased Array Antennas has been traditionally the Method of Moments because of its ability to model rigorously the microstrip antenna geometry, and thanks to the excellent work developed by Pozar and others. The main contribution and emphasis of the work presented here is on the use of the FDTD method to analyze small arrays with stacked microstrip elements. The

flexibility and generality of the FDTD method renders it the advantage to model very complex geometrical configurations, without the need to derive a Green's Function. And also, FDTD can deliver broadband results in a single computational run. The phase-shift for each antenna element is modeled in the time-domain, feeding a Gaussian pulse to each array element but with the appropriate time delay.

7.1 Scanning Characteristics of Finite-sized Phased Array Microstrip Antennas

When an array of antennas is used for scanning, the input impedance of the array elements changes due to their interactions and mutual coupling. The scan impedance is defined as the driving-point impedance of a given array element as a function of scan angles, when all of the elements of the array are excited by the proper amplitude and phase [75-76].

Beam steering is implemented via changes in the excitation of a given element. Using the notation for an *N*-port network, the excitation for the $n-th$ element of an *N*-element array, scanning at an angle (θ_o , ϕ_o), can be expressed as

$$a_n = |a_n| e^{-jk(x_n \sin\theta_o \cos\phi_o + y_n \sin\theta_o \sin\phi_o)} \tag{81}$$

where a_n is the incident wave at port n in the *N*-port network, x_n and y_n are the coordinates of the $n-th$ element with respect to a reference element.

From the definition of the *S*-parameters,

$$S_{mn} = \left.\frac{b_m}{a_n}\right|_{a_n=0, i=1..N, i\neq n} \tag{82}$$

it can be easily shown that the active reflection coefficient for element n, the scanning angle (θ_o , ϕ_o) can be represented by the following expressions

$$\begin{aligned} \Gamma_{in}^{n}(\theta_o,\phi_o) &= \frac{b_n}{a_n} \\ \Gamma_{in}^{n}(\theta_o,\phi_o) &= \sum_{m=1}^{N} S_{nm}\frac{a_m}{a_n} \end{aligned} \tag{83}$$

The first expression for the active reflection coefficient can be easily implemented with the FDTD method, since we can feed the array element at port n with the incident wave a_n and measure the reflected wave b_n.

The second expression is very useful if the S-parameters of the array are known. The coupled energy from the other ports into port n can be calculated with FDTD using the procedure described Chapter 6, or it can be measured exciting the input element while all other elements are terminated with a matched load.

Doing the substitution of the excitation a_m into the above expression, it becomes:

$$\Gamma_{in}^{n}(\theta_o,\phi_o) = \sum_{m=1}^{N} S_{nm}\frac{|a_m|}{|a_n|} e^{-jk\sin\theta_o[(x_m-x_n)\cos\phi_o+(y_m-y_n)\sin\phi_o]} \tag{84}$$

For a uniformly excited array, the ratio of a_m to a_n is equal to 1. This expression was implemented, and proved to be very useful once the S-parameters are known.

It is a common practice to express the active reflection coefficient assuming that the array is conjugate matched to its broadside scan impedance, so

$$\Gamma_{in}^{n}(\theta_o,\phi_o) = \frac{Z_{in}^{n}(\theta_o,\phi_o) - Z_{in}^{n}(0,0)}{Z_{in}^{n}(\theta_o,\phi_o) + Z_{in}^{n}(0,0)} \tag{85}$$

where $Z_{in}^{n}(\theta_o,\phi_o)$ is the scan impedance at the scan angle (θ_o,ϕ_o) and $Z_{in}^{n}(0,0)$ is the input impedance at broadside.

Figure 51 shows the setup between the source and the $n-th$ array element. The actual input b_s at the $n-th$ port can be expressed as

$$b_s = a_n\left[1 - \Gamma_{in}^{n}(\theta,\phi)\Gamma_s^{n}(\theta,\phi)\right] \tag{86}$$

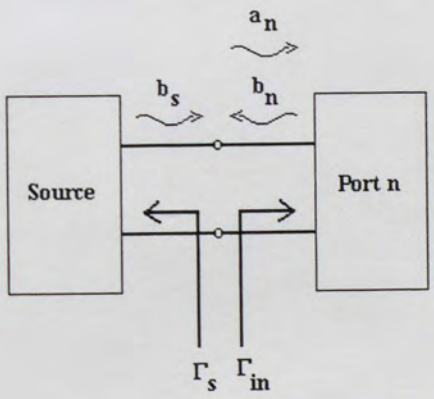

Figure 51. Two-port network setup for the excitation of the $n-th$ array element.

Therefore, the scan element pattern $E_e^n(\theta,\phi)$ for the $n-th$ element of the array can be obtained from the knowledge of the far-field radiation pattern of an isolated element $E(\theta,\phi)$ as follows

$$E_e^n(\theta,\phi) = E(\theta,\phi)\cdot b_s \cdot e^{jk\sin\theta(x_n\cos\phi + y_n\sin\phi)} \tag{87}$$

and after making the substitution for b_s yields the final expression for the scan element pattern

$$E_e^n(\theta,\phi) = E(\theta,\phi)|a_n|e^{jk[x_n(\sin\theta\cos\phi - \sin\theta_o\cos\phi_o)+y_n(\sin\theta\sin\phi-\sin\theta_o\sin\phi_o)]}\left[1-\Gamma_{in}^n(\theta,\phi)\Gamma_s^n(\theta,\phi)\right] \tag{88}$$

where $\Gamma_{in}^n(\theta,\phi)$ is the active reflection coefficient of the $n-th$ element, and $\Gamma_s^n(\theta,\phi)$ is the reflection coefficient as seen into the excitation source. Note that for conjugate matching between the source and the $n-th$ port $\left[1-\Gamma_{in}^n(\theta,\phi)\Gamma_s^n(\theta,\phi)\right]$ becomes $\left[1-\left|\Gamma_{in}^n(\theta,\phi)\right|^2\right]$. The scan element pattern can be obtained experimentally or with the FDTD model presented in chapter 6, exciting one element and terminating the others to 50 ohms.

For an array with N elements, the array radiation pattern $E_a(\theta,\phi)$ can be obtained adding the contributions of all the scan element patterns in the far field

$$E_a(\theta,\phi) = \sum_{n=1}^{N} E_e^n(\theta,\phi) \tag{88}$$

7.1.1 FDTD Treatment of the Excitations

In order to use the FDTD algorithm to analyze finite phased arrays antennas [58,59], a phase shift can be implemented in the time domain to model the effects of the scanning angle. The sources that excite each one of the array elements can be modeled using the shift property of the Fourier Transform, i.e. [53-57]:

$$e^{-j\Delta\phi_o} F(\omega) \leftrightarrow f(t - t_d) \tag{89}$$

where $\Delta\phi_o$ is the excitation phase difference between the $n-th$ array element and a reference element and t_d is the time delay in the excitation of both elements, i.e.:

$$\Delta\phi_o = \omega t_d = \phi_n - \phi_{ref} \tag{90}$$

By inspection of the above expression it is observed that a fixed delay in the time domain will yield a frequency-dependent phase shift. Does this mean that this is not a viable procedure? Without loss of generality, let's do an exercise with a uniformly excited array with spacing d among the array elements.

Switched-line shifters (also referred to as time-delay steering) have the desirable property that beam position is independent of the frequency driving the phase shifter. The phase shift $\Delta\phi_o$ required to scan to an angle θ_o from bore-sight is given by

$$\Delta\phi_o = kd\,sin\theta_o \tag{91}$$

Note that since $k = 2\pi f / c$, if there is a frequency change the phase and steering angle direction will change. If a delay line with length L is used as a phasing network, the phase shift is equal to $\Delta\phi_o = kL$. If this expression is combined with the above equation, it can be shown that the steering direction can be made independent of frequency

$$sin\theta_o = \frac{L}{d} \tag{92}$$

Using the idea presented above, introducing a phase shift $\Delta\phi_o = \omega t_d$ and combining it with the equation for the phase shift $\Delta\phi_o$ required to scan to an angle θ_o from bore-sight yields,

$$sin\theta_o = \frac{ct_d}{d} \tag{93}$$

Therefore, it can be concluded that the introduction of a constant time delay is equivalent to the introduction of a line of length $L = ct_d$ at the excitation point. And that renders this approach viable for the modeling of the excitation and broadband analysis of phased array antennas.

7.2 Implementation of the Excitation in Time Domain

The excitation phase-difference $\Delta\phi_o = \phi_n - \phi_{ref}$ between element n and the reference element in the array can be determined in terms of a constant $\Delta\phi_{min}$. For simplicity, the time delay is chosen to be proportional to the time step used in the FDTD calculations, i.e., $t_d = m\Delta t$. Thus [53-57],

$$\begin{aligned} \Delta\phi_o &= m\Delta\phi_{min} = \varpi \cdot t_d = 2\pi f \cdot m\Delta t \\ \Delta\phi_{min} &= 2\pi f \Delta t \end{aligned} \tag{94}$$

If β_x and β_y are the progressive phase shift, d_x and d_y the distance between the array elements in the x and y directions respectively, the maximum of the array factor occurs when:

$$\begin{aligned} \beta_x &= -kd_x \sin\theta_o \cos\phi_o \\ \beta_y &= -kd_y \sin\theta_o \sin\phi_o \end{aligned} \tag{95}$$

Hence, using the idea presented previously, the progressive phase shift β_x is m times $\Delta\phi_{min}$ in the x-direction and β_y is n times $\Delta\phi_{min}$ in the y-direction:

$$\begin{aligned} \beta_x &= m\Delta\phi_{min} \\ \beta_y &= n\Delta\phi_{min} \end{aligned} \tag{96}$$

Thus, delaying the phase excitation by m time steps ($m \cdot \Delta t$) in the x-direction and n time steps ($n \cdot \Delta t$) in the y-direction renders a time domain approach for modeling a phased array antenna.

In the frequency domain, the phase excitation for the (i, j) array element in a planar array takes the form ($i = 1..M$, $j = 1..N$):

$$\begin{aligned} \Delta\phi &= \phi_o + (i-1)\beta_x + (j-1)\beta_y \\ \Delta\phi &= \phi_o + (i-1)m\Delta\phi_{min} + (j-1)n\Delta\phi_{min} \end{aligned} \tag{97}$$

where ϕ_o is the phase of the reference element of the array (usually $\phi_o = 0$).

In order to avoid modeling time advances, only time delays are represented with this approach; therefore, the reference element must always be element #1 $(i = 1, j = 1)$. In the time domain, the equivalent Gaussian pulse excitation becomes:

$$E(t) = e^{-\left[\frac{t - t_o - (i-1)m\Delta t - (j-1)n\Delta t}{t_c}\right]^2} \tag{98}$$

The excitation of every array element occurs at delayed times with respect to the reference element. This idea is depicted in Figure 52.

$$t = t_o + (i-1)m\Delta t + (j-1)n\Delta t \tag{99}$$

Some caution must be exercised in order to represent adequately this time delay and to avoid undesired numerical reflections coming from the coaxial lines. The feed model requires terminating the coaxial lines with an absorbing boundary condition at their excitation planes. The ABCs must start once the Gaussian pulse (width $2t_o$) has already traveled through the excitation plane. For example, for element #1 the ABC must start at $t = 2t_o$, for element #2 at $t = 2t_o + m\Delta t$, and in general, for the element located at row M, column N, at $t = 2t_o + (M-1)m\Delta t + (N-1)n\Delta t$.

The number of time steps that the excitation must be delayed in order to represent the desired progressive phase shift is, in the x and y directions,

$$\begin{aligned} m &= \frac{d_x \sin\theta_o \cos\phi_o}{c_x \Delta t} \\ n &= \frac{d_y \sin\theta_o \sin\phi_o}{c_y \Delta t} \end{aligned} \tag{100}$$

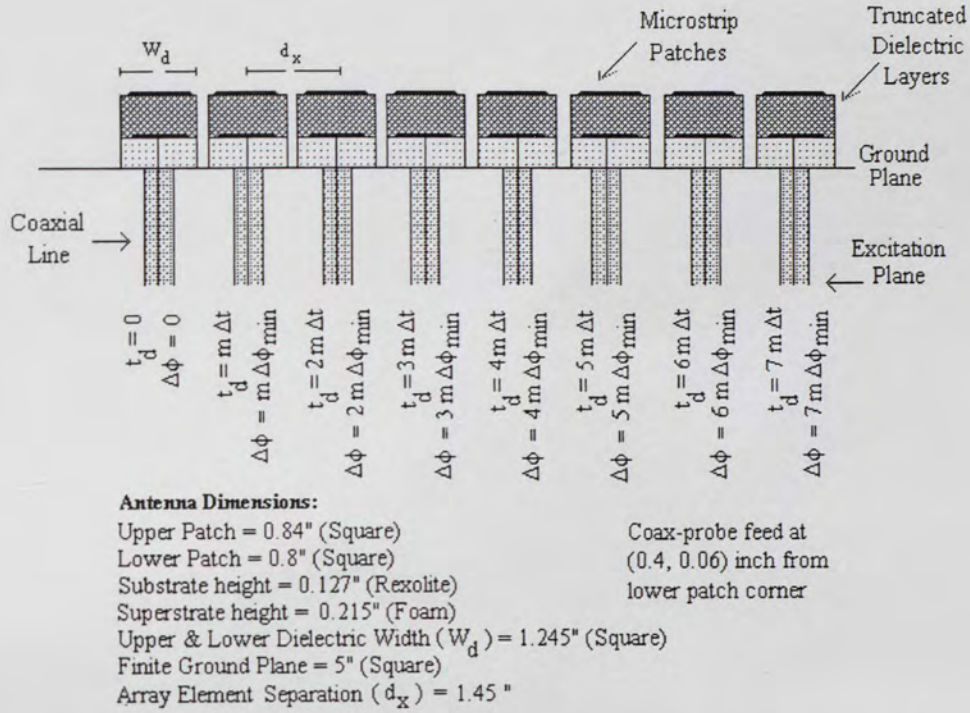

Figure 52. Time Domain excitation of the Phased Array. PML parameters: $N = 9$, $g = 4.0$, $R(0) = 10^{-4}$. Antenna & Coax-Line Mesh Size: $\Delta x = \Delta y = 1.016\ mm$, $\Delta z = 0.80645\ mm$. Number of grids: Antenna *306 x 54 x 30*, Coax-Line *7 x 7 x 70*.

7.3 Simulation Results

The active reflection coefficient was calculated for two linear arrays, E-Plane and H-Plane configuration [53-57]. For these calculations, a nine-layer PML was used, with the geometrical progression coefficient $g = 4.0$ and a reflection coefficient at normal incidence $R(0) = 10^{-4}$. The computational grid size was $\Delta x = \Delta y = 1.016\ mm$, $\Delta z = 0.80645\ mm$.

Figures 53 through 56 depict the active impedance and S_{11} calculations for element number 4 of the broadside linear arrays, H-plane and E-plane configuration ($\beta_x = \beta_y = 0$). Two different scanning angles (30 and 90 degrees) were calculated for the H-plane configuration. For these angles, $\beta_x = 104.9655$ *degrees* ($m = 34.6753$, $\Delta\phi_{min} = 3.0271$ *degrees*, $\Delta t = 1.7702$ *psec*), and $\beta_x = 209.935$ *degrees* ($m = 69.3519$, $\Delta\phi_{min} = 3.0271$ *degrees*, $\Delta t = 1.7702$ *psec*). The results are shown in Figures 57 through 61.

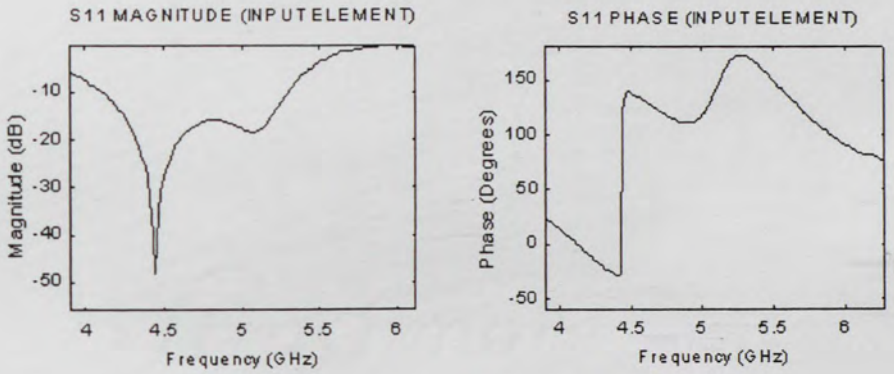

Figure 53. Magnitude and Phase of S_{11} at element 4 of the active H-Plane array configuration ($\beta_x = 0$ *degrees*).

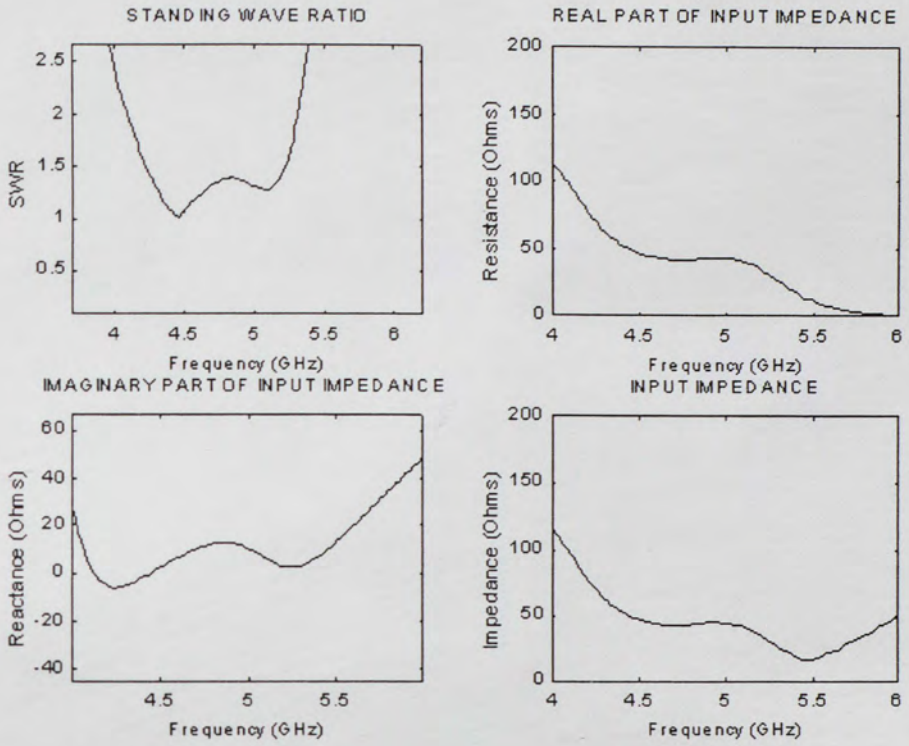

Figure 54. Input impedance and VSWR at element 4 of the active H-Plane array configuration (β_x = *0 degrees*).

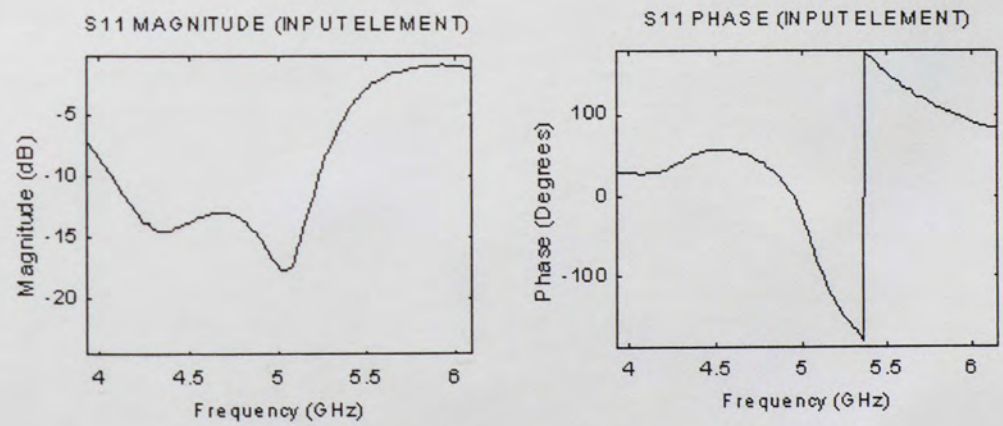

Figure 55. Magnitude and Phase of S_{11} at element 4 of the active E-Plane array configuration (β_y = *0 degrees*).

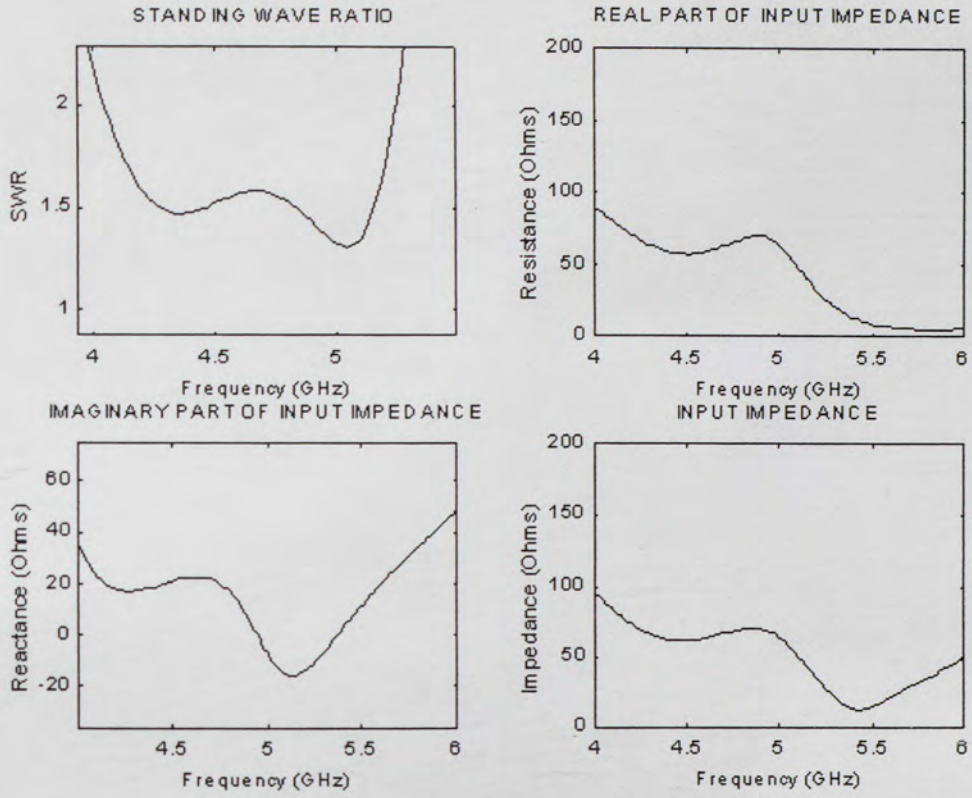

Figure 56. Input impedance and VSWR at element 4 of the active E-Plane array configuration (β_y = *0 degrees*).

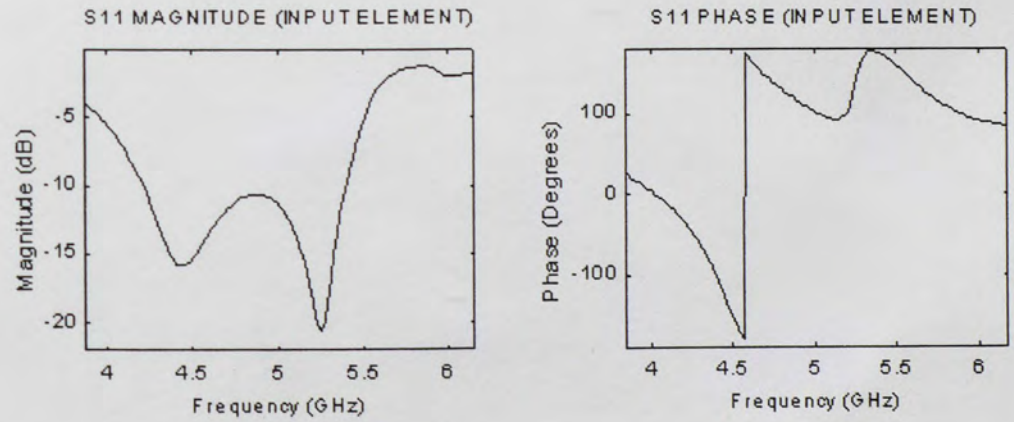

Figure 57. Magnitude and Phase of S_{11} at element 4 of the active H-Plane array configuration (β_x = *104.9655 degrees*, isotropic scan angle = *30 degrees*).

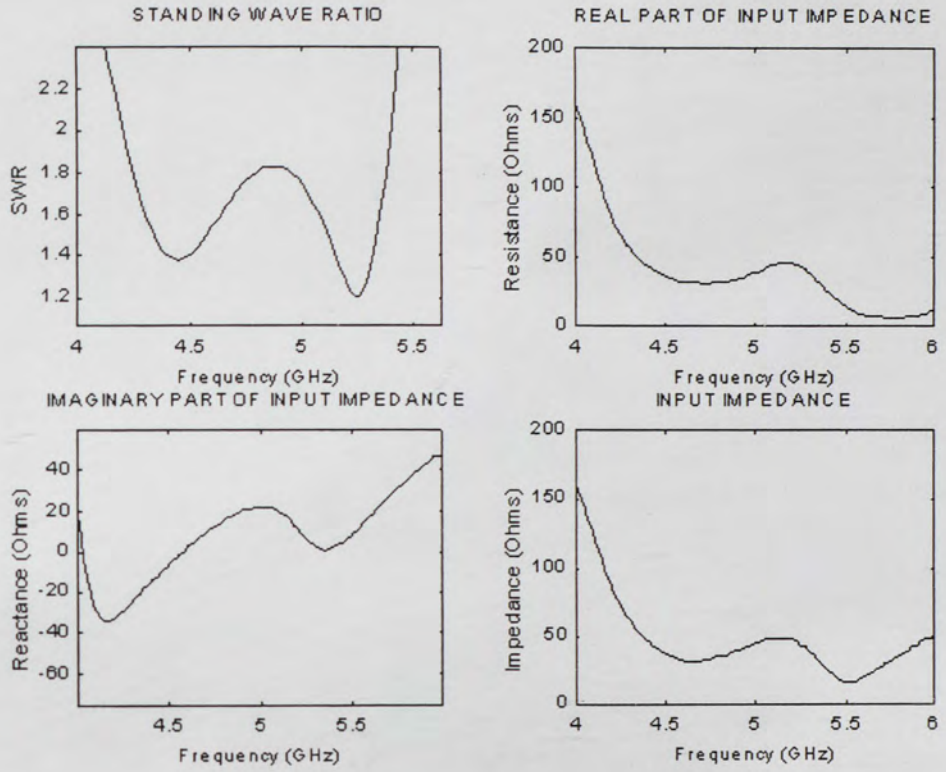

Figure 58. Input impedance and VSWR at element 4 of the active H-Plane array configuration (β_x = *104.9655 degrees*, isotropic scan angle = *30 degrees*).

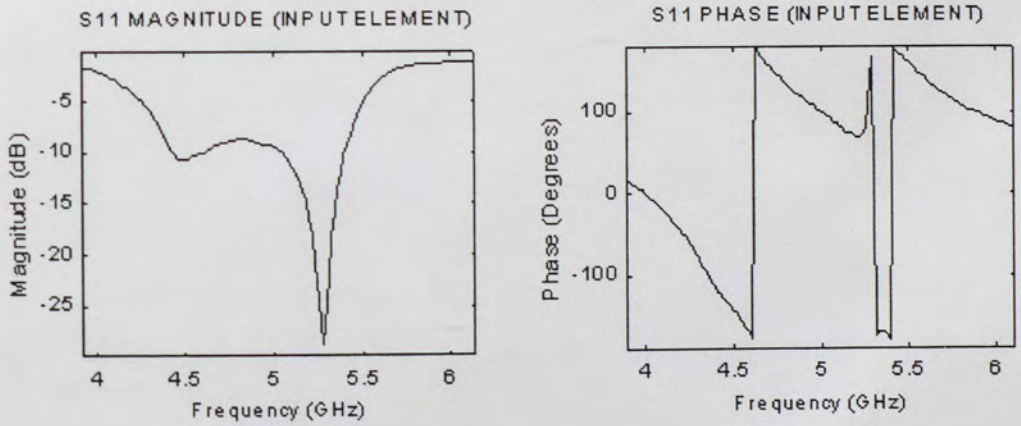

Figure 59. Magnitude and Phase of S_{11} at element 4 of the active H-Plane array configuration (β_x = *209.935 degrees*, isotropic scan angle = *90 degrees*).

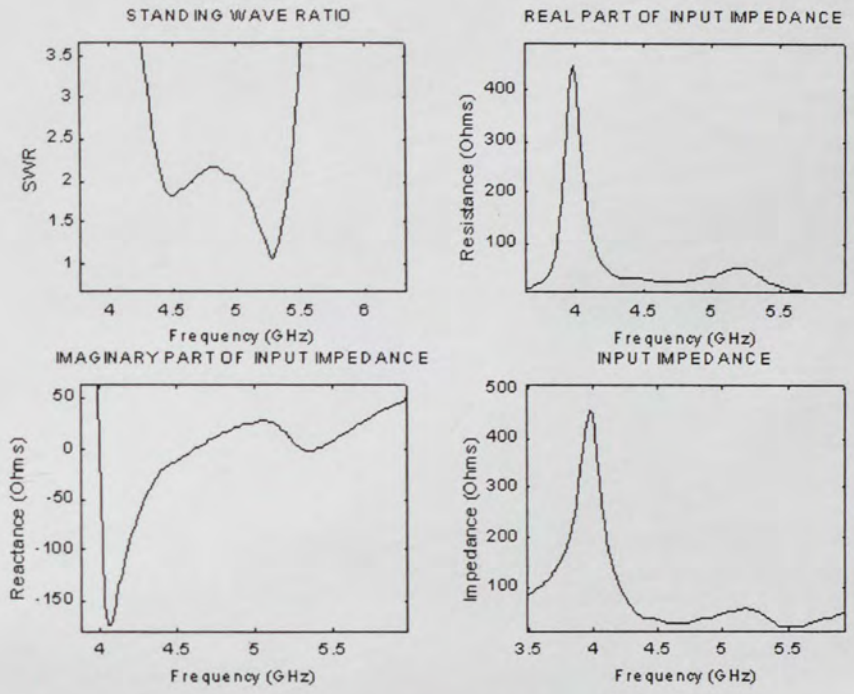

Figure 60. Input impedance and VSWR at element 4 of the active H-Plane array configuration (β_x = *209.935 degrees*, isotropic scan angle = *90 degrees*).

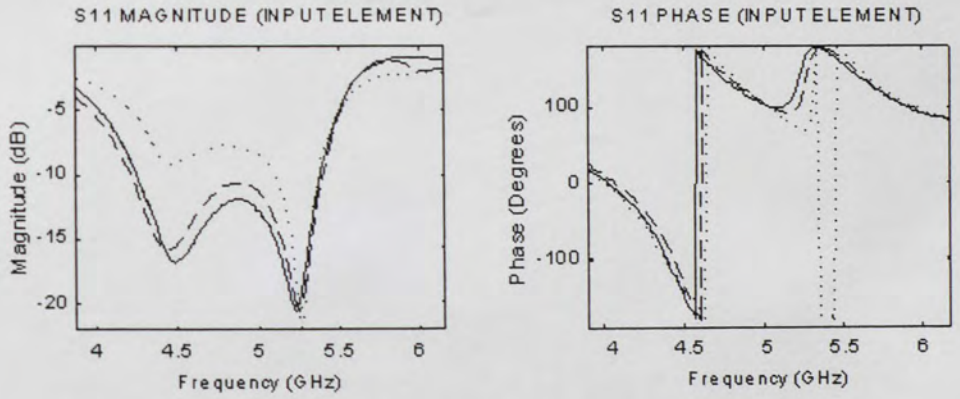

Figure 61. Magnitude and Phase of S11 at element 4 of the H-Plane array configuration (center frequency, 4.75 GHz)

____ β_x = *0, m = 0, scan angle = 0 degrees*

- - - - β_x = *104.9655 degrees, m = 34.6753, scan angle = 30 degrees*

. . . . . β_x = *209.935 degrees, m = 69.3519, scan angle = 90 degrees*

7.3.1 Isolated Microstrip Antenna

The radiation characteristics of the isolated microstrip element are presented in Figures 62 through 69. These results will be appreciated better when they are compared to the case when the antenna is put in an array environment.

The radiation parameters can be calculated from the electric fields predicted using the near to far zone transformation:

The circular polarization loss is: -3.0103 dB

The radiation pattern has a maximum at phi = 0 degrees, theta = 0 degrees

The mismatch loss is equal to: -0.414759 dB

The input power at the antenna port is equal to: 0.00908917 Watts

The total radiated power is equal to: 0.00474736 Watts

The average radiated power per steradian is equal to: 0.000377783 Watts/steradian

The directivity is equal to: 8.46723 dB

The radiation efficiency is equal to: 52.231 percent or -2.82072 dB

The gain is equal to : 5.23175 dB or 3.13175 dbi

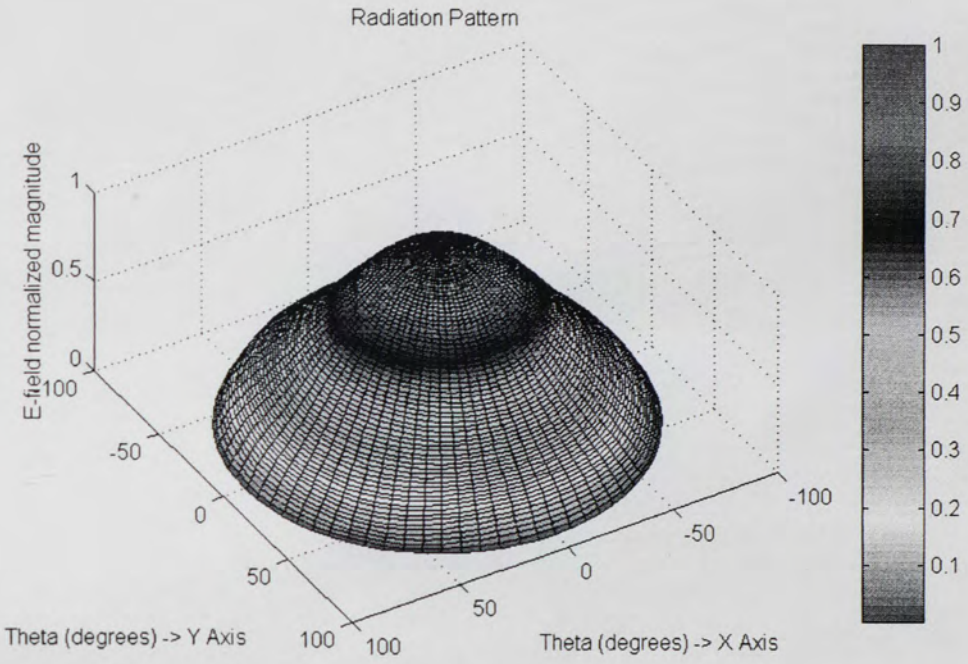

Figure 62. 3-D Mapped Pattern of the Isolated Microstrip Element at 4.75 GHz.

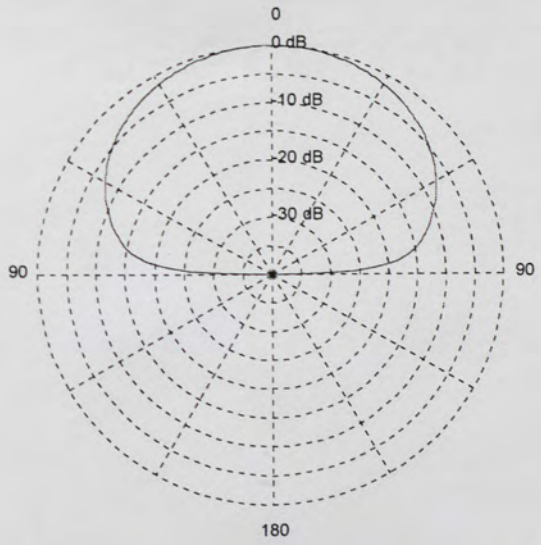

Figure 63. E-Plane Radiation Pattern of the isolated microstrip element, phi-cut = 0 degrees at 4.75 GHz.

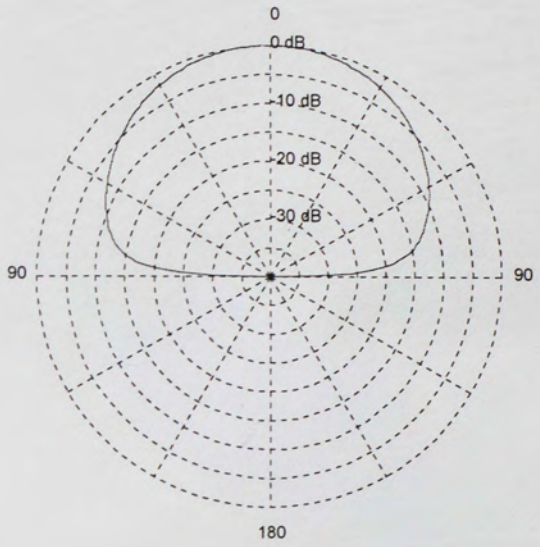

Figure 64. H-Plane Radiation Pattern of the isolated microstrip element, phi-cut = 90 degrees at 4.75 GHz.

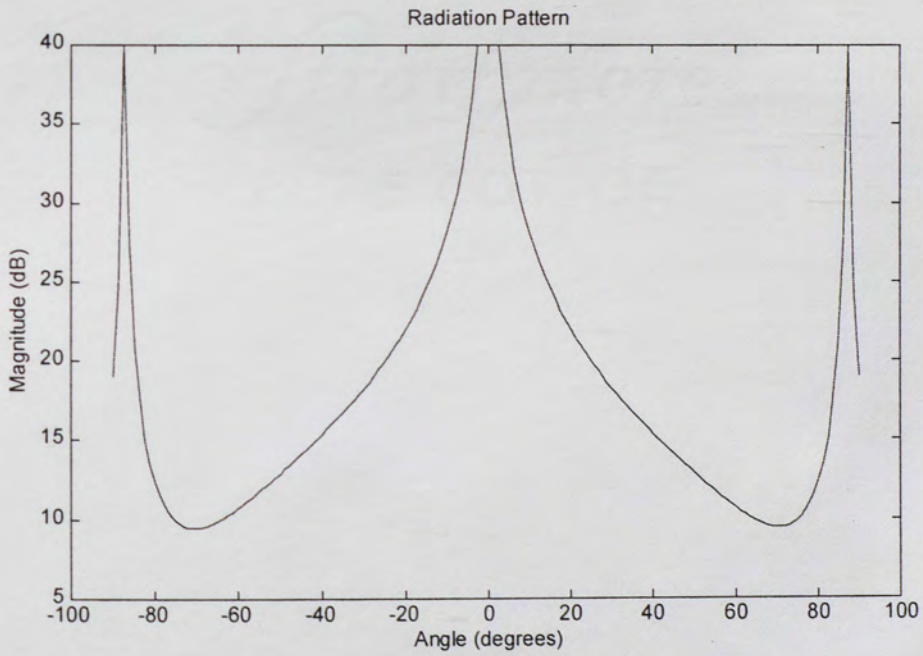

Figure 65. Axial Ratio for the isolated microstrip element, phi-cut = 0 degrees at 4.75 GHz.

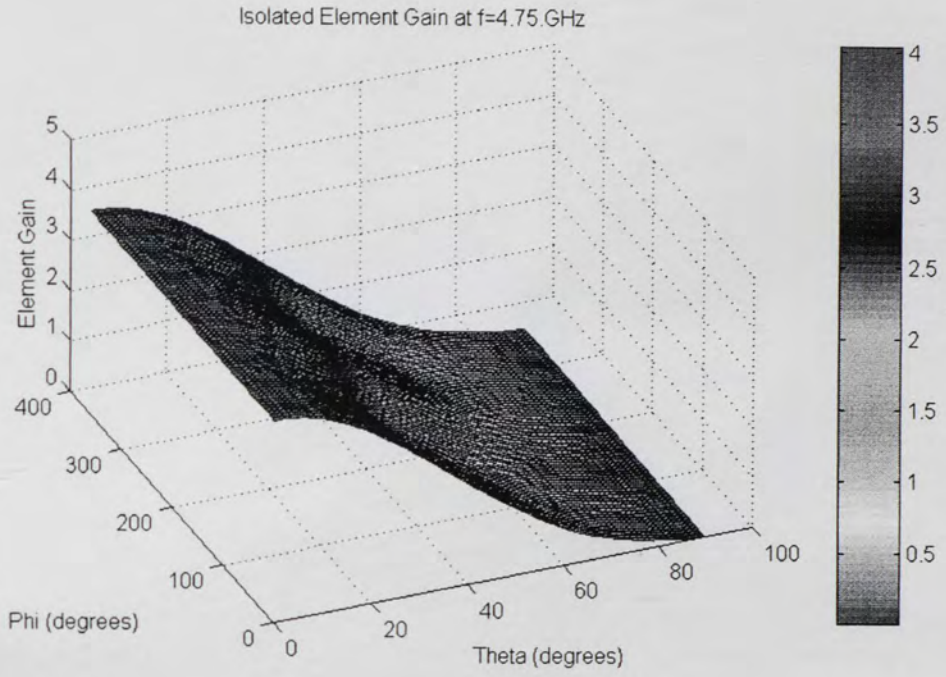

Figure 66. Gain of the isolated microstrip element at 4.75 GHz.

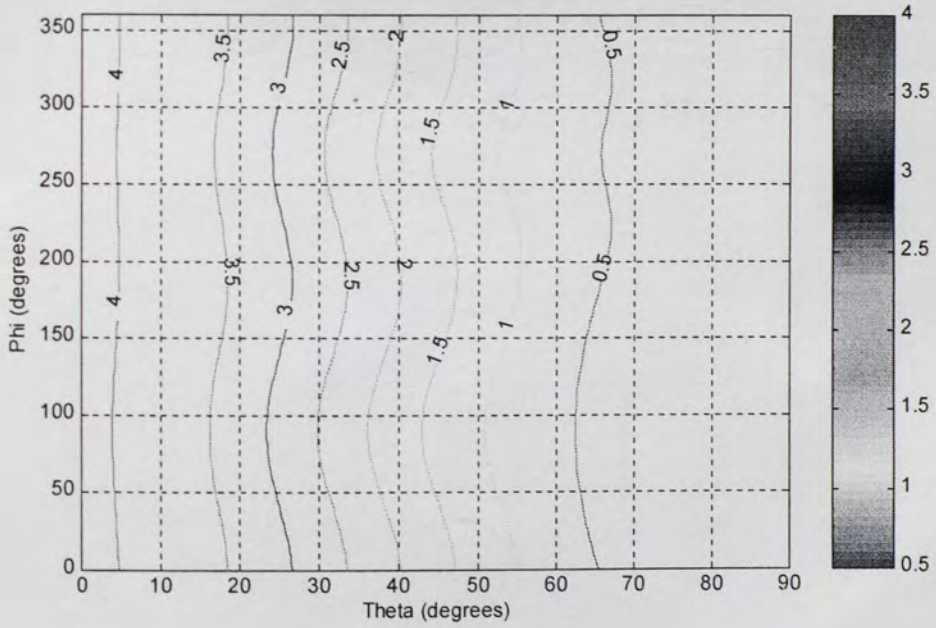

Figure 67. Contour Plot of the gain for the isolated microstrip element at 4.75 GHz.

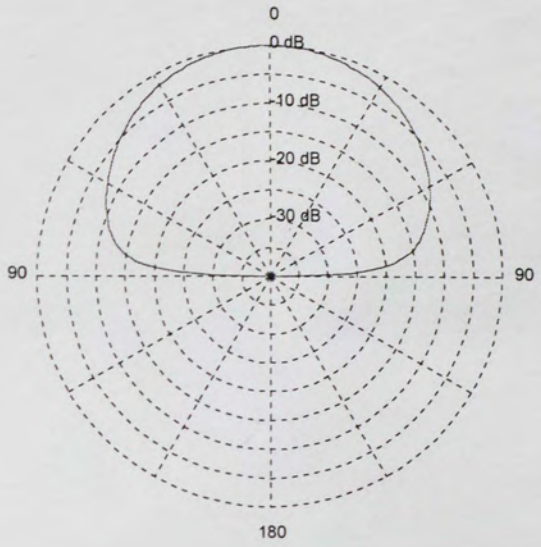

Figure 68. E-Plane Co-polarized Pattern for the isolated microstrip element, phi-cut = 0, Ey at 4.75 GHz.

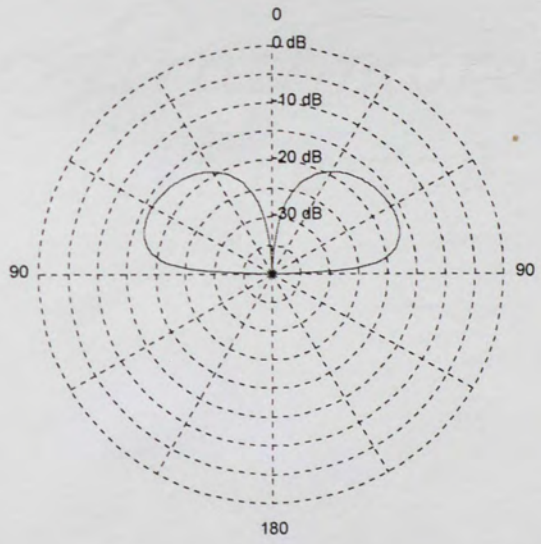

Figure 69. E-Plane cross-polarization pattern for the isolated microstrip element, phi-cut = 0, Ex at 4.75 GHz.

7.3.2 E-Plane Array Scan Element Patterns

The scan element pattern characteristics for the eight-element E-Plane Array are presented in Figures 70 through 80. Although in these results only one element is being fed while the other elements are terminated in 50 ohms, several conclusions can be extrapolated that will determine the performance of the scanning-array once all the elements are active.

The radiation parameters can be calculated from the electric fields predicted using the near to far zone transformation. These results can be compared to those for the isolated element.

The circular polarization loss is: -3.0103 dB

The radiation pattern has a maximum at phi = 0 degrees, theta = 0 degrees

The mismatch loss is equal to: -0.414759 dB

The input power at the antenna port is equal to: 0.00908917 Watts

The total radiated power is equal to: 0.00386622 Watts

The average radiated power per steradian is equal to: 0.000307664 Watts/steradian

The directivity is equal to: 9.10666 dB

The gain is equal to: 4.97953 dB or 2.87953 dbi

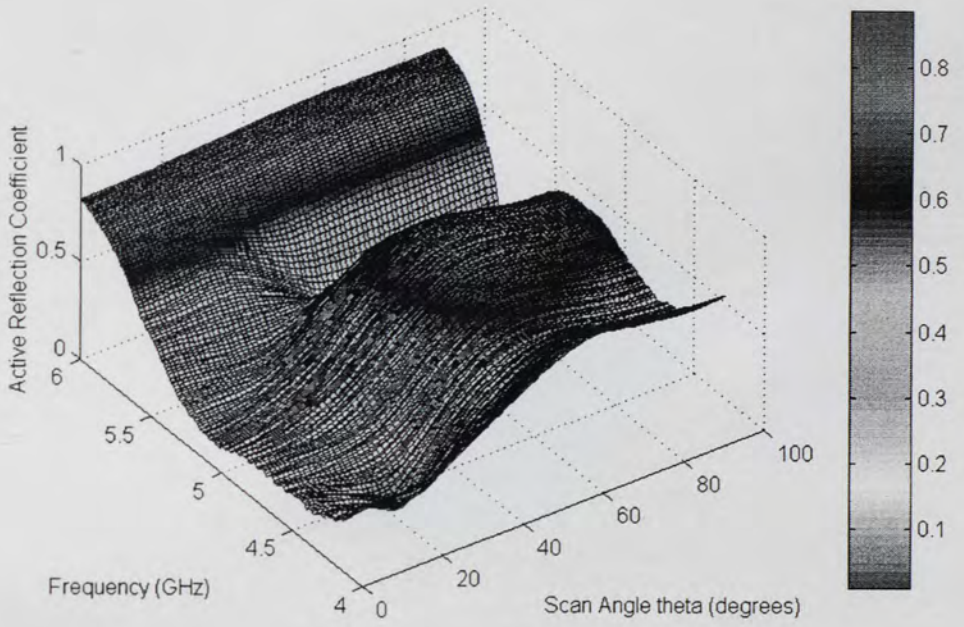

Figure 70. Active Reflection-Coefficient for the eight-element E-Plane Array.

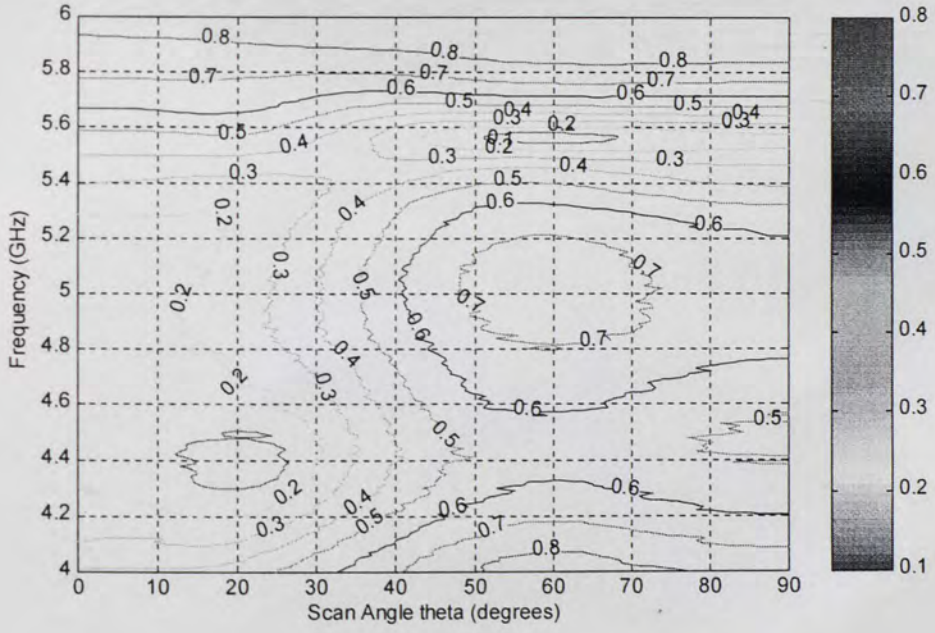

Figure 71. Contour Plot of the Active Reflection-Coefficient for the 8-element E-Plane Array.

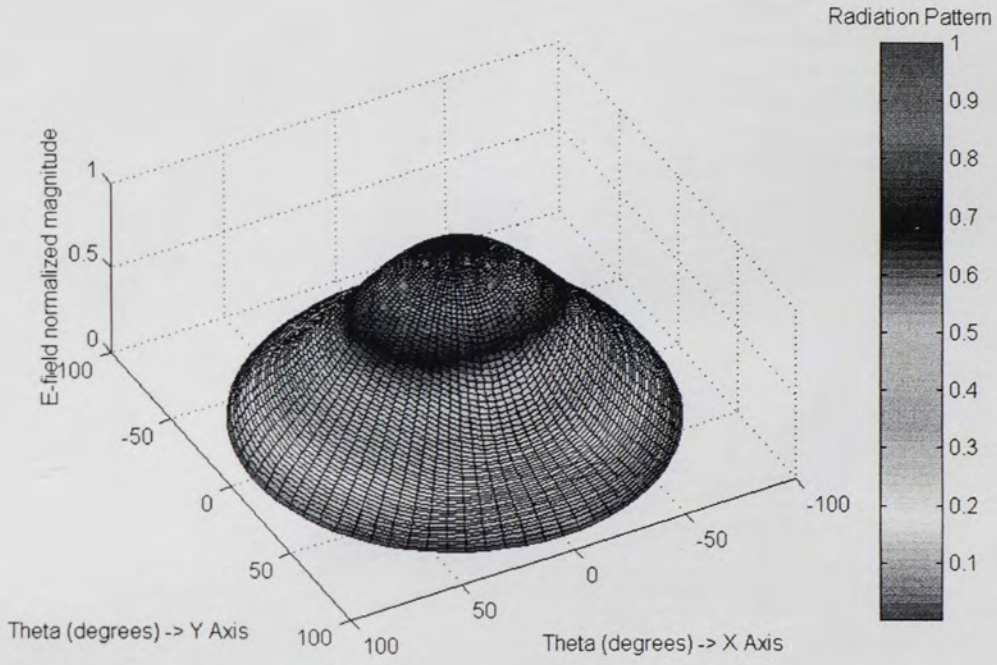

Figure 72. 3-D Mapped Scan Element Pattern for the E-Plane Array at 4.75 GHz.

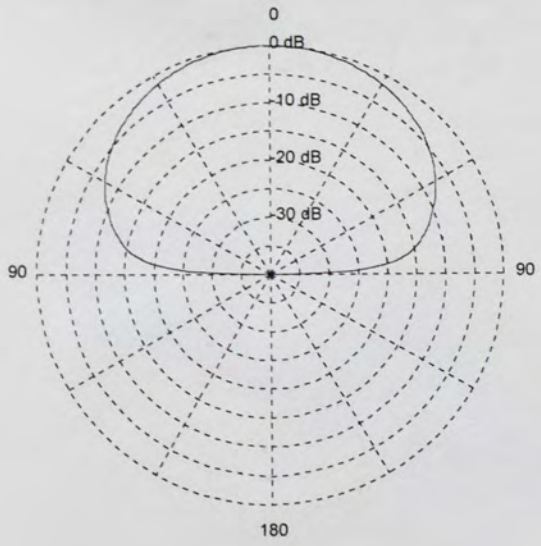

Figure 73. Scan element pattern for the E-Plane Array, phi-cut = 0 degrees at 4.75 GHz.

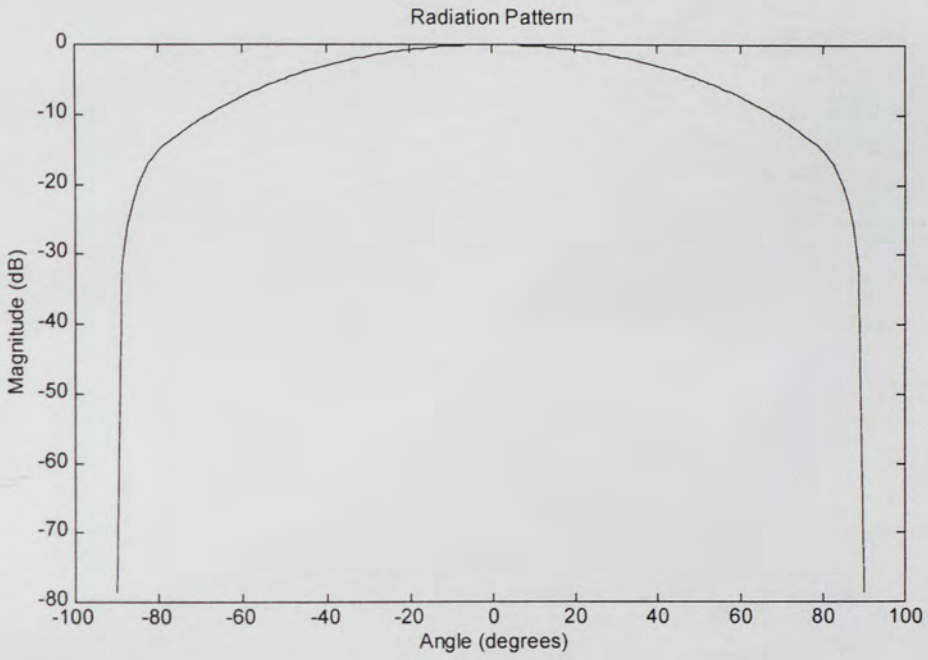

Figure 74. Scan element pattern for the E-Plane Array, phi-cut = 0 degrees at 4.75 GHz.

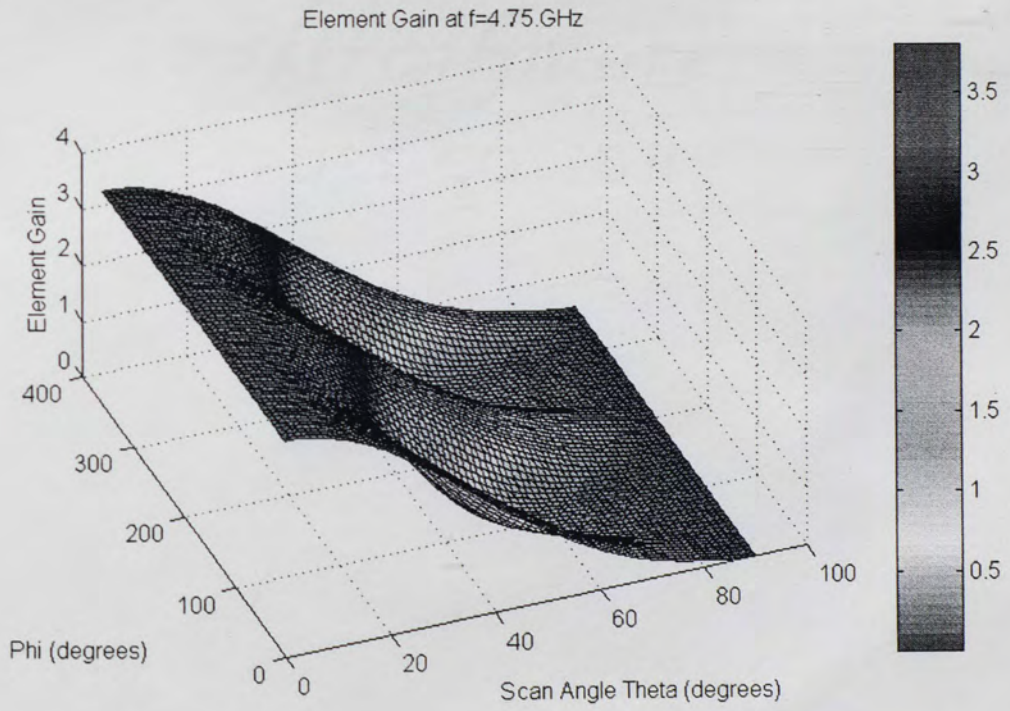

Figure 75. Gain of the Scan Element for the E-Plane Array at 4.75 GHz.

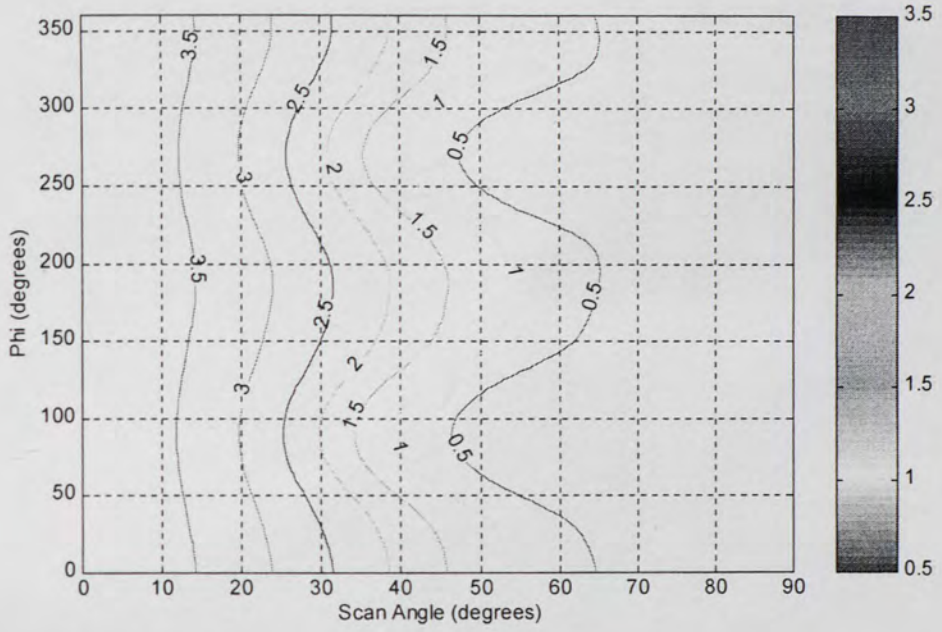

Figure 76. Gain of the Scan Element for the E-Plane Array at 4.75 GHz.

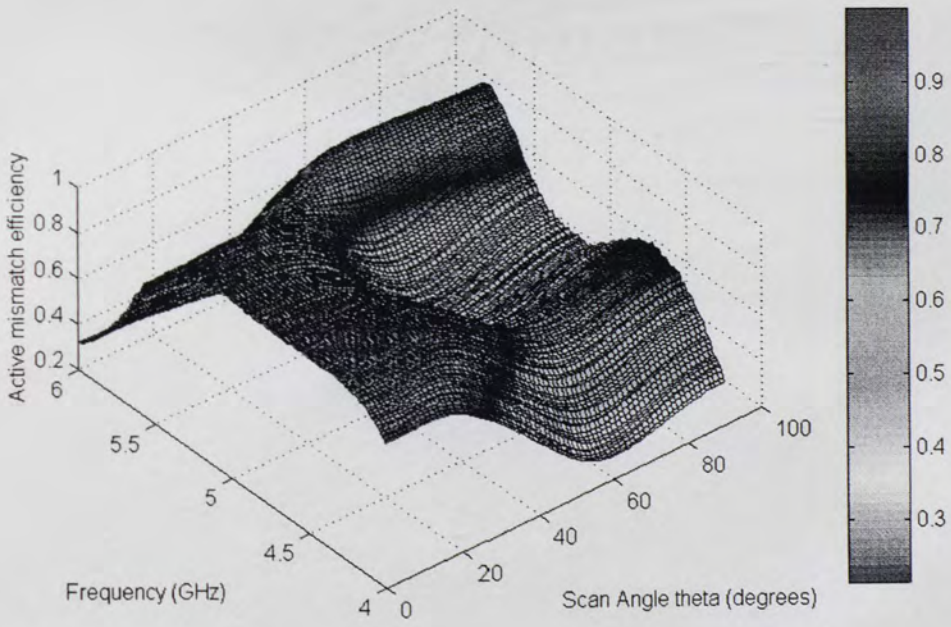

Figure 77. Efficiency of the Scan Element for the E-Plane Array.

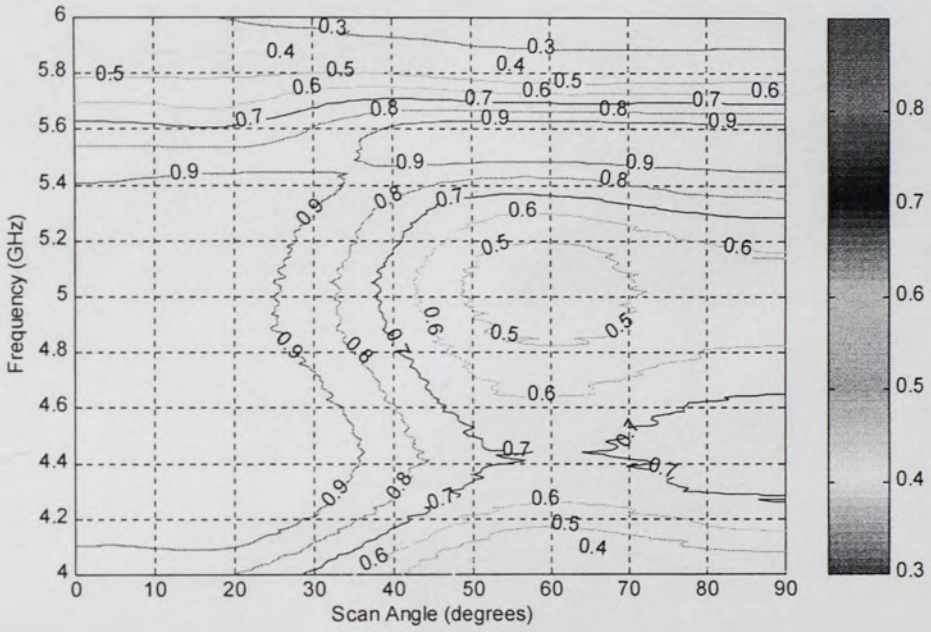

Figure 78. Contour Plot of the Efficiency of the Scan Element for the E-Plane Array.

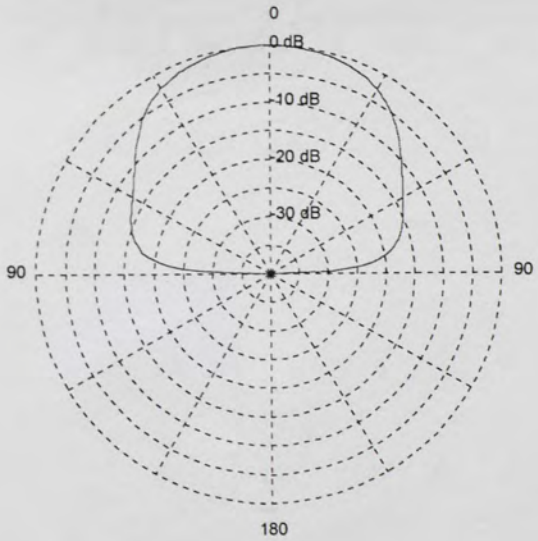

Figure 79. E-Plane Pattern for the E-Plane Array, phi-cut = 90 degrees, at 4.75 GHz.

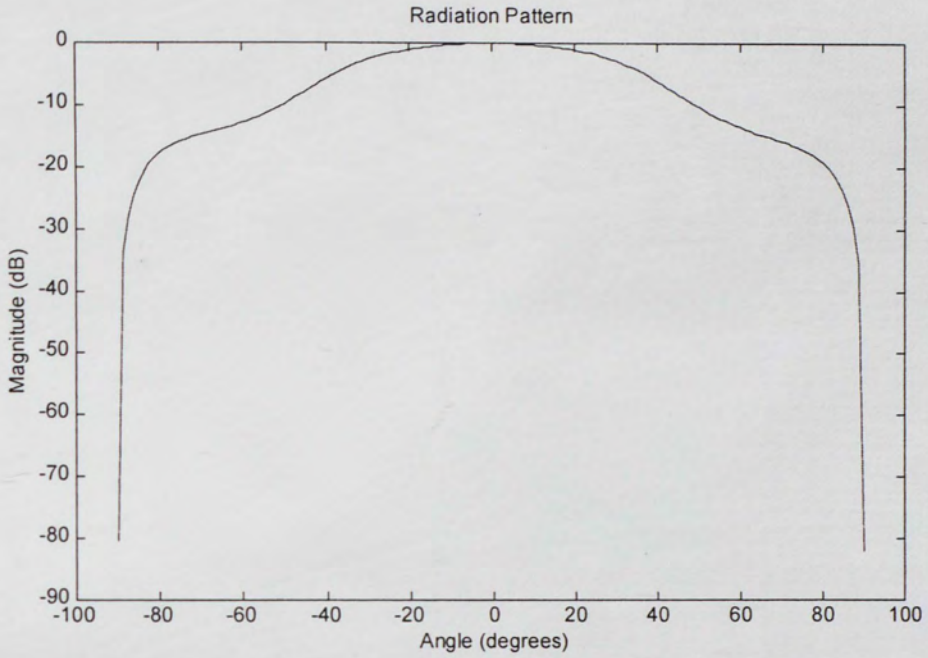

Figure 80. E-Plane Pattern for the E-Plane Array, phi-cut = 90 degrees, at 4.75 GHz.

7.3.3 H-Plane Array Scan Element Patterns

The scan element pattern characteristics for the eight-element H-Plane Array are presented in Figures 81 through 91. Although in these results only one element is being fed while the other elements are terminated in 50 ohms, several conclusions can be extrapolated that will determine the performance of the scanning-array once all the elements are active.

The radiation parameters can be calculated from the electric fields predicted using the near to far zone transformation. These results can be compared to those for the isolated element.

The radiation pattern has a maximum at phi = 0 degrees, theta = 0 degrees

The mismatch loss is equal to: -0.270424 dB

The input power at the antenna port is equal to: 0.00939632 Watts

The total radiated power is equal to: 0.00421081 Watts

The average radiated power per steradian is equal to: 0.000335085 Watts/steradian

The directivity is equal to: 8.80382 dB

The gain is equal to: 5.04748 dB or 2.94748 dbi

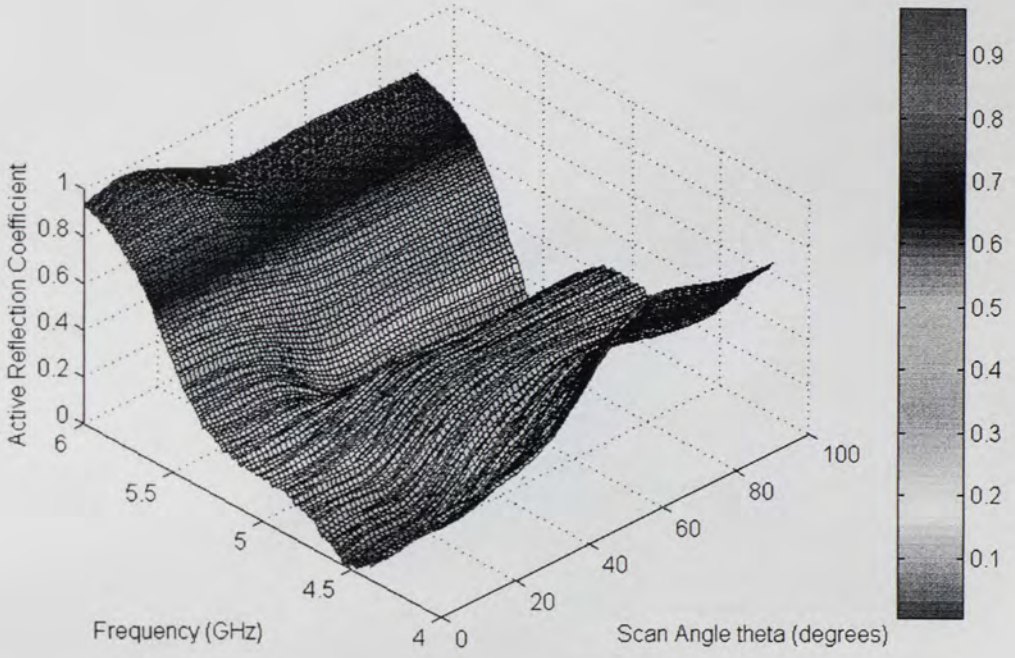

Figure 81. Active Reflection Coefficient for the H-Plane Array.

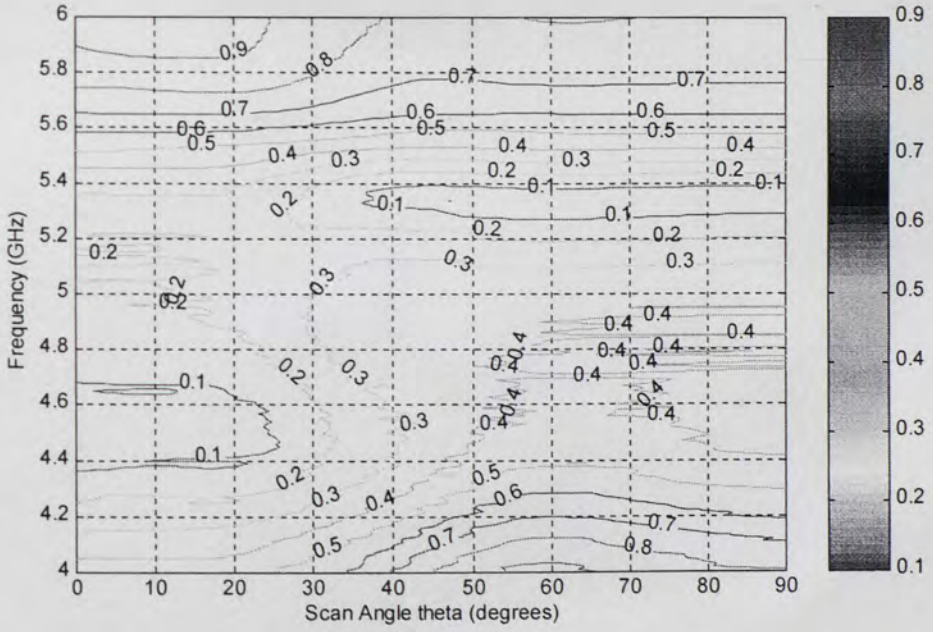

Figure 82. Contour Plot of the Active Reflection Coefficient for the H-Plane Array.

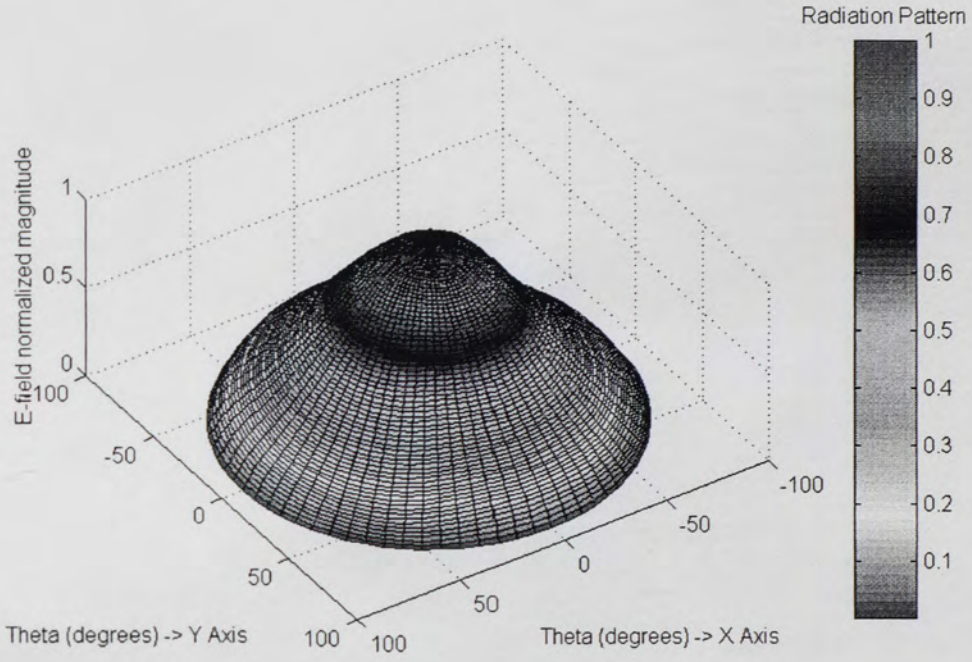

Figure 83. 3-D Mapped Scan Element Pattern for the H-Plane Array at 4.75 GHz.

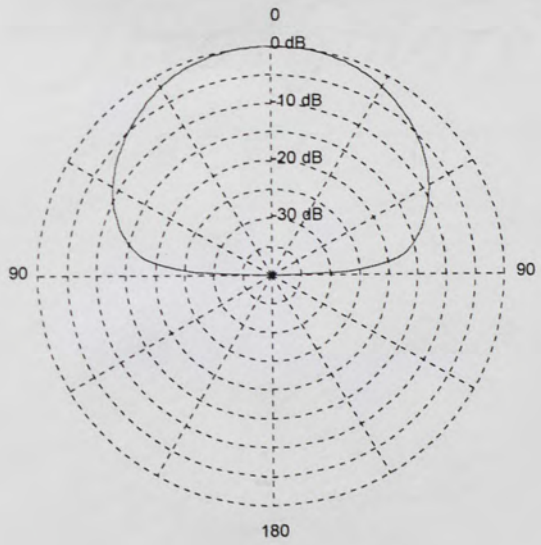

Figure 84. H-Plane Scan Element Pattern, H-Plane Array, phi-cut = 0 degrees, 4.75 GHz.

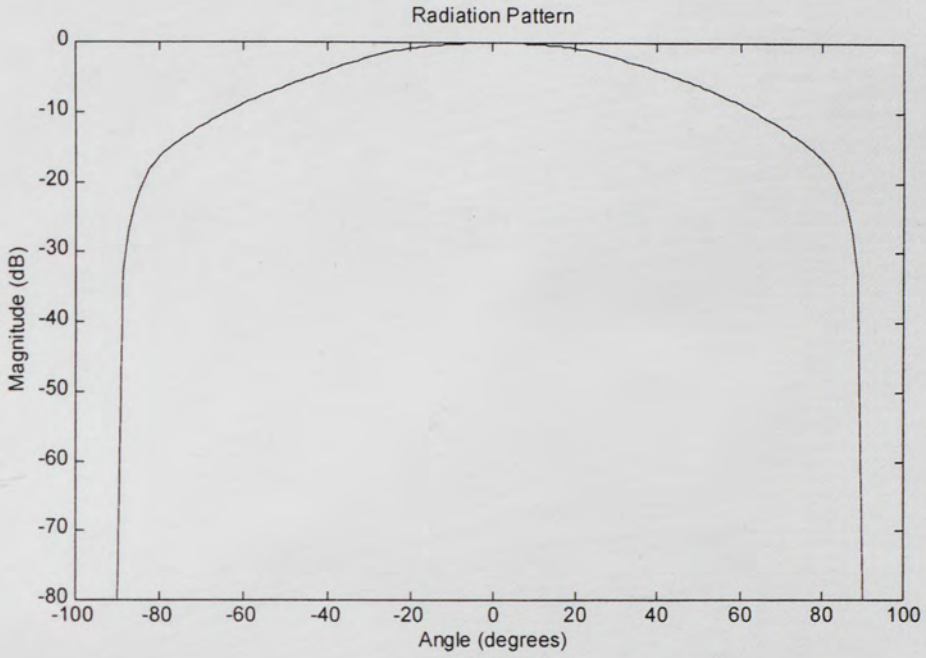

Figure 85. H-Plane Scan Element Pattern, H-Plane Array, phi-cut = 0 degrees, 4.75 GHz.

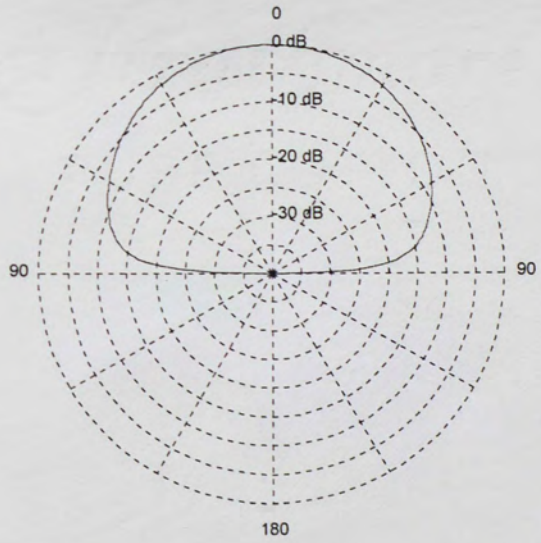

Figure 86. E-Plane Scan Element Pattern, H-Plane Array, phi-cut = 90, 4.75 GHz.

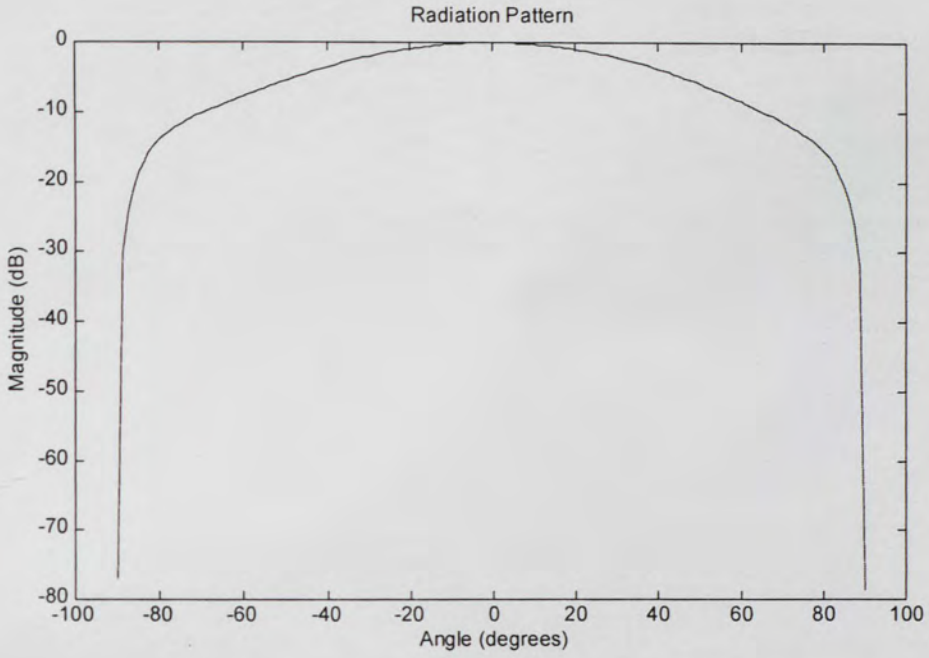

Figure 87. E-Plane Scan Element Pattern, H-Plane Array, phi-cut = 90, 4.75 GHz.

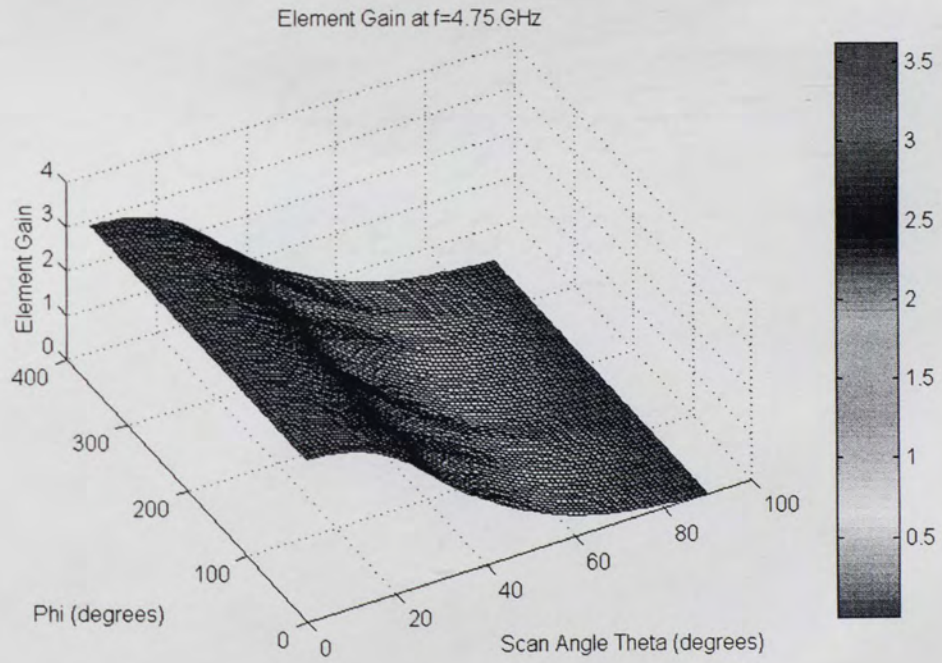

Figure 88. Gain for the Scan Element in H-Plane Array at 4.75 GHz.

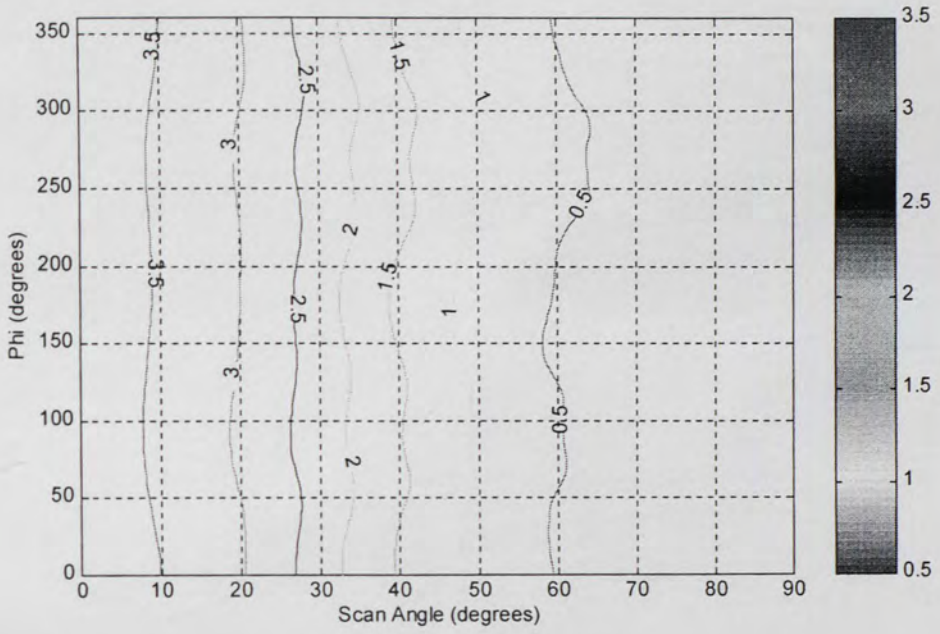

Figure 89. Contour Plot of the Gain for the Scan Element, H-Plane Array, 4.75 GHz.

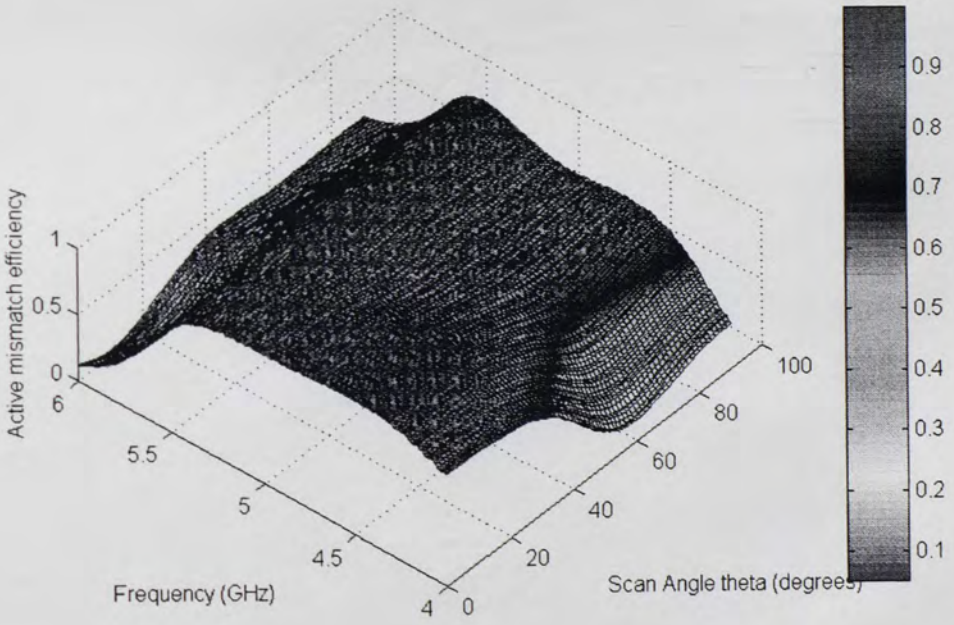

Figure 90. Efficiency of the Scan Element, H-Plane Array.

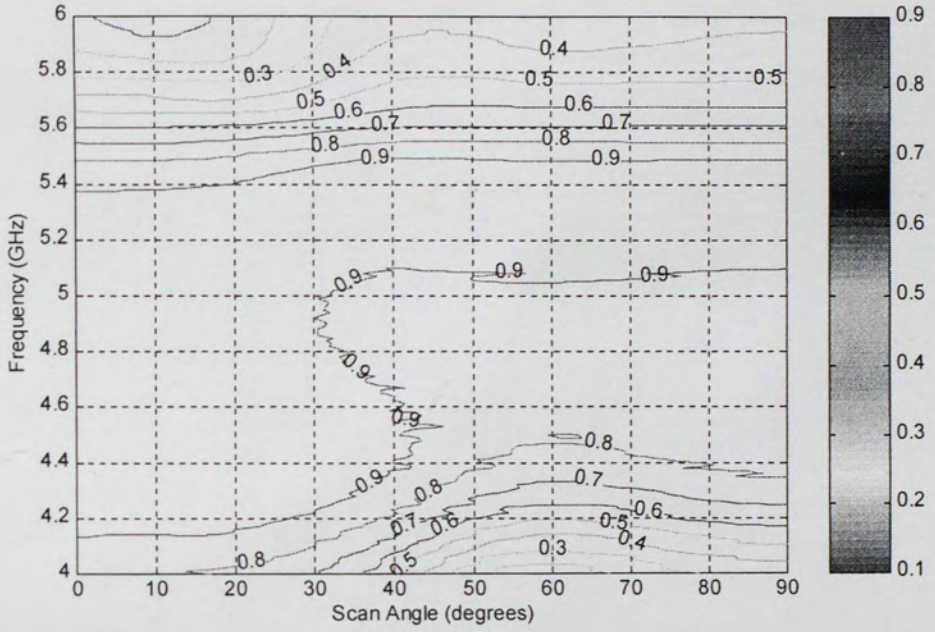

Figure 91. Contour Plot of the Efficiency for the Scan Element, H-Plane Array.

7.3.4 Planar Array Scan Element Patterns

The scan element pattern characteristics for the 25-element Planar Array are presented in Figures 92 through 108. Although in these results only one element is being fed while the other elements are terminated in 50 ohms, several conclusions can be extrapolated that will determine the performance of the scanning-array once all the elements are active.

The radiation parameters can be calculated from the electric fields predicted using the near to far zone transformation. These results can be compared to those for the isolated element.

The radiation pattern has a maximum at phi = 0 degrees, theta = 0 degrees

The mismatch loss is equal to: -0.313258 dB

The input power at the antenna port is equal to: 0.0093041 Watts

The total radiated power is equal to: 0.00394267 Watts

The average radiated power per steradian is equal to: 0.000313748 Watts/steradian

The directivity is equal to: 9.06976 dB

The gain is equal to: 5.02767 dB or 2.92767 dbi

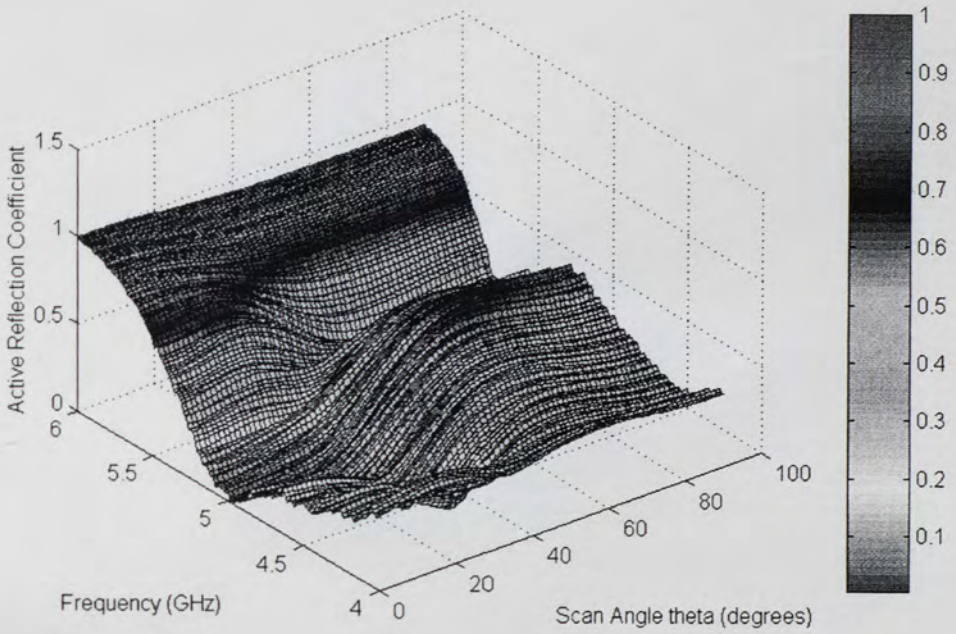

Figure 92. Active Reflection Coefficient for Planar Array, phi-cut = 0 degrees.

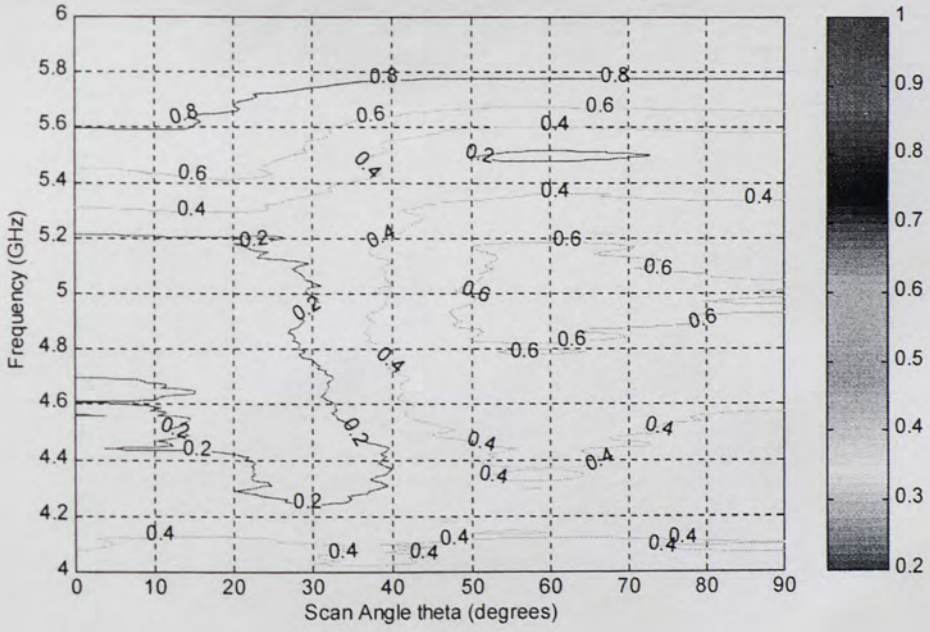

Figure 93. Active Reflection Coefficient for the Planar Array, phi-cut = 0 degrees.

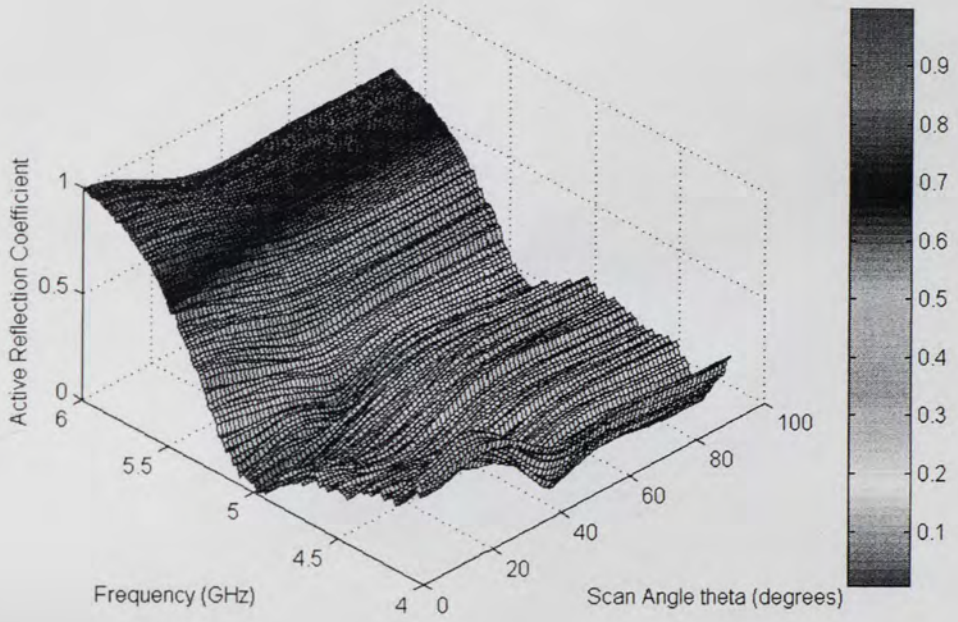

Figure 94. Active Reflection Coefficient for the Planar Array, phi-cut = 90 degrees.

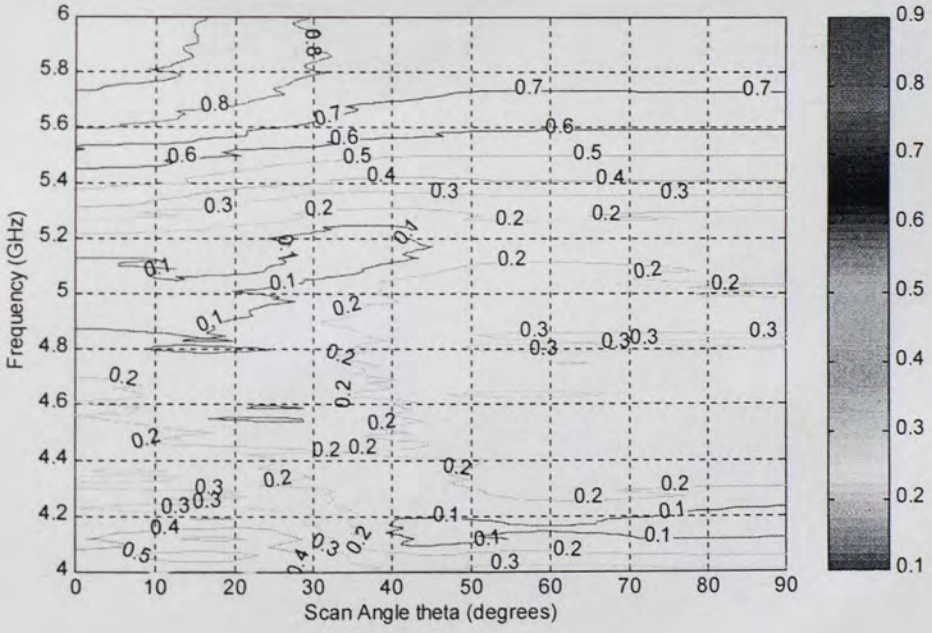

Figure 95. Active Reflection Coefficient for the H-Plane Array, phi-cut = 90 degrees.

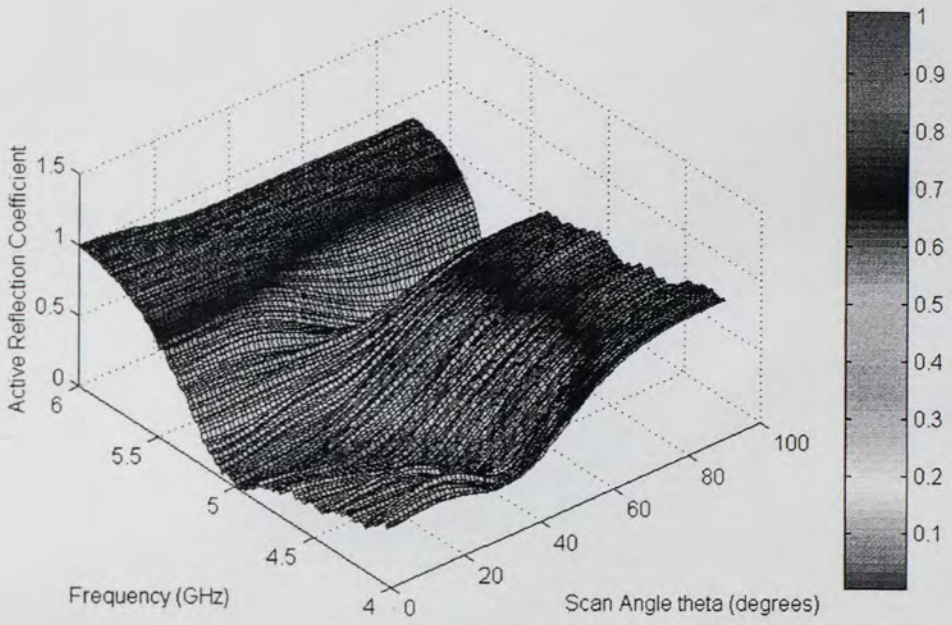

Figure 96. Active Reflection Coefficient for the Planar Array, phi-cut = 45 degrees.

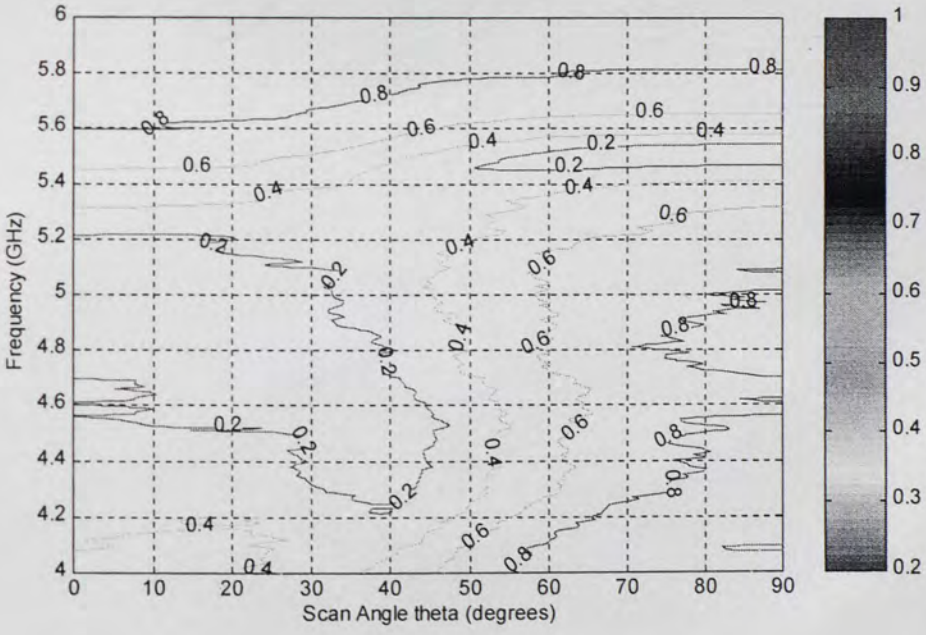

Figure 97. Active Reflection Coefficient for the Planar Array, phi-cut = 45 degrees.

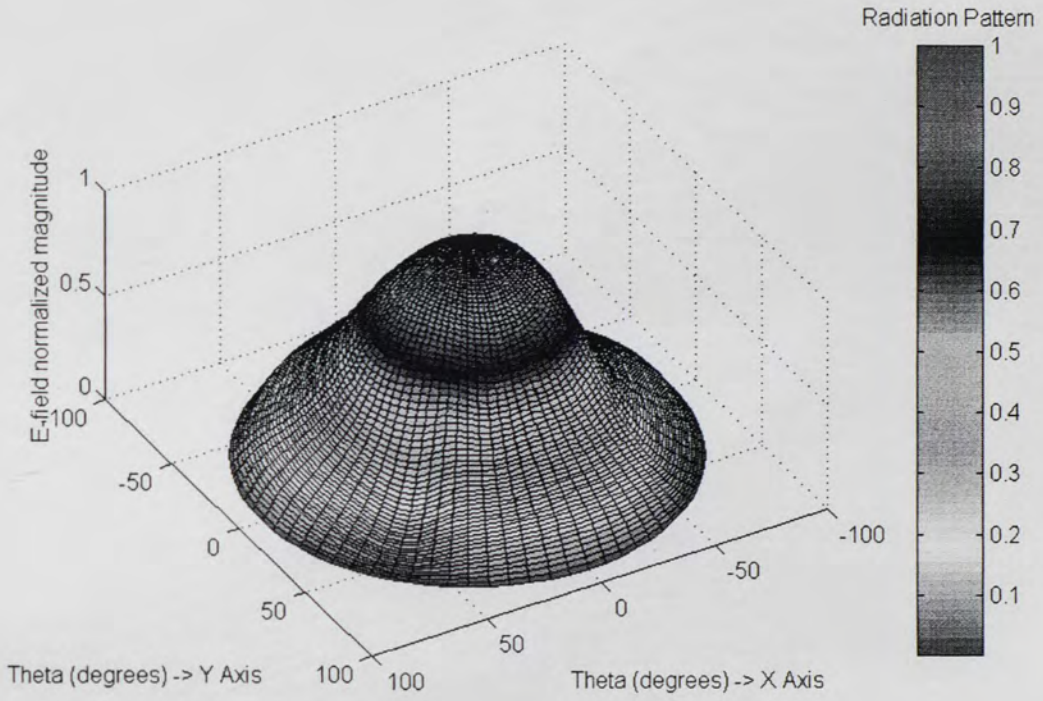

Figure 98. 3-D Mapped Scan Element Pattern for the Planar Array at 4.75 GHz.

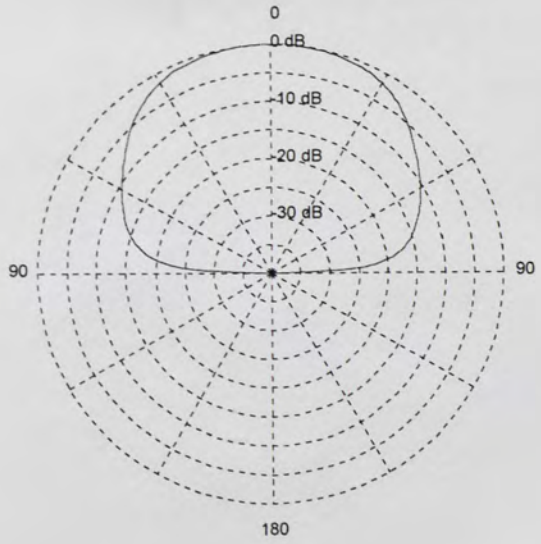

Figure 99. H-Plane Scan Element Pattern, Planar Array, phi-cut = 0, 4.75 GHz.

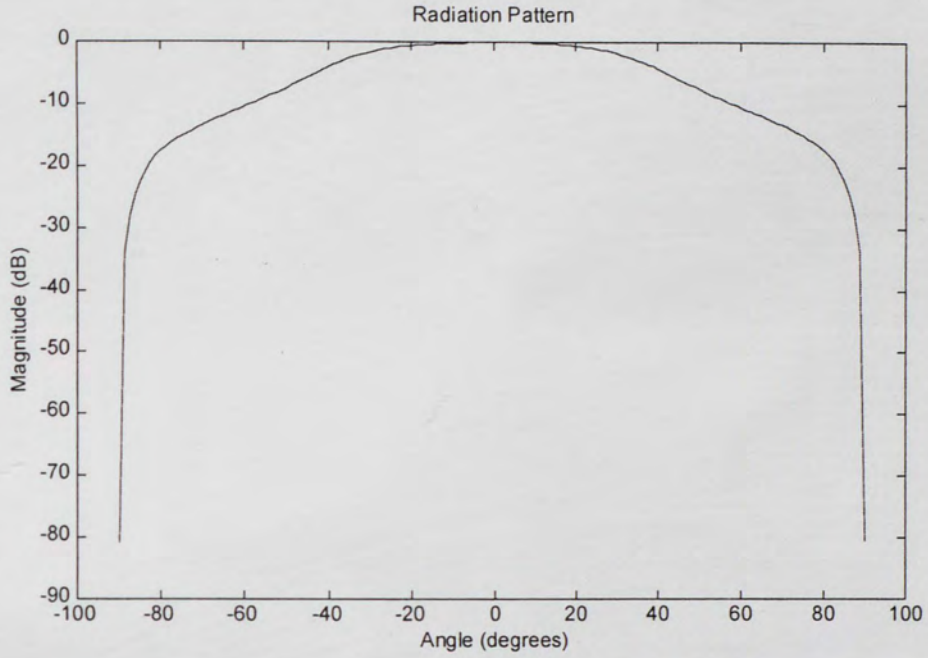

Figure 100. H-Plane Scan Element Pattern, Planar Array, phi-cut = 0, 4.75 GHz.

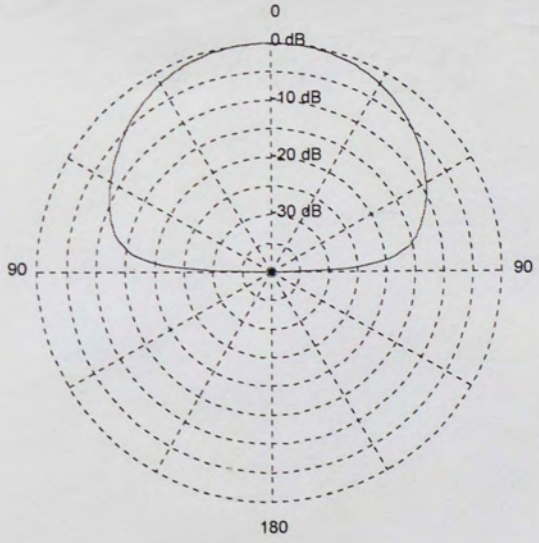

Figure 101. E-Plane Scan Element Pattern, Planar Array, phi-cut = 90, 4.75 GHz.

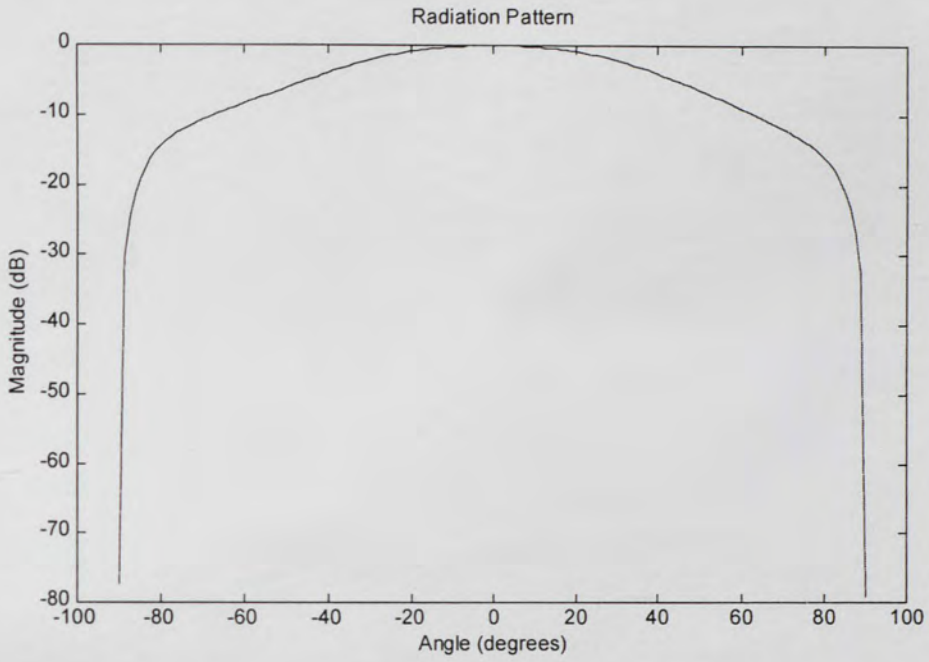

Figure 102. E-Plane Scan Element Pattern Planar Array, phi-cut = 90, 4.75 GHz.

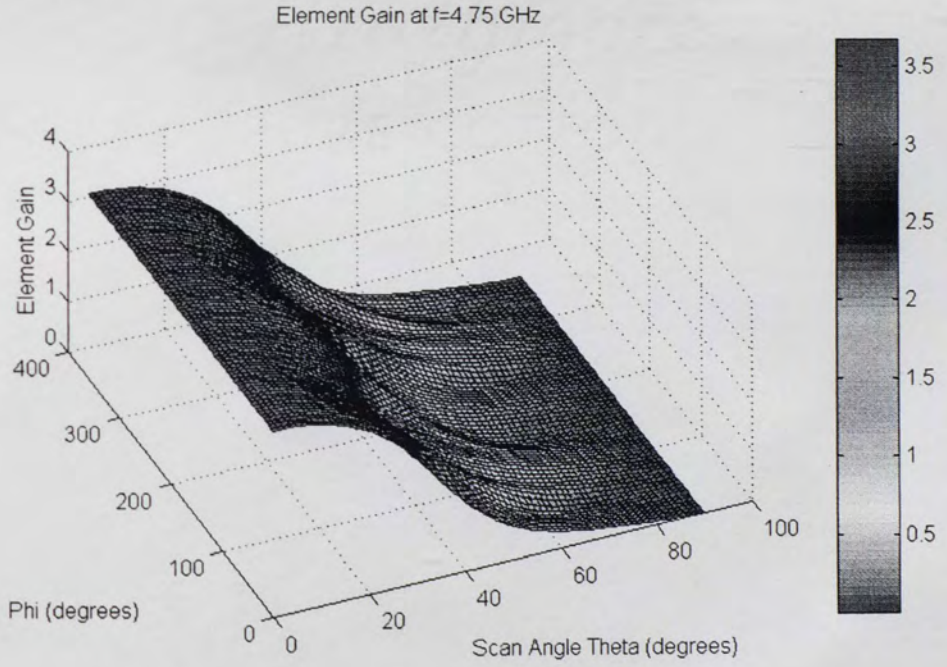

Figure 103. Gain of the Scan Element at 4.75 GHz.

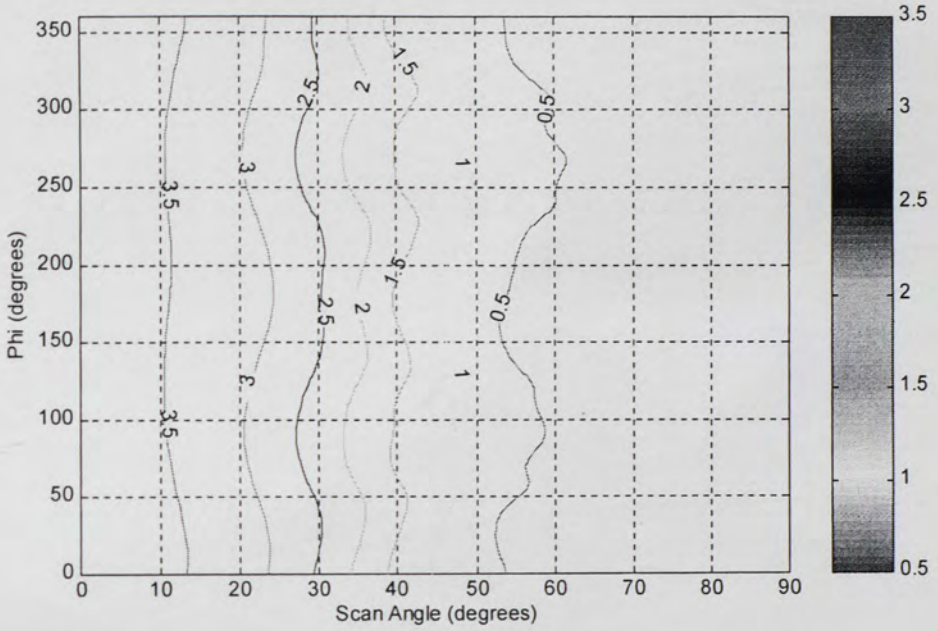

Figure 104. Gain of the Scan Element at 4.75 GHz.

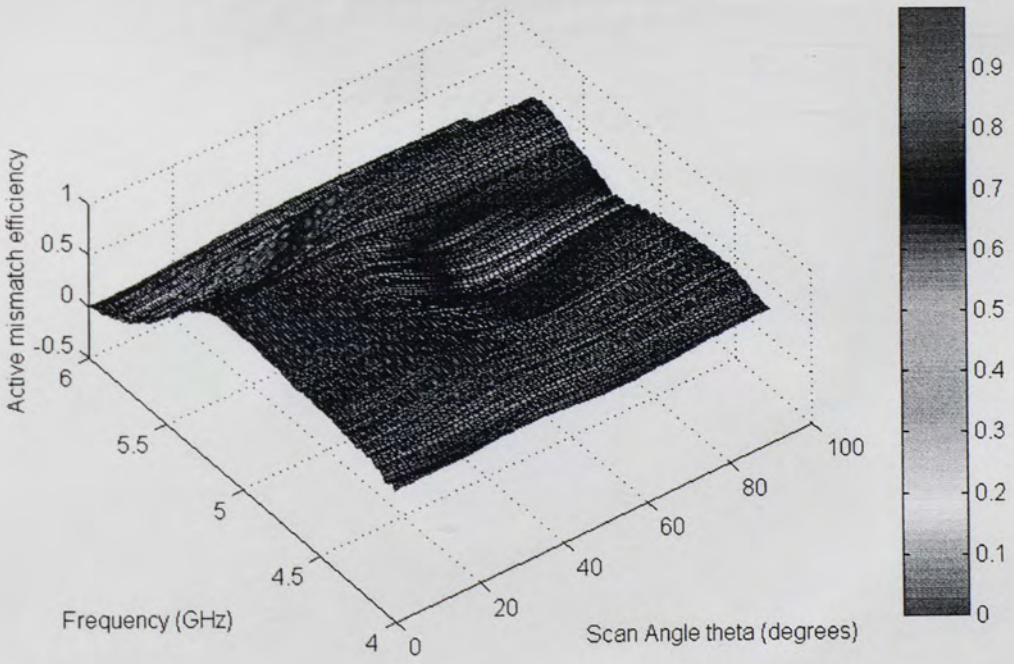

Figure 105. Efficiency of the Scan Element, phi-cut = 0 degrees.

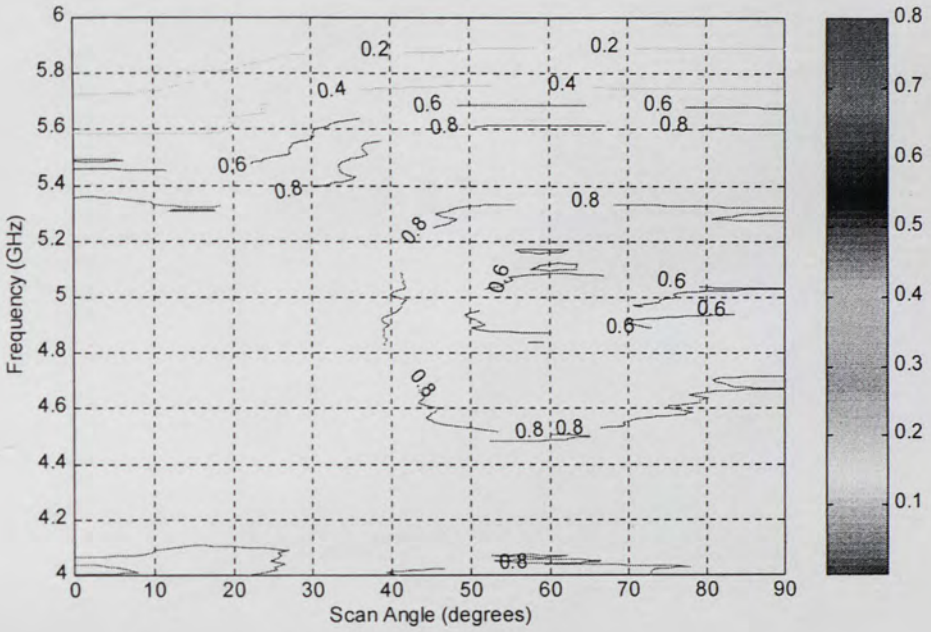

Figure 106. Efficiency of the Scan Element, phi-cut = 0 degrees.

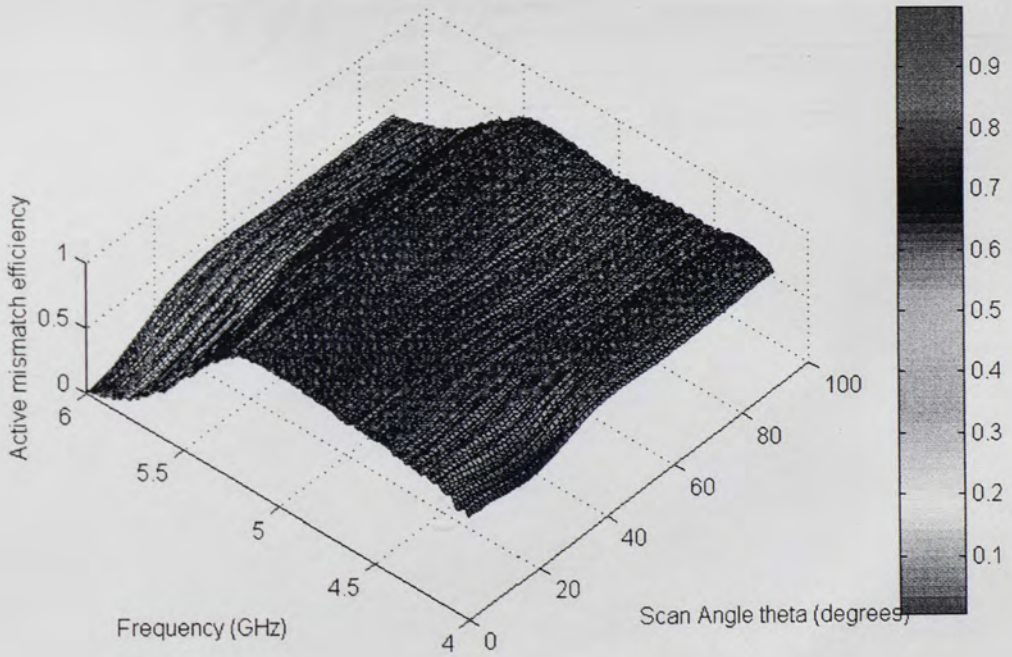

Figure 107. Efficiency of the Scan Element, phi-cut = 90 degrees.

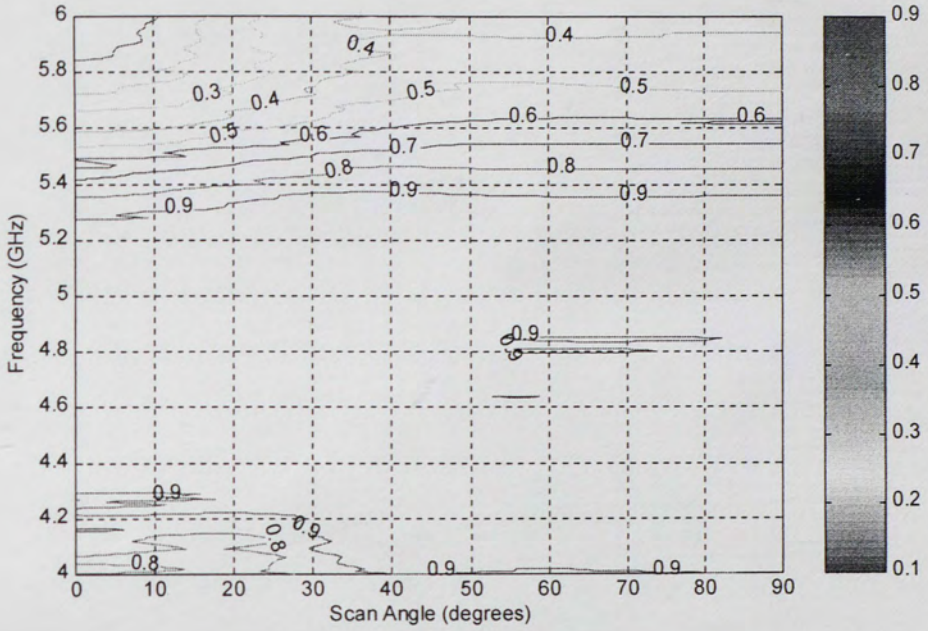

Figure 108. Efficiency for the Scan Element, phi-cut = 90 degrees.

7.3.5 E-Plane Phased Array Characteristics

The scan element pattern characteristics for the eight-element E-Plane Array are presented in Figures 109 through 120. Broadband results have been obtained for the scanning-array when all the elements are active.

The radiation parameters can be calculated from the electric fields predicted using the scan element patterns. The radiation parameters for the E-plane Array scanning at 0 degrees are:

The radiation pattern has a maximum at phi = 0 degrees, theta = 0 degrees

The mismatch loss is equal to: -0.414759 dB

The input power at the antenna port is equal to: 0.0750658 Watts

The total radiated power is equal to: 0.0489373 Watts

The average radiated power per steradian is equal to: 0.0038943 Watts/steradian

The directivity is equal to: 16.1449 dB

The radiation efficiency is equal to: 65.1925 percent or -1.85802 dB

The gain is equal to: 13.8721 dB or 11.7721 dbi

The radiation parameters for the E-plane Array scanning at 30 degrees are:

The radiation pattern has a maximum at phi = 90 degrees, theta = 30 degrees

The mismatch loss is equal to: -0.414759 dB

The input power at the antenna port is equal to: 0.0750658 Watts

The total radiated power is equal to: 0.026617 Watts

The average radiated power per steradian is equal to: 0.00211812 Watts/steradian

The directivity is equal to: 16.1166 dB

The gain is equal to : 11.199 dB or 9.09898 dbi

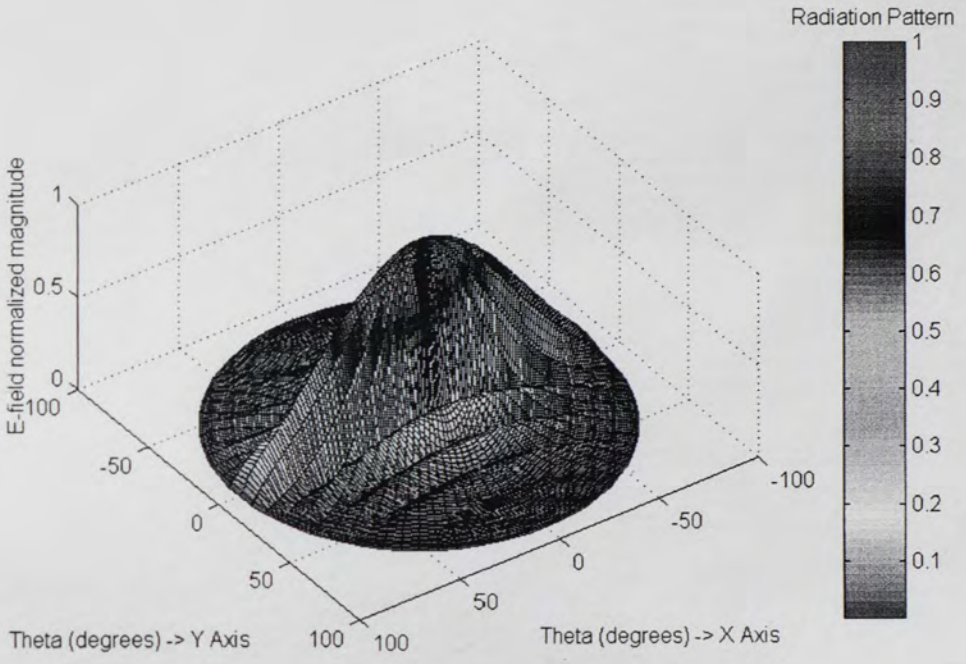

Figure 109. 3-D Mapped Pattern for E-Plane Array, scan angle = 0, 4.75 GHz.

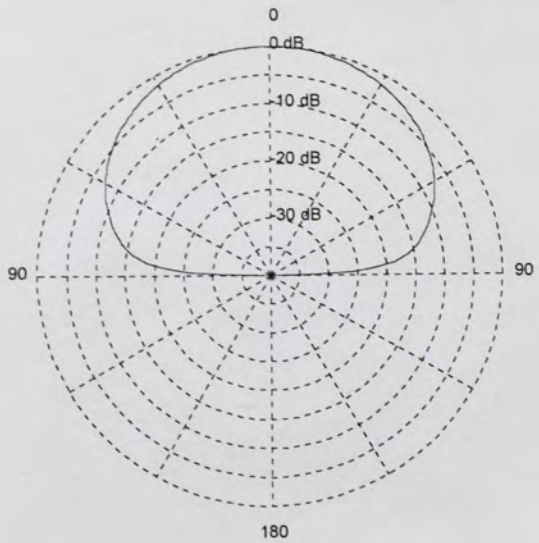

Figure 110. H-Plane radiation Pattern of the E-Plane Array, scan angle = 0 degrees, phi-cut = 0, 4.75 GHz.

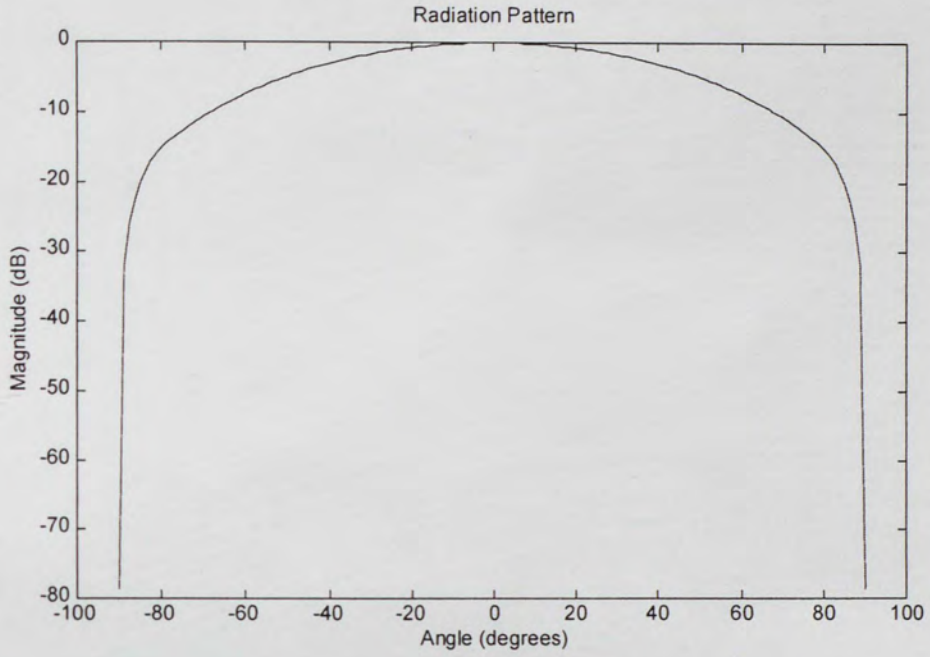

Figure 111. H-Plane radiation pattern for the E-Plane Array, scan angle = 0 degrees, phi-cut = 0, 4.75 GHz.

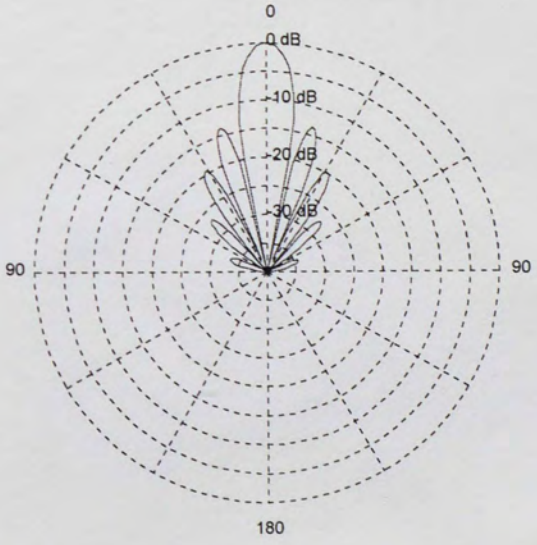

Figure 112. E-Plane Radiation Pattern for the E-Plane Array, scan angle = 0 degrees, phi-cut = 90 degrees, 4.75 GHz.

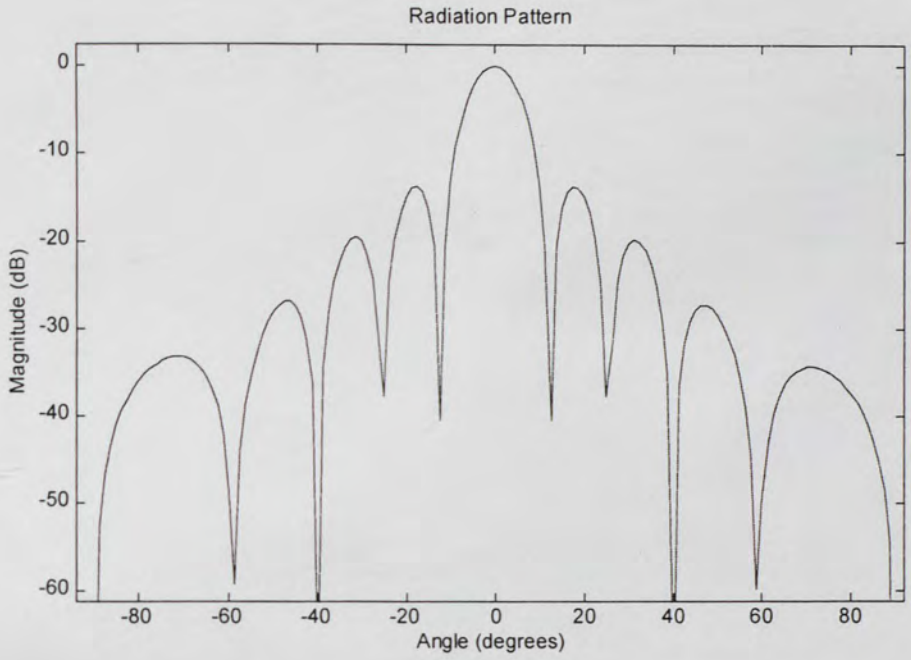

Figure 113. E-Plane Pattern, E-Plane Array, scan angle = 0, phi-cut = 90, 4.75 GHz.

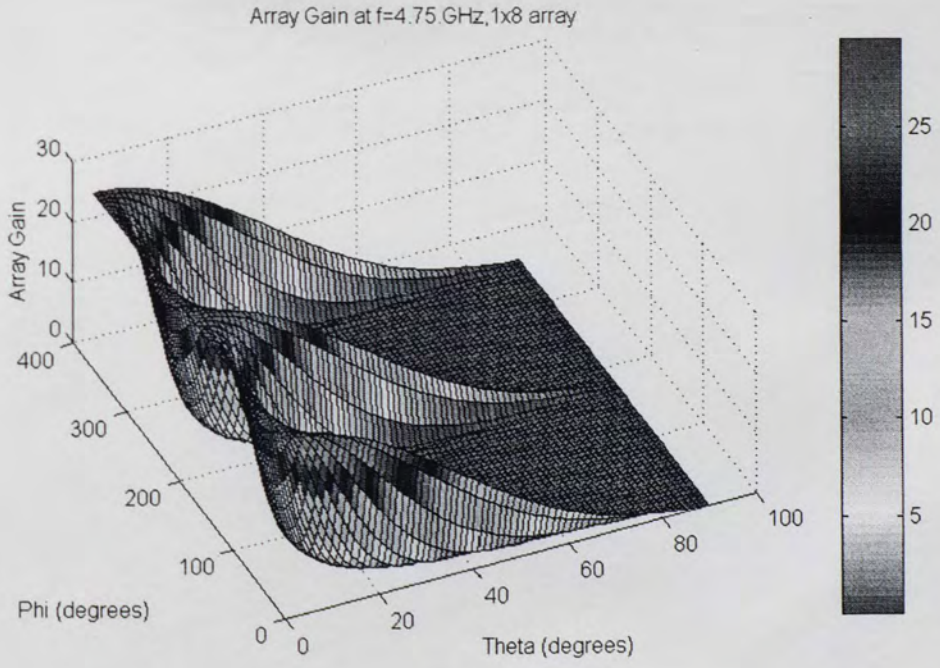

Figure 114. Gain of the E-Plane Array at 4.75 GHz, scan angle = 0 degrees.

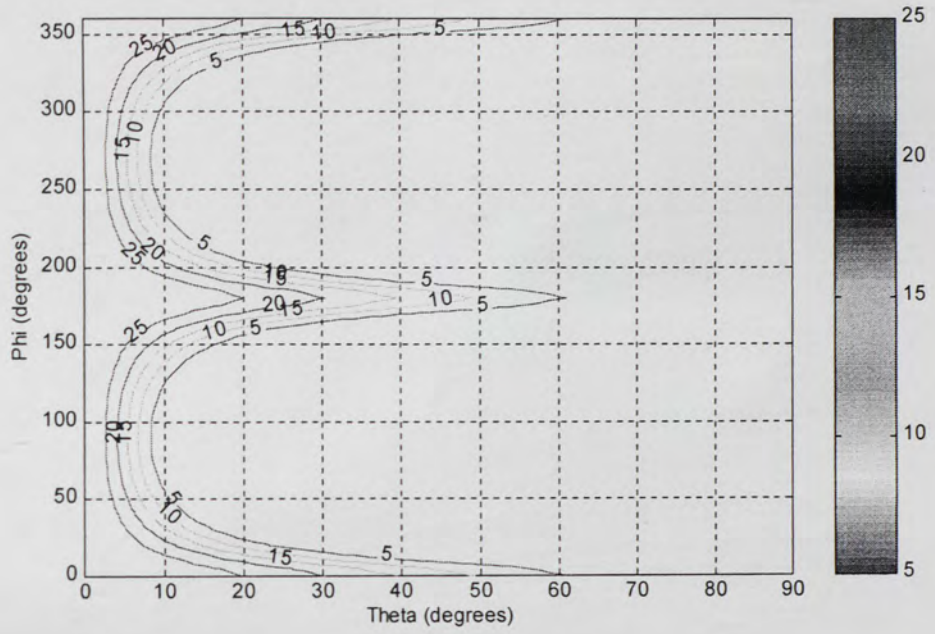

Figure 115. Gain of the E-Plane Array, scan angle = 0 degrees, 4.75 GHz.

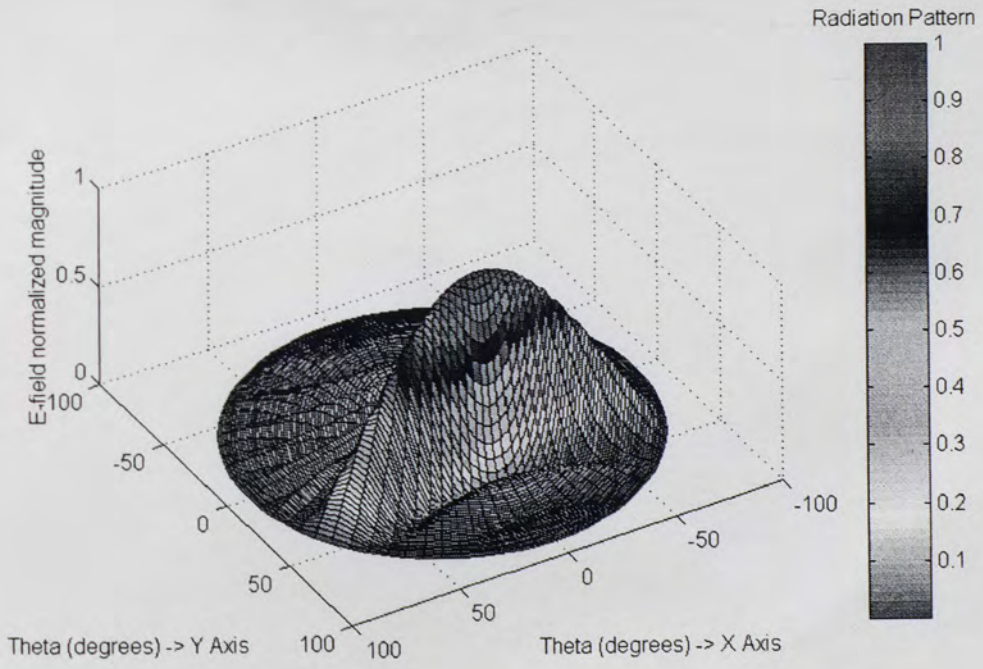

Figure 116. 3-D Pattern for the E-Plane array, scan angle = 30, 4.75 GHz.

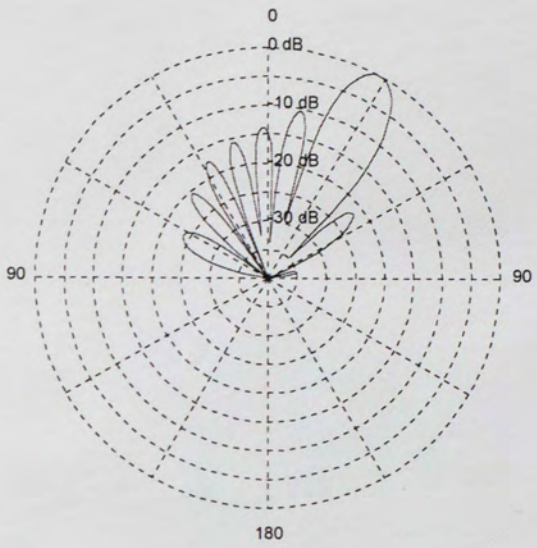

Figure 117. E-Plane Radiation Pattern for the E-Plane Array, scan angle = 30 degrees, phi-cut = 90 degrees, 4.75 GHz.

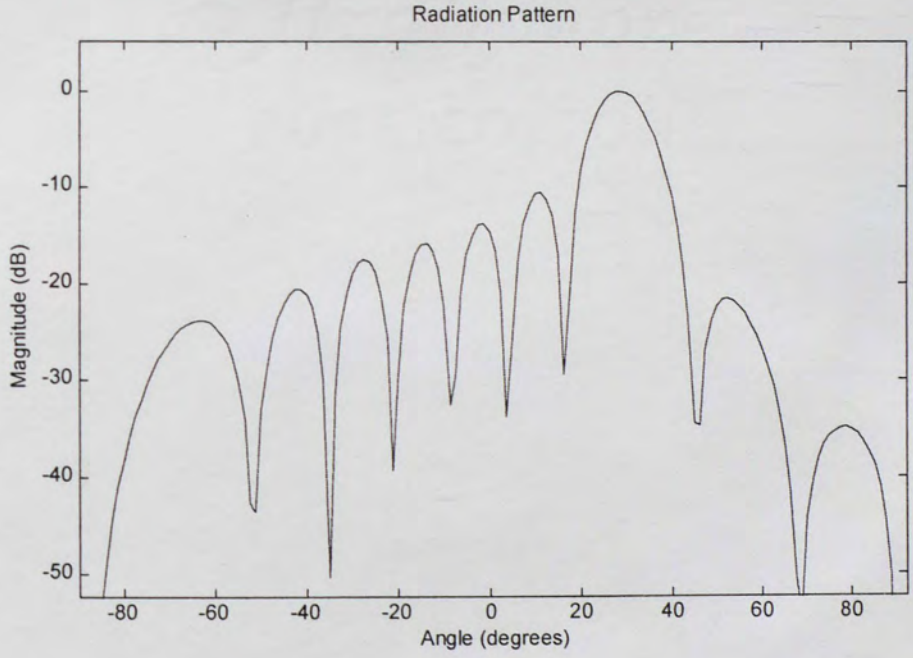

Figure 118. E-Plane Radiation Pattern for the E-Plane Array, scan angle = 30 degrees, phi-cut = 90 degrees, 4.75 GHz.

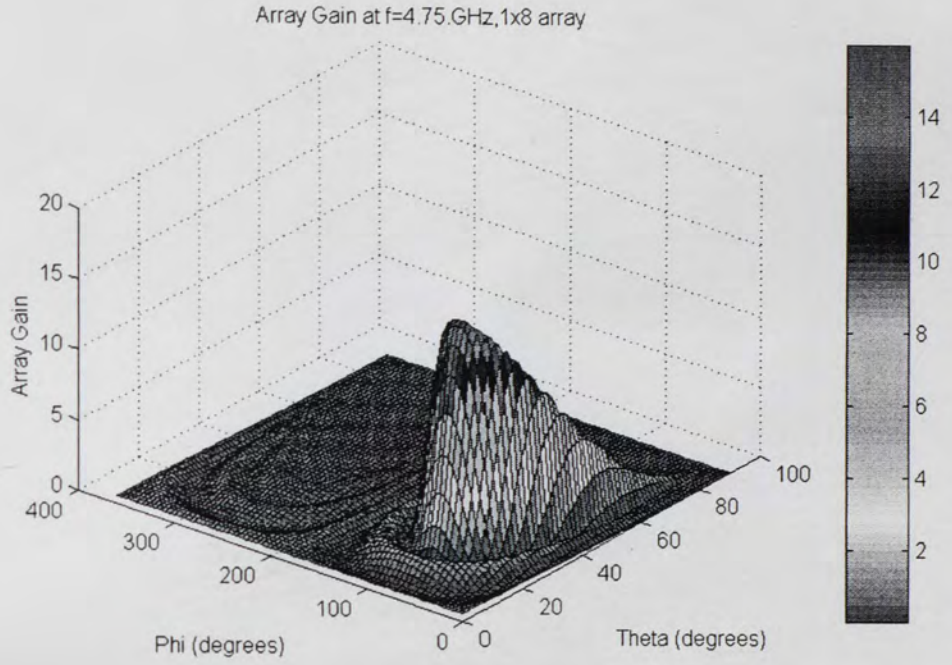

Figure 119. Gain for the E-plane Array, scan angle = 30 degrees, 4.75 GHz.

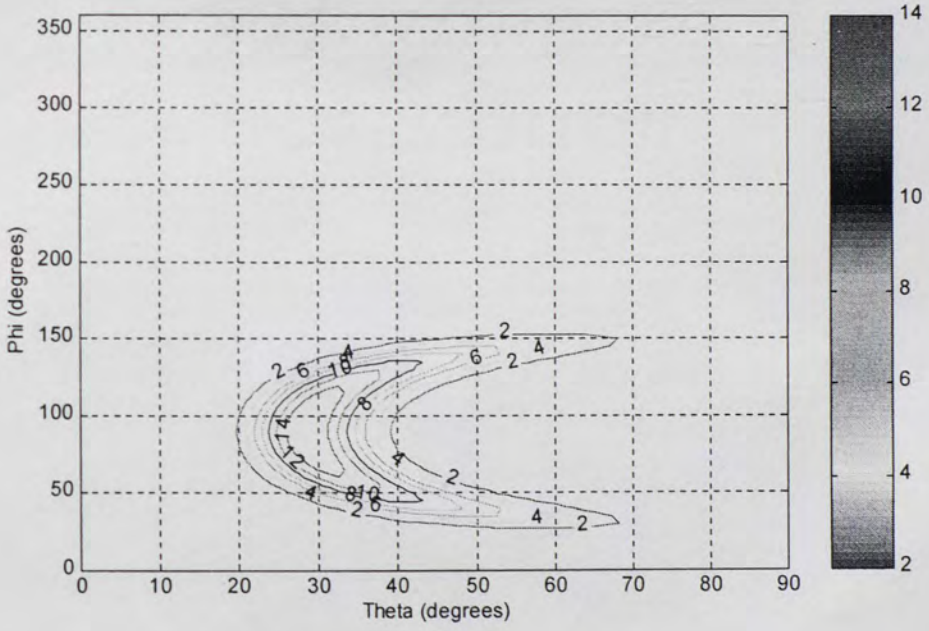

Figure 120. Gain of the E-Plane Array, scan angle = 30 degrees, 4.75 GHz.

7.3.6 H-Plane Array Scanning Characteristics

The scan element pattern characteristics for the eight-element H-Plane Array are presented in Figures 121 through 132. Broadband results have been obtained for the scanning-array when all the elements are active.

The radiation parameters can be calculated from the electric fields predicted using the scan element patterns. The radiation parameters for the H-plane Array scanning at 0 degrees are:

The radiation pattern has a maximum at phi = 0 degrees, theta = 0 degrees

The mismatch loss is equal to: -0.270424 dB

The input power at the antenna port is equal to: 0.0759095 Watts

The total radiated power is equal to: 0.0455992 Watts

The average radiated power per steradian is equal to: 0.00362867 Watts/steradian

The directivity is equal to: 16.5197 dB

The radiation efficiency is equal to: 60.0706 percent or -2.21338 dB

The gain is equal to: 14.0359 dB or 11.9359 dbi

The radiation parameters for the H-plane Array scanning at 30 degrees are:

The radiation pattern has a maximum at phi = 0 degrees, theta = 30 degrees

The mismatch loss is equal to: -0.270424 dB

The input power at the antenna port is equal to: 0.0759095 Watts

The total radiated power is equal to: 0.0314544 Watts

The average radiated power per steradian is equal to: 0.00250306 Watts/steradian

The directivity is equal to: 16.1039 dB

The gain is equal to: 12.0074 dB or 9.90737 dbi

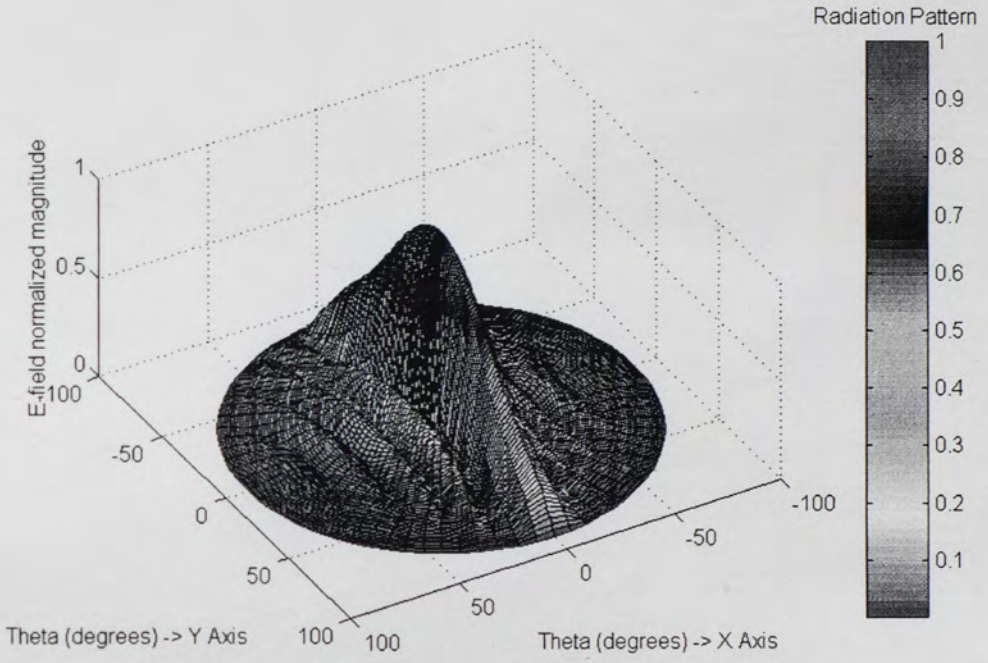

Figure 121. 3-D Radiation Pattern for the H-Plane Array, scan angle = 0, 4.75 GHz.

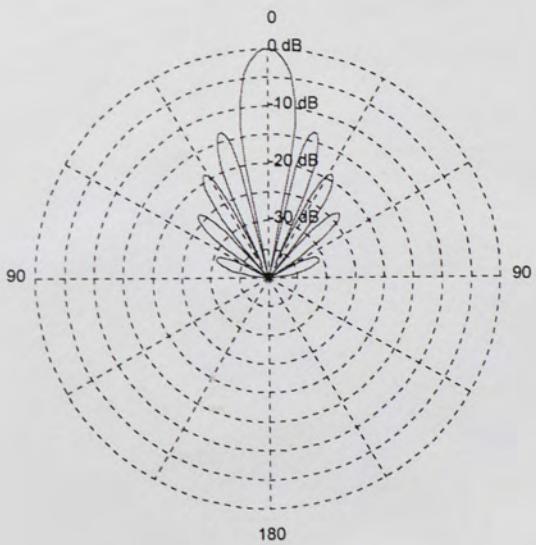

Figure 122. H-Plane Pattern, H-Plane Array, scan angle = 0, phi-cut = 0, 4.75 GHz.

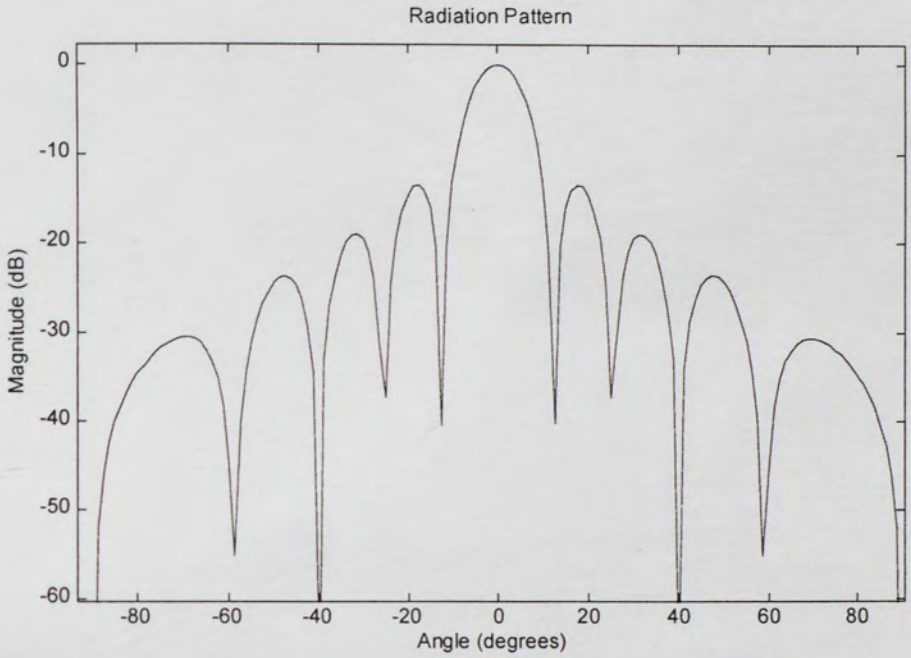

Figure 123. H-Plane Pattern, H-Plane Array, scan angle = 0, phi-cut = 0, 4.75 GHz.

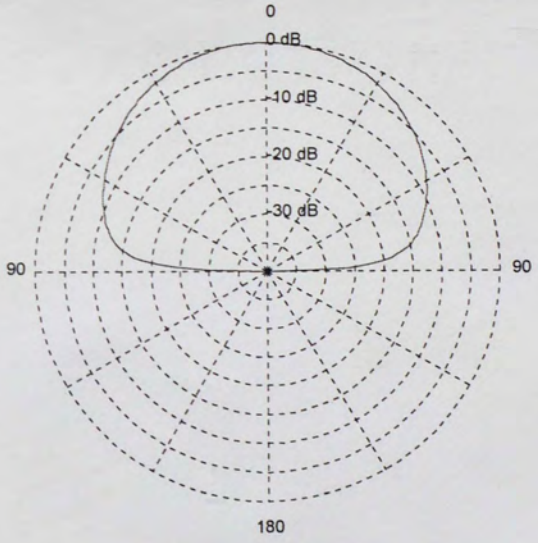

Figure 124. E-Plane Pattern, H-Plane Array, scan angle = 0, phi-cut = 90, 4.75 GHz.

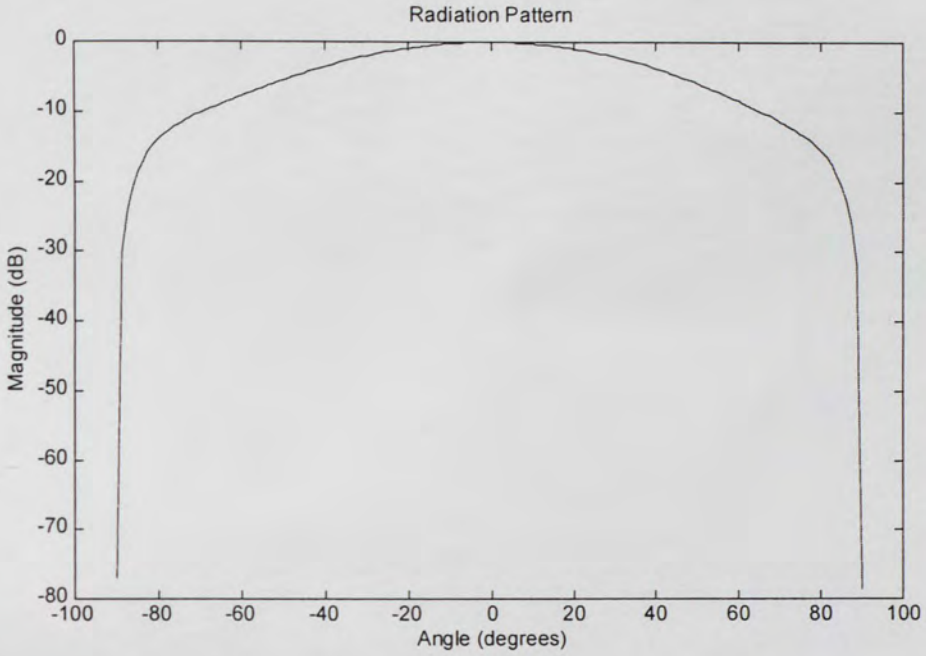

Figure 125. E-Plane Pattern, H-Plane Array, scan angle = 0, phi-cut = 90, 4.75 GHz.

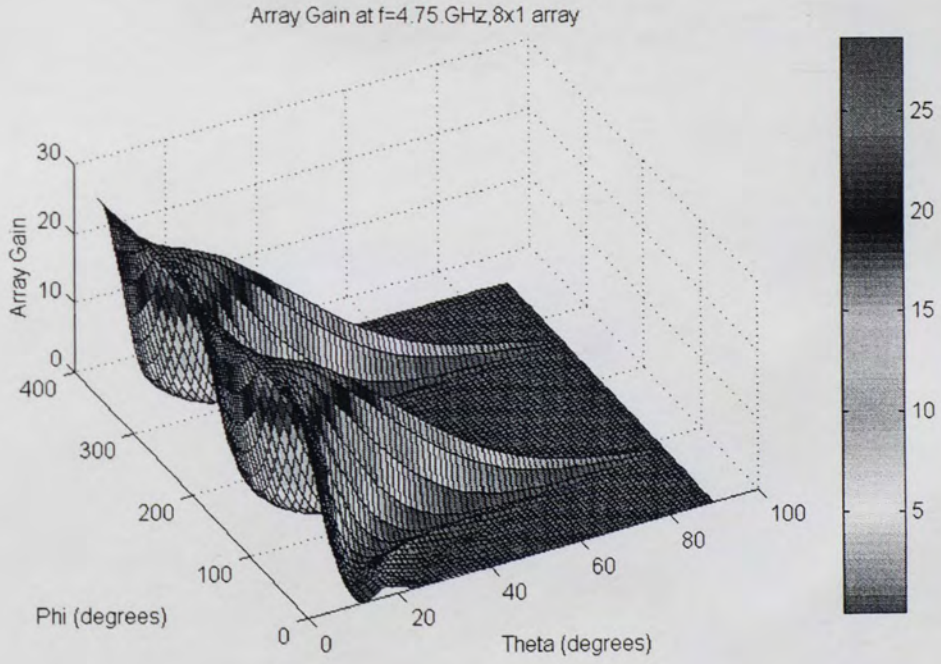

Figure 126. Gain of the H-Plane Array, scan angle = 0 degrees at 4.75 GHz.

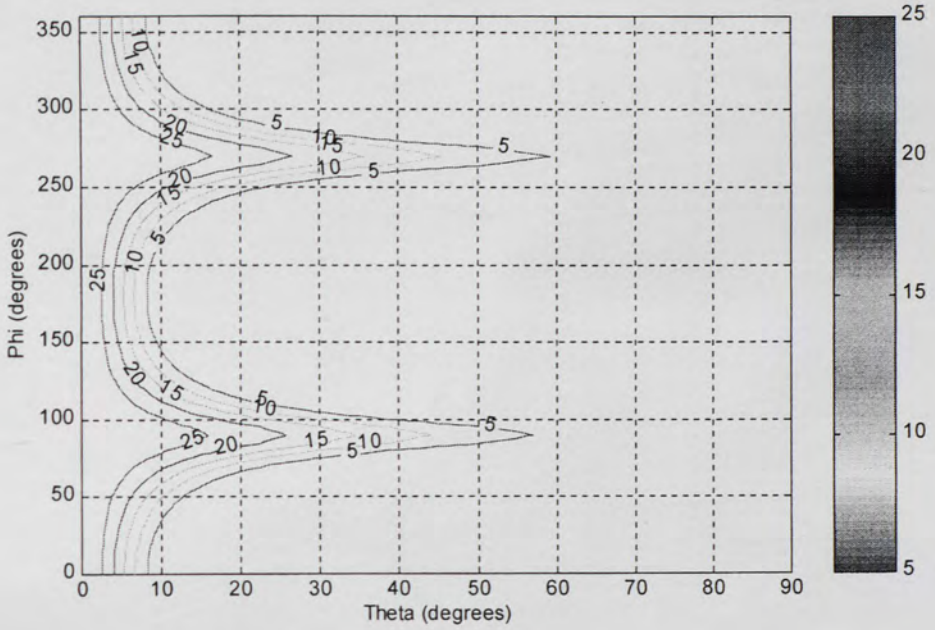

Figure 127. Gain of the H-Plane Array, scan angle = 0 degrees, 4.75 GHz.

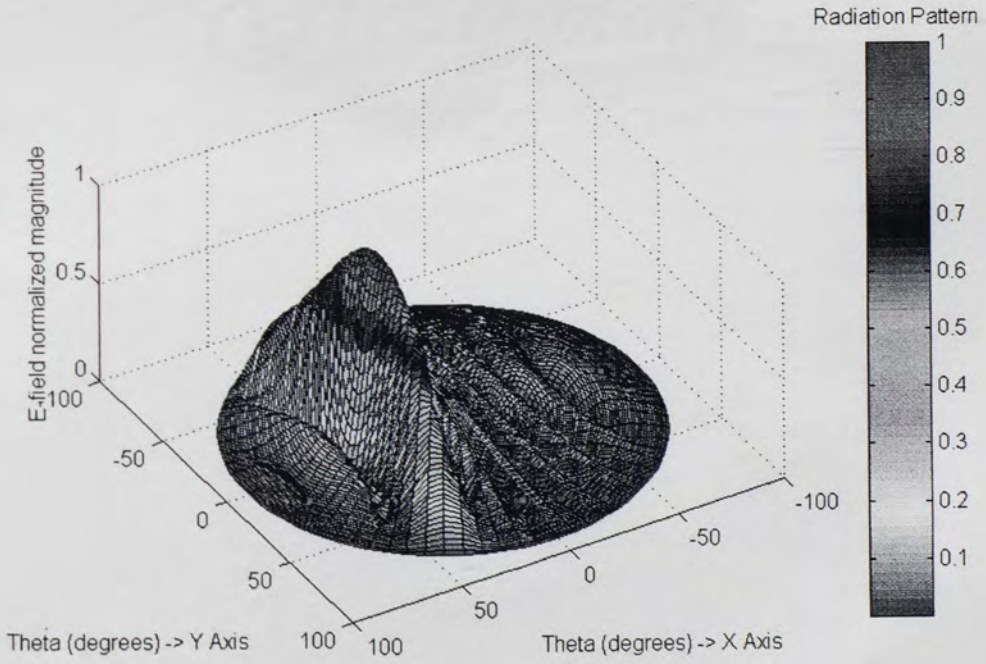

Figure 128. 3-D Radiation Pattern, H-Plane Array, scan angle = 30, 4.75 GHz.

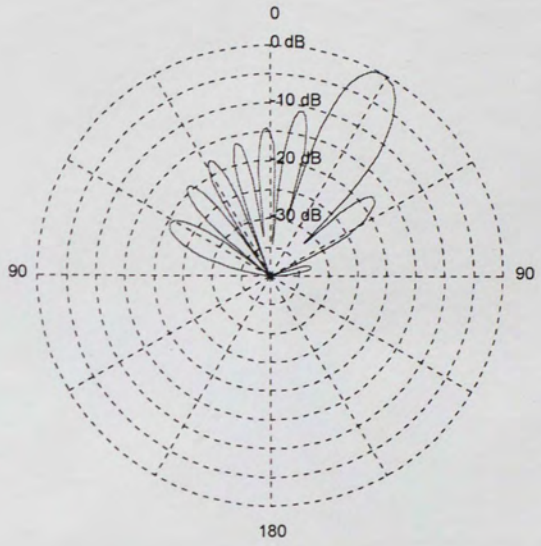

Figure 129. H-Plane Pattern, H-Plane Array, scan angle = 30 degrees, 4.75 GHz.

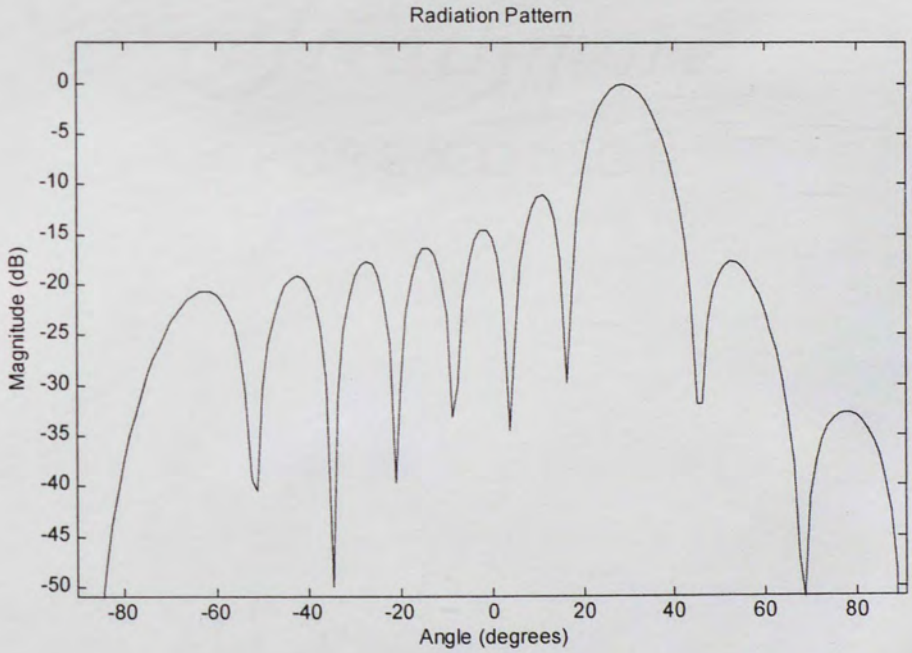

Figure 130. H-Plane Pattern for the H-Plane Array, scan angle = 30, 4.75 GHz.

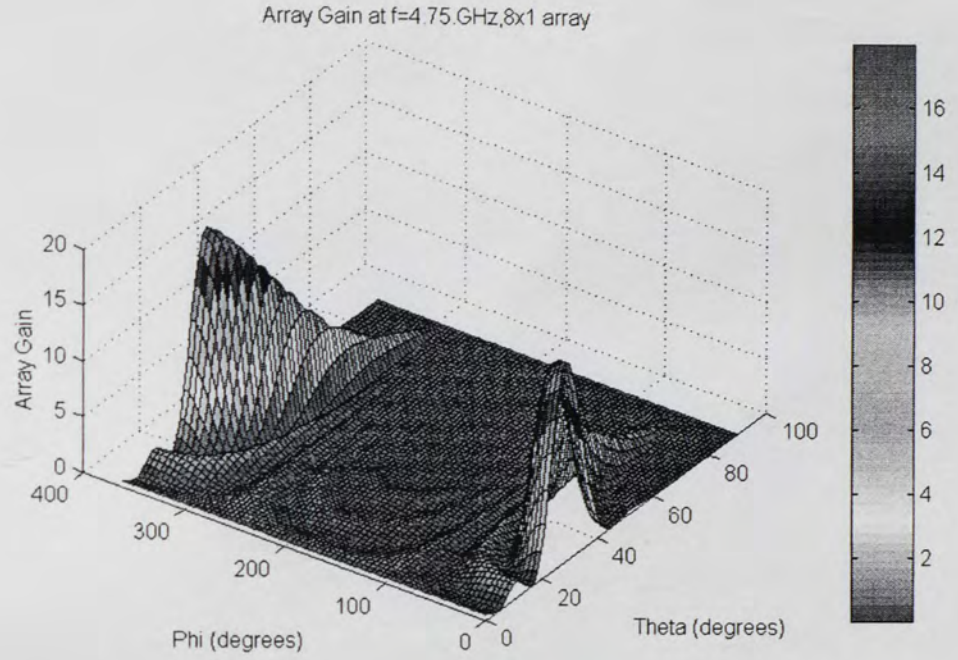

Figure 131. Gain for the H-Plane Array at 4.75 GHz, scan angle = 30 degrees.

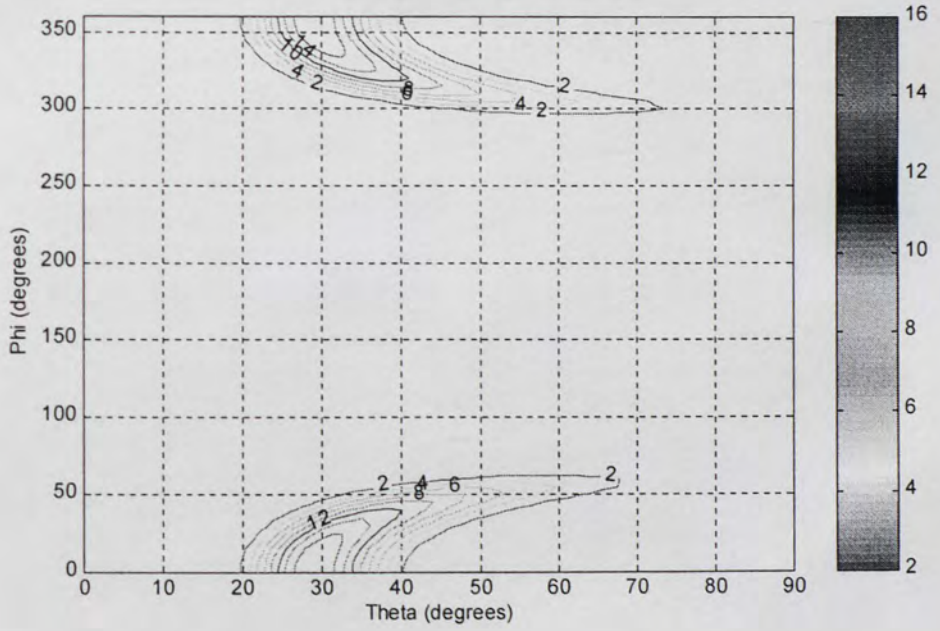

Figure 132. Gain for the H-Plane Array at 4.75 GHz, scan angle = 30 degrees.

7.3.7 Planar Array Scanning Characteristics

The scan element pattern characteristics for the 25-element Planar Array are presented in Figures 133 through 143. Broadband results have been obtained for the scanning-array when all the elements are active.

The radiation parameters for the phased array are calculated from the scan element patterns, and for the Planar Array scanning at $\theta = 0, \phi = 0$ degrees are:

The radiation pattern has a maximum at phi = 0 degrees, theta = 0 degrees

The mismatch loss is equal to: -0.313258 dB

The input power at the antenna port is equal to: 0.235455 Watts

The total radiated power is equal to: 0.17254 Watts

The average radiated power per steradian is equal to: 0.0137303 Watts/steradian

The directivity is equal to: 20.6146 dB

The radiation efficiency is equal to: 73.2792 percent or -1.35019 dB

The gain is equal to: 18.9511 dB or 16.8511 dbi

The radiation parameters for the planar array scanning at $\theta = 30, \phi = 0$ are:

The radiation pattern has a maximum at phi = 0 degrees, theta = 30 degrees

The mismatch loss is equal to: -0.313258 dB

The input power at the antenna port is equal to: 0.235455 Watts

The total radiated power is equal to: 0.132654 Watts

The average radiated power per steradian is equal to: 0.0105563 Watts/steradian

The directivity is equal to: 20.2037 dB

The gain is equal to: 17.3985 dB or 15.2985 dbi

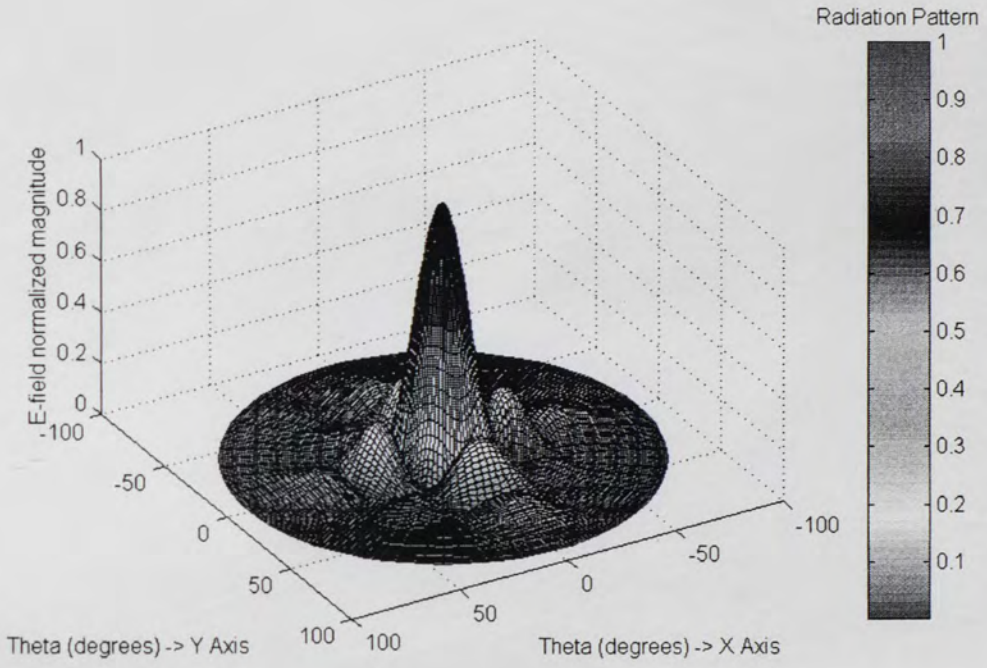

Figure 133. 3-D Mapped Pattern for the Planar Array, 4.75 GHz, scan angle = 0,0.

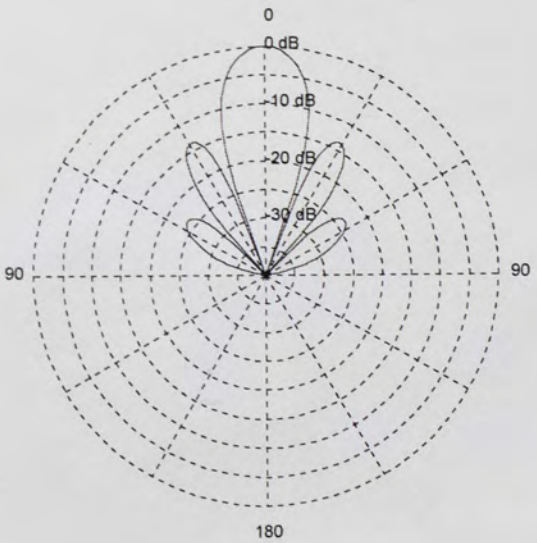

Figure 134. H-Plane Pattern, Planar Array, scan angle = 0,0, phi-cut = 0, 4.75 GHz.

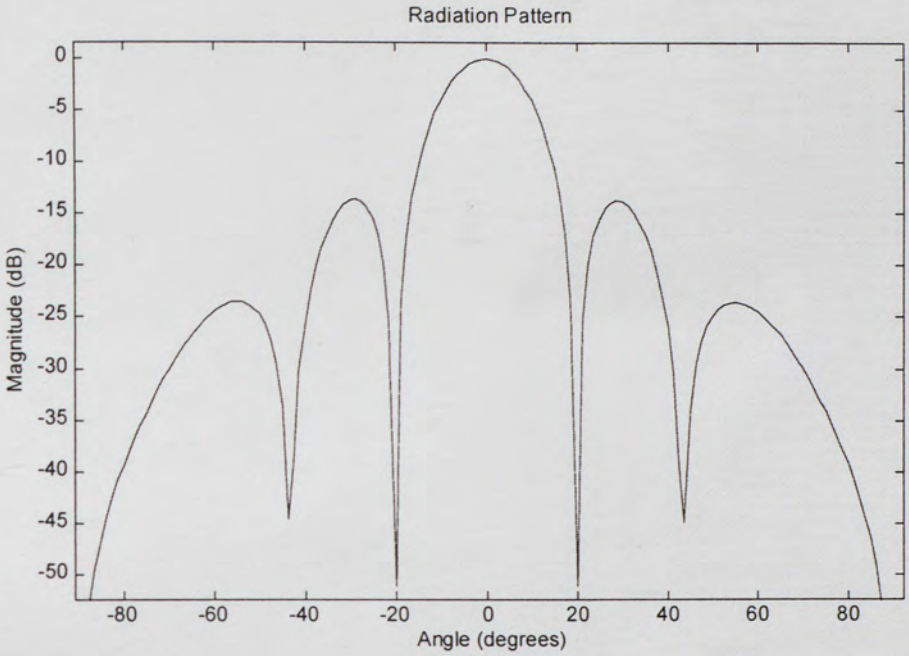

Figure 135. H-Plane Pattern, Planar Array, scan angle = 0,0, phi-cut = 0, 4.75 GHz.

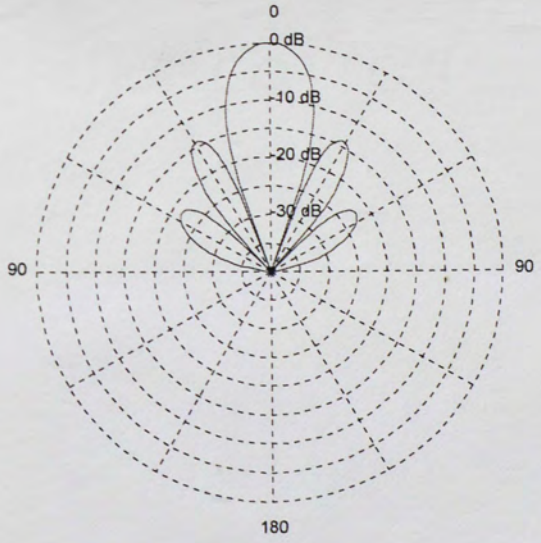

Figure 136. E-Plane Pattern, Planar Array, scan angle = 0,0, phi-cut = 90, 4.75 GHz.

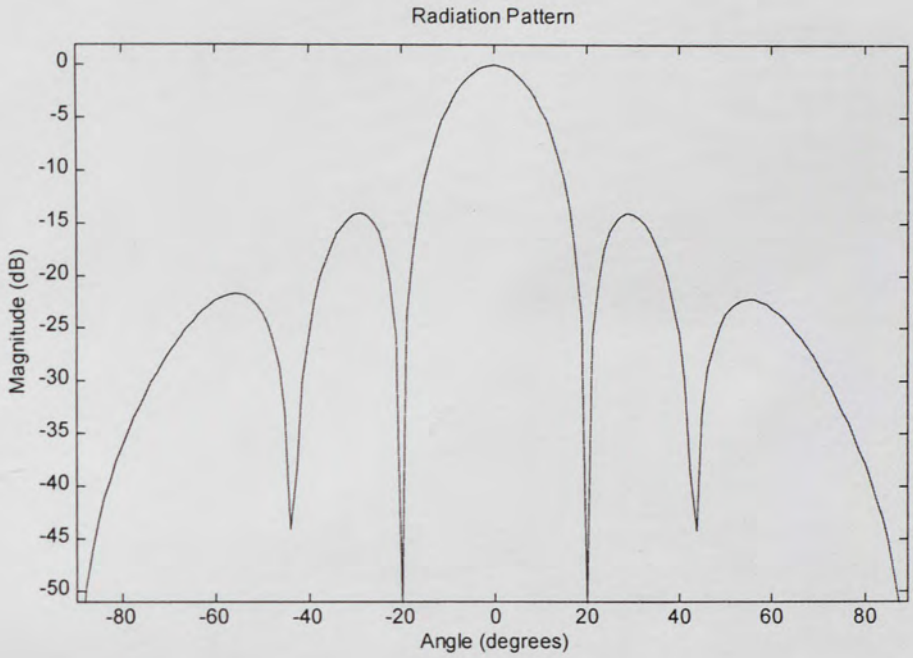

Figure 137. E-Plane Pattern, Planar Array, scan angle = 0,0, phi-cut = 90, 4.75 GHz.

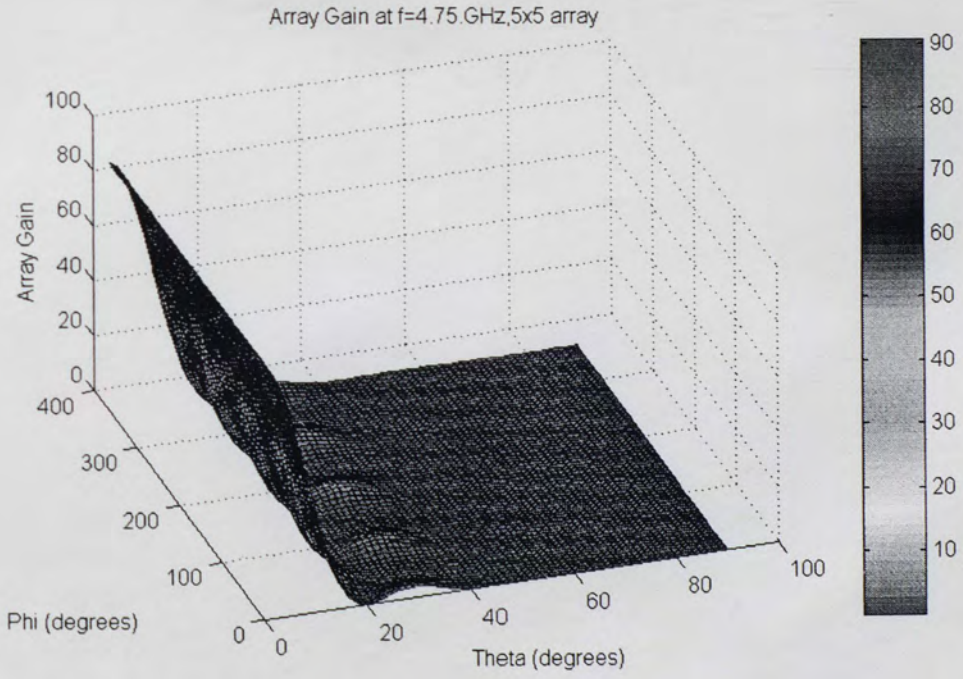

Figure 138. Gain for the Planar Array at 4.75 GHz, scan angle = 0,0.

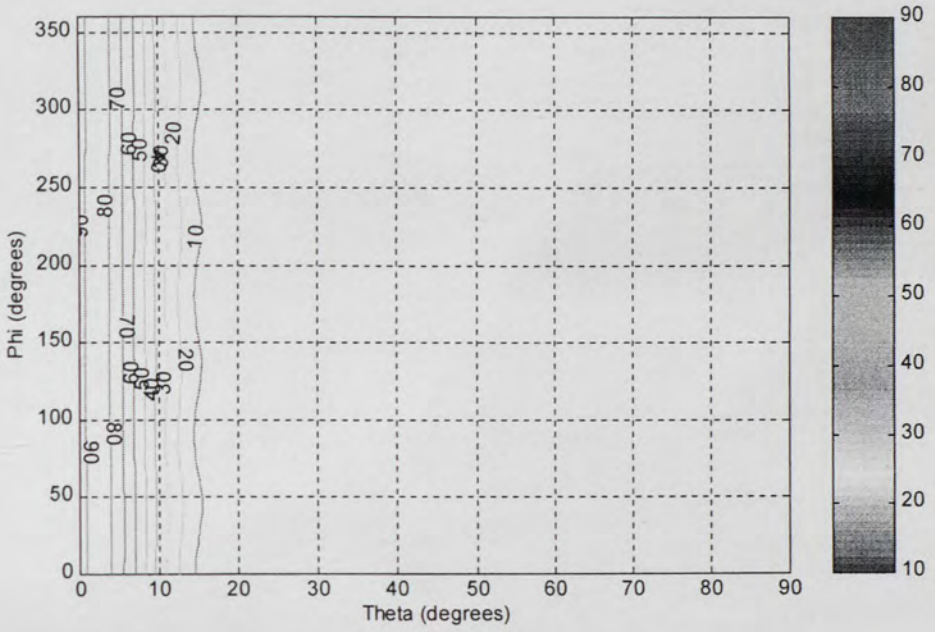

Figure 139. Gain for the Planar Array at 4.75 GHz, scan angle = 0,0.

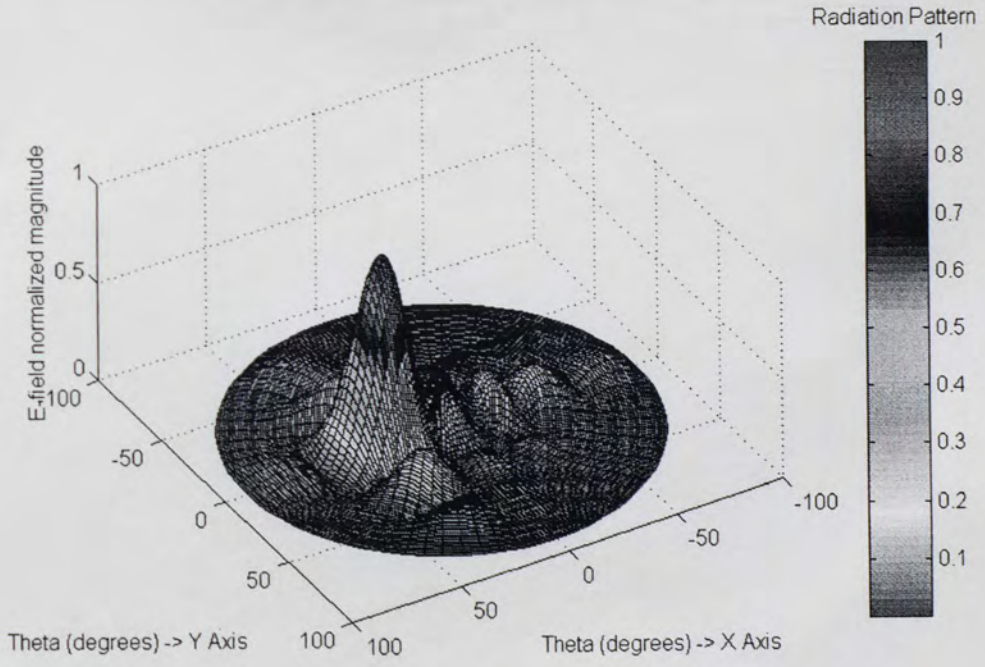

Figure 140. 3-D Mapped Pattern for the Planar Array, 4.75 GHz, scan angle = 30,0.

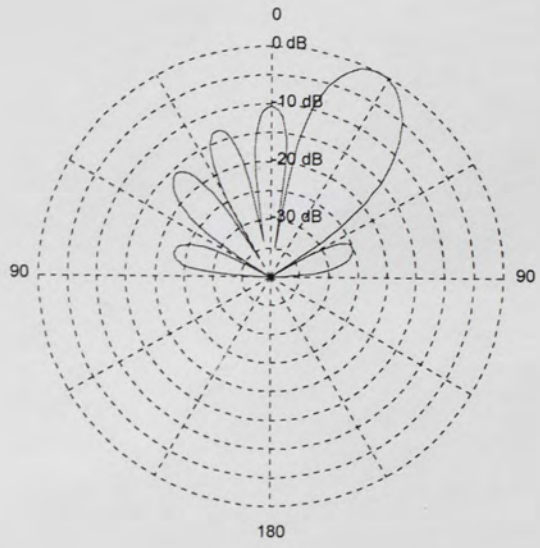

Figure 141. H-Plane Pattern, Planar Array, scan angle = 30,0, phi-cut = 0, 4.75 GHz.

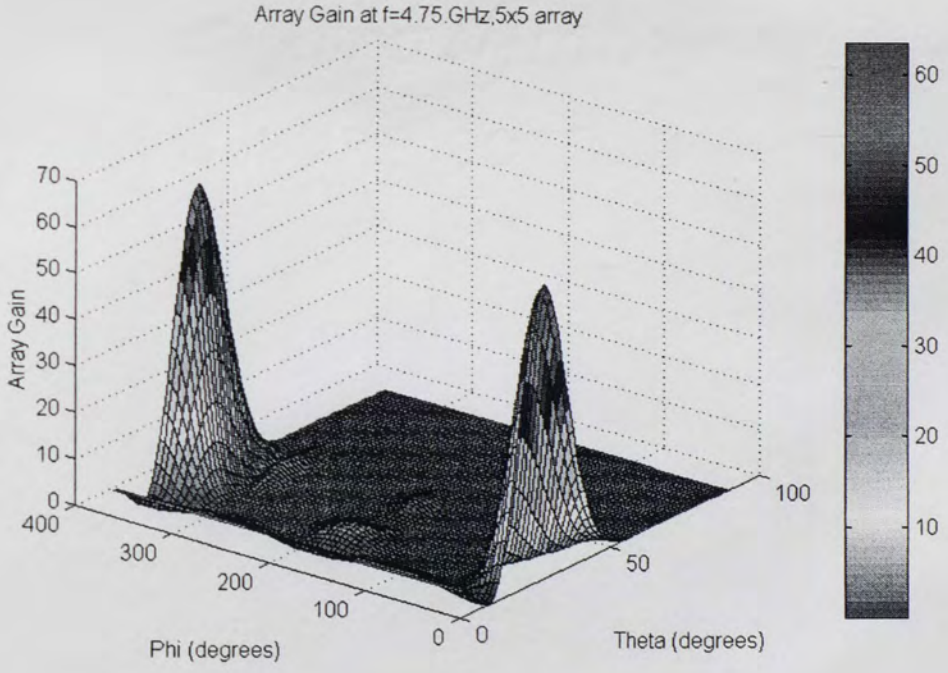

Figure 142. Gain for the Planar Array at 4.75 GHz, scan angle = 30,0.

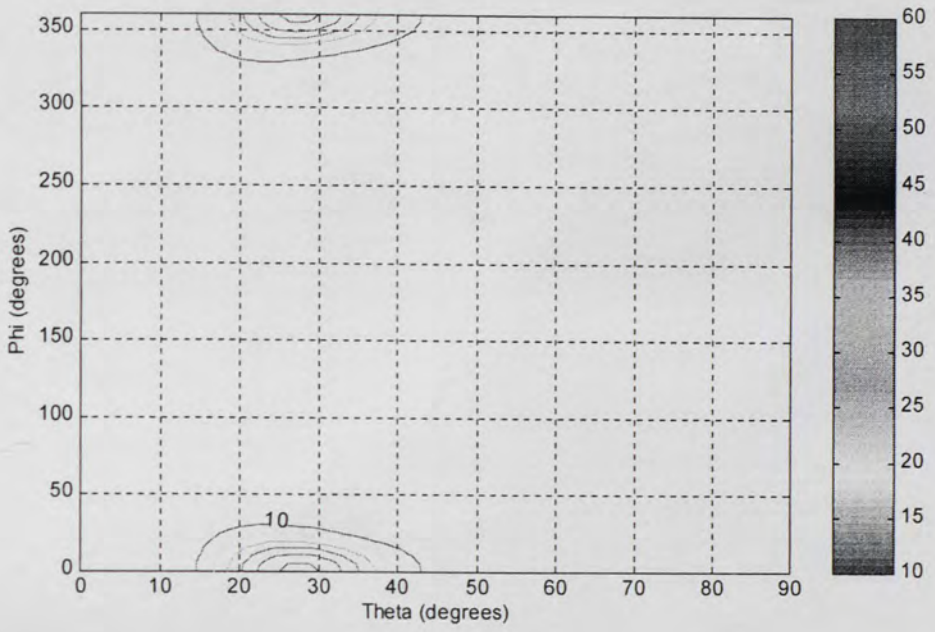

Figure 143. Gain for the Planar Array at 4.75 GHz, scan angle = 30,0.

7.3.8 Remarks

At the scan blindness angle, the reflection coefficient magnitude of an infinite array is unity. For a finite array, the reflection coefficient magnitude of the center element can actually be greater than unity, which means that the antenna is delivering power to the generator; this power of course is being transferred from other ports and does not violate any conservation laws. The reflection coefficient magnitude variation with position tends to oscillate about the corresponding value for an infinite array.

For an isolated antenna, the efficiency is constant at a specific frequency and of course, does not vary with scan angle. For arrays, however, a significant variation of efficiency occurs with scanning. The general trend is that the efficiency improves substantially for even modest sized arrays, and increases with array size at all scan angles

except those near the angle where the infinite array has blindness. At the scan blindness angle, the efficiency decreases with increasing array size since there is more surface wave power. Destructive interference of the surface wave occurs with increasing array size, except near the blindness angle. If an infinite array approximation of an array does not predict any scan blindness angle, the efficiency would be unity; the efficiency predicted by the finite array simulation would be close to unity.

As the array size increases, the pattern and gain becomes oscillatory and converge to the pattern and element gain of the infinite array. The element patterns for elements away from the center can be quite asymmetric, that is why it is so important to have a finite array simulation that, unlike the infinite array approximation, takes into consideration the edge effects [79-83].

8. CONCLUSIONS AND FUTURE RESEARCH

In this dissertation, it has been shown that the FDTD method is a very flexible and powerful simulation methodology for studying finite-sized broadband multi-layered phased array microstrip antennas. The approach allows modeling of electric conductors, inhomogeneous dielectric media and the coaxial feed.

Several validation and comparison tests have been performed to show the accuracy of the FDTD methodology. The FDTD results have been compared with measured data and in some cases with the Method of Moments.

Following is a summary of the main contributions that have been presented in the dissertation:

a) An extensive study of finite phased arrays of coax-fed stacked microstrip antennas using the Finite Difference Time Domain Method (FDTD). Rectangular and circular patches are used. The model can handle multi-layer microstrip antennas. The antennas can be bottom-fed for broadband, or upper-fed for dual-frequency applications.

b) Accurate prediction of mutual coupling between the array elements, scattering parameters, radiation patterns and the computation of the scan impedance of the array.

c) A full-time domain source excitation model for phased arrays, which renders broad band results in a single computational run.

d) Analysis of antennas with multiple coaxial feeds for dual linear and circular polarization, using a full-time domain excitation.

e) A Computer Aided Design (CAD) program has been developed, which include all the features mentioned in this dissertation. Emphasis has been placed on visualization of the results, using 3-D and 2-D graphics that are very useful to interpret the results. These developments can be used future research endeavors.

While the goal of this dissertation was to present a very detailed and complete formulation of the topics considered, it certainly does not represent a comprehensive study of the various techniques and numerical methods that can be used. Several opportunities of future research may include:

1) Implement different coaxial and microstrip feed models. Simpler feed models could reduce the computational time used for the FDTD calculations. Include the FDTD scattered-field formulation. Investigate non-orthogonal grids and non-uniform meshing. Implement the Anisotropic PML. Include dispersive and non-isotropic electric and magnetic materials.

2) Investigate Massive Parallel Processing Algorithms that can be used in the solution of time-stepping finite-difference techniques. This is a very promising arena that can reduce drastically the time used for the simulations.

3) Integrate existing CAD file formats to the FDTD program. This endeavor will be the key to model very complex and large structures.

This in no way represents a complete list of the possible research topics that can be derived from the work presented in this dissertation. However, it does provide some ideas concerning important future contributions that would be useful for phased array antennas analysis and numerical techniques for electromagnetic computations.

9. APPENDIX

Appendix A. Radiation Characteristics

Once the radiation pattern is obtained, all the radiation characteristics can be obtained using the standard relations for antennas. The total electric field is obtained from the complex-valued E_θ and E_ϕ components [2]

$$|E_{tot}| = \sqrt{|E_\theta(\theta,\phi)|^2 + |E_\phi(\theta,\phi)|^2} \tag{A.1}$$

The radiation intensity is obtained from the total field, and in the far field it can be approximated as

$$U(\theta,\phi) = \frac{1}{2\eta}\left[|E_\theta(\theta,\phi)|^2 + |E_\phi(\theta,\phi)|^2\right] \tag{A.2}$$

The total radiated power can be calculated from the knowledge of the radiation intensity,

$$P_{rad} = \int_0^{2\pi}\int_0^{\pi} U(\theta,\phi)\sin\theta d\theta d\phi \tag{A.3}$$

The directivity is obtained from the maximum radiation intensity and the radiated power,

$$D_o = \frac{4\pi U_{max}}{P_{rad}} \tag{A.4}$$

The total input power to an N-element array can be obtained assuming $V = 1$ *volt* is being fed into the port and $Z_o = 50$ *ohms* reference at the port,

$$P_{in} = \sum_{n=1}^{N} \left(1 - \left|\Gamma_{in}^{n}\right|^2\right) \frac{V^2}{2Z_o} \tag{A.5}$$

The definition of radiation efficiency does not include losses arising from impedance and polarization mismatches. It includes only conduction and dielectric losses, and it is represented by e_{cd}. The radiation efficiency is the ratio of the total power radiated by the antenna to the total power accepted by the antenna at its input terminals during radiation, therefore [84]

$$e_{cd} = \frac{P_{rad}}{P_{rad} + P_{loss}} = \frac{P_{rad}}{P_{in}} \tag{A.6}$$

In the above equation, the term P_{loss} represents the surface wave, dielectric and conductor losses. The gain can be obtained from

$$G(\theta,\phi) = 4\pi \frac{U(\theta,\phi)}{P_{in}} \tag{A.7}$$

and the maximum gain can be obtained from the above equation or from the following relations,

$$G_o = e_{cd} D_o = 4\pi \frac{U_{max}}{P_{in}} \tag{A.8}$$

The maximum effective aperture is dependent on the polarization loss, the radiation efficiency and the mismatch loss,

$$A_{em} = e_{cd}\left(1 - \left|\Gamma_{in}^{n}\right|^2\right)\frac{\lambda^2}{4\pi} D_o \left|\hat{\rho}_w \cdot \hat{\rho}_a\right|^2 \tag{A.9}$$

where the mismatch loss is obtained from $1 - \left|\Gamma_{in}^{n}\right|^2$. The polarization loss factor $\left|\hat{\rho}_w \cdot \hat{\rho}_a\right|^2$ is valid for any kind of polarization. A circular polarization loss factor can be defined as the loss that the antenna would have as a response to an incident circularly polarized wave on the antenna. It will be close to 0 dB for circularly polarized antennas and approximately –3 dB for linearly polarized antennas. This kind of loss can be obtained considering the unit vectors of the polarization of the incident wave and the polarization of the antenna

$$\hat{a}_w = \frac{\hat{a}_x \pm j\hat{a}_y}{\sqrt{2}}$$

$$\hat{a}_a = \frac{\vec{E}_a}{\left|\vec{E}_a\right|} \qquad \text{(A.10)}$$

$$\vec{E}_a = \left(|E_R| + |E_L|\right)\hat{a}_x \pm j\left(|E_R| - |E_L|\right)\hat{a}_y$$

Appendix B. Co-polarization, Cross-polarization and Axial Ratio

From the IEEE Standard definition, cross-polarization is defined as the polarization orthogonal to a reference polarization. The polarization is observed along the direction of propagation. If the polarization obeys the right hand rule for wave propagation, this type of wave is referred as right-hand; otherwise, it is referred as left-hand. If we define the reference and the cross-polarization to be what one measures when radiation patterns are measured, we can define the unit vectors $\hat{a}_{ref}$ and $\hat{a}_{cross}$ such that $\vec{E}(\theta,\phi)\cdot\hat{a}_{ref}$ is the reference polarization component of $\vec{E}$ and $\vec{E}(\theta,\phi)\cdot\hat{a}_{cross}$ is the cross polarization component of $\vec{E}$.

Therefore, the measured pattern is given by [85]

$$M(\theta) = \vec{E}(\theta,\phi)\cdot\left(sin\,\beta\hat{a}_{\theta} + cos\,\beta\hat{a}_{\phi}\right) \tag{B.1}$$

where $\vec{E}(\theta,\phi)$ is the field of the transmitting antenna, ϕ is the pattern-cut angle and β is the probe polarization angle of the reference antenna; ϕ and β are fixed for a given pattern.

If the reference antenna is polarized in the $\hat{a}_y$ direction (vertical polarization) at $\theta = 0$, this alignment procedure leads to $\beta = \phi$ for the reference polarization pattern E_{copol} and $\beta = \phi + 90^o$ for the cross polarized pattern E_{xpol} in the above equation for $M(\theta)$.

If the reference antenna is polarized in the $\hat{a}_x$ direction (horizontal polarization) at $\theta = 0$, this alignment procedure leads to $\beta = \phi + 90^o$ for the reference polarization pattern E_{copol} and $\beta = \phi$ for the cross polarized pattern E_{xpol} in the above equation for $M(\theta)$.

The cross polarization level is defined as the ratio of the maximum magnitude of E_{copol} to the maximum magnitude of E_{xpol} in a specified plane (pattern-cut angle).

$$Cross - pol = \left. \frac{|E_{copol}|_{max}}{|E_{xpol}|_{max}} \right|_{\phi = fixed} \tag{B.2}$$

Let the expression of a general plane wave propagating in a specified direction take the form

$$\begin{aligned} \vec{E} &= (E_x^+ \hat{a}_x + E_y^+ \hat{a}_y) e^{-jk_o z} \\ E_x^+ &= E_{xo}^+ e^{j\phi_x}, E_y^+ = E_{yo}^+ e^{j\phi_y} \end{aligned} \tag{B.3}$$

The following expressions can be used to determine the co-polarization and cross-polarization patterns from $\vec{E}(\theta, \phi)$

$$\begin{aligned} E_x^+ &= E_\theta(\theta, \phi) \cos\phi - E_\phi(\theta, \phi) \sin\phi \\ E_y^+ &= E_\theta(\theta, \phi) \sin\phi - E_\phi(\theta, \phi) \cos\phi \end{aligned} \tag{B.4}$$

Any plane wave of the form given in equation (B.3) can be decomposed into the sum of a right-hand circularly polarized (RHCP) and a left-hand circularly polarized (LHCP) wave,

$$\begin{aligned} \vec{E} &= RHCP + LHCP \\ RHCP &= E_{right}\left(\frac{\hat{a}_x - j\hat{a}_y}{\sqrt{2}}\right) \\ LHCP &= E_{left}\left(\frac{\hat{a}_x + j\hat{a}_y}{\sqrt{2}}\right) \end{aligned} \tag{B.5a}$$

$$\begin{aligned} E_{right} &= \frac{1}{\sqrt{2}}\left(E_x^+ + jE_y^+\right) \\ E_{left} &= \frac{1}{\sqrt{2}}\left(E_x^+ - jE_y^+\right) \end{aligned} \tag{B.5b}$$

When a wave is circularly polarized, it does not make sense to use the cross polarization level. Instead, the axial ratio AR is used. The axial ratio relates the major axis to the minor axis of the polarization ellipse. The axial ratio is positive for left-hand polarization and negative for right-hand polarization. It can be obtained in our case as follows,

$$AR = -\frac{|E_{right}| + |E_{left}|}{|E_{right}| - |E_{left}|}$$

$$AR_{dB} = 20\log(|AR|) \tag{B.6}$$

$$1 \leq |AR| \leq \infty$$

10. LIST OF REFERENCES

1. J. Gómez-Tagle, C. G. Christodoulou and P. F. Wahid, "FDTDMA v. 1.0: Phased Array Antenna Analysis Program", Final Report for Raytheon E-Systems, May 1998.
2. C. A. Balanis, "Antenna Theory", Second Edition, John Wiley & Sons Inc., 1997.
3. J. Gómez-Tagle and C. G. Christodoulou, "Extended Cavity Model Analysis of Microstrip Ring Antennas", IEEE Transactions on Antennas and Propagation, November 1997.
4. J. Gómez-Tagle, "Cavity Model Analysis of Stacked Microstrip Ring Antennas using Green's Functions", M. Sc. Thesis, UCF, July 1996.
5. J. Gómez-Tagle and C. G. Christodoulou, "Cavity Model Analysis of Stacked Microstrip Ring Antennas", IEEE AP/S International Symposium, Baltimore, Maryland, July 1996.
6. R. C. Johnson, "Antenna Engineering Handbook", Third Edition, Mc Graw Hill, 1993.
7. N. Amitay, V. Galindo and C. Wu, "Theory and Analysis of Phased Array Antennas", John Wiley, First edition, New York, 1972.
8. R. C. Hansen, "Phased Array Antennas", John Wiley & Sons, First Edition, New York, 1998.

9. R. J. Mailloux, "Phased Array Antenna Handbook", Artech House, First Edition, Boston, 1994.

10. A. A. Oliner and G. H. Knittel, "Proceedings of the 1970 Phased Array Antenna Symposium", Artech House, Boston, 1970.

11. D. M. Pozar and D. H. Schaubert, "Microstrip Antennas", IEEE Press, Piscataway, N. J., 1995.

12. P. Bhartia, K. rao and R. S. Tomar, "Millimeter-Wave Micrsotrip and Printed Circuit Antennas", Artech House, First Ed., Boston, 1991.

13. K. R. Carver, "Microstrip Antenna Technology", IEEE Trans. Antennas Prop., vol. AP-29, no. 1, Jan. 1981.

14. D. M. Pozar, "Microstrip Antennas", IEEE Proc., pp. 79-91, vol. 80, no. 1, Jan. 1992.

15. S. A. Long, "A Dual-Frequency Stacked Circular Disc Antenna", IEEE Trans. Antennas Prop., pp. 270-273, vol. AP-27, no. 2, Mar. 1979.

16. K. S. Kunz and R. J. Luebbers, "The Finite Difference Time Domain Method for Electromagnetics", First Edition, CRC Press Inc., 1993.

17. A. Taflove, "Computational Electrodynamics: The Finite Difference Time Domain Method", First Edition, Artech House Inc., 1995.

18. K. S. Yee, "Numerical Solution of Initial Boundary Value Problems involving Maxwell's Equations in Isotropic Media", IEEE Trans. Antennas Prop., vol. 14, no. 5, pp. 302 – 307, May 1966.

19. A. Taflove, "Advances in Computational Electrodynamics: The Finite Difference Time Domain Method", Artech House Inc., 1998.

20. D. M. Sullivan, "Frequency Dependent FDTD Methods Using Z Transforms", IEEE Trans. Antennas Prop., vol. 40, no. 10, pp. 1223 – 1230, Oct. 1992.

21. J. Gómez-Tagle and C. G. Christodoulou, "FDTD Analysis of Stacked Microstrip Ring Antennas", IEEE AP/S International Symposium, Montreal, Canada, July 1997.

22. A. Reineix and B. Jecko, "Analysis of Microstrip Patch Antennas Using Finite Difference Time Domain Method", IEEE Trans. Antennas Prop., vol. 37, no. 11, pp. 1361 – 1369, Nov. 1989.

23. D. Sheen et al, "Application of the Three Dimensional Finite Difference Time Domain Method to the Analysis of Planar Microstrip Circuits", IEEE Trans. Microwave Theory Tech., vol. 38, no. 7, pp. 849 – 857, July 1990.

24. X. Zhang and K. K. Mei, "Time-Domain Finite Difference Approach to the Calculation of the Frequency Dependent Characteristics of Microstrip Discontinuities", IEEE Trans. Microwave Theory Tech., vol. 36, no. 12, pp. 1775 – 1787, Dec. 1988.

25. J. Fang and D. Xeu, "Numerical Error in the Computation of Impedances by FDTD Method and Ways to Eliminate Them", IEEE Microwave Guided Wave Letters, vol. 5, no. 1, pp. 6 – 8, Jan. 1995.

26. C. G. Christodoulou, J. Gómez-Tagle and J. Zalewsky, "A Note on MPI Applied to Electromagnetic Calculations", Informatica International Journal of Computing, December 1998.

27. R. J. Luebbers and H. S. Langdon, "A Simple Feed Model that Reduces Time Steps Needed for FDTD Antenna and Microstrip Calculations", IEEE Trans. Antennas Prop., vol. 44, no. 7, pp. 1000 – 1005, July 1996.

28. M. A. Jensen and Y. Rahmat-Samii, "Performance Analysis of Antennas for Hand-Held Transceivers Using FDTD", IEEE Trans. Antennas Prop., vol. 42, no. 8, pp. 1106 – 1113, Aug. 1994.

29. C. Wu et al, "Modelling of Coaxial-Fed Microstrip Patch Antenna by Finite Difference Time Domain Method", Electronics Letters, vol. 27, no. 19, pp. 1691 – 1692, Sep. 1991.

30. C. Wu et al, "Accurate Characterization of Planar Printed Antennas Using Finite Difference Time Domain Method", IEEE Trans. Antennas Prop., vol. 40, no. 5, pp. 526 – 534, May 1992.

31. G. Mur, "Absorbing Boundary Conditions for the Finite Difference Approximation of the Time Domain Electromagnetic Field Equations", IEEE Trans. Electromagnetic Compat., vol. 23, no. 4, pp. 377 – 382, Nov. 1981.

32. J. P. Berenger, "A Perfectly Matched Layer for the Absorption of Electromagnetic Waves", Journal Comp. Physics, vol. 114, pp. 185 – 200, 1994.

33. J. P. Berenger, "Perfectly Matched Layer for the FDTD Solution of Wave Structure Interaction Problems", IEEE Trans. Antennas Prop., vol. 44, no. 1, pp. 110 – 117, Jan. 1996.

34. J. P. Berenger, "Improved PML for the FDTD Solution of Wave Structure Interaction Problems", IEEE Trans. Antennas Prop., vol. 45, no. 3, pp. 466 – 473, Mar. 1997.

35. D. T. Prescott, "Reflection Analysis of FDTD Boundary Conditions – Part I: Time Space Absorbing Boundaries", IEEE Trans. Antennas Prop., pp. 1162-1170, vol. 45, no. 8, Aug. 1997.

36. D. T. Prescott, "Reflection Analysis of FDTD Boundary Conditions – Part II: Berenger's PML Absorbing Layers", IEEE Trans. Antennas Prop., pp. 1171-1178, vol. 45, no. 8, Aug. 1997.

37. D. S. Katz et al, "Validation and Extension to Three Dimensions of the Berenger PML Absorbing Boundary Condition for FDTD Meshes", IEEE Microwave Guided Wave Letters, vol. 4, no. 8, pp. 268 – 270, Aug. 1994.

38. S. D. Gedney, "An Anisotropic PML Absorbing Media for the FDTD Simulation of Fields in Lossy and Dispersive Media", Electromagnetics, vol. 16, pp. 399 – 415, 1996.

39. S. D. Gedney, "An Anisotropic Perfectly Matched Layer Absorbing Medium for the Truncation of FDTD Lattices", IEEE Trans. Antennas Prop., vol. 44, no. 12, pp. 1630 – 1639, Dec. 1996.

40. R. J. Luebbers et al, "A Finite-Difference Time-Domain Near Zone to Far Zone Transformation", IEEE Trans. Antennas Prop., vol. 39, no. 4, pp. 429 - 433, April 1991.

41. R. Luebbers et al, "A Two Dimensional Time Domain Near Zone to Far Zone Transformation", IEEE Trans. Antennas Prop., vol. 40, no. 7, pp. 848 – 851, Jul. 1992.

42. J. G. Maloney et al, "Accurate Computation of the Radiation from Simple Antennas Using the Finite Difference Time Domain Method", IEEE Trans. Antennas Prop., vol. 38, no. 7, pp. 1059 – 1068, Jul. 1990.

43. P. A. Tirkas and C. A. Balanis, "Finite Difference Time Domain Method for Antenna Radiation", IEEE Trans. Antennas Prop., vol. 40, no. 3, pp. 334 – 340, Mar. 1992.

44. R. J. Luebbers, "FDTD Calculation of Wide Band Antenna Gain and Efficiency", IEEE Trans. Antennas Prop., vol. 40, no. 11, pp. 1403 – 1407, Nov. 1992.

45. R. Luebbers et al, "FDTD Calculation of Radiation Patterns, Impedance, and Gain for a Monopole Antenna on a Conducting Box", IEEE Trans. Antennas Prop., vol. 40, no. 12, pp. 1577 – 1583, Dec. 1992.

46. T. Martin, "An Improved Near to Far Zone Transformation for the Finite Difference Time Domain Method", IEEE Trans. Antennas Prop., pp. 1263-1271, vol. 46, no. 9, Sept. 1998.

47. J. Huang, "Circularly Polarized Conical Patterns from Circular Microstrip Antennas", IEEE Trans. Antennas Prop., vol. 32, no. 9, pp. 991-994, Sep. 1984.

48. J. T. Aberle and D. M. Pozar, "Analysis of Infinite Arrays of One and Two-Probe Fed Circular Patches", IEEE Trans. Antennas Prop., vol. 38, pp. 421-432, no. 4, April 1990.

49. J. Gómez-Tagle, C. G. Christodoulou and P. F. Wahid, "Mutual Coupling and Active Impedance Analysis of Finite Phased Array Microstrip Antennas", URSI/IEEE International Symposium, Thessaloniki, Greece, May 1998.

50. A. N. Tulintseff et al, "Input Impedance of a Probe-Fed Stacked Circular Microstrip Antenna", IEEE Trans. Antennas Prop., pp. 381-390, vol. 39, no. 3, Mar. 1991.

51. T. R. Holzheimer and T. O. Miles, "Broadband Microstrip Phased Array", E-Systems Inc., Technical Report

52. T. O. Miles, "Broadband Microstrip Antenna Element", E-Systems Inc., Technical Report.

53. J. Gómez-Tagle, C. G. Christodoulou and P. F. Wahid, "Mutual Coupling Analysis of Finite Phased Array Microstrip Antennas", SouthEastCon, Orlando, Florida, May 1998.

54. J. Gómez-Tagle, C. G. Christodoulou and P. F. Wahid, "Active Impedance Analysis of Finite Phased Array Microstrip Antennas", IEEE AP/S International Symposium, Atlanta, Georgia, July 1998.

55. J. Gómez-Tagle, C. G. Christodoulou and P. F. Wahid, "Modeling of Broadband Finite Sized Phased Array Antennas", IEEE AP/S International Symposium on Antennas for Wireless Communications, Boston, Massachusetts, November 1998.

56. J. Gómez-Tagle, C. G. Christodoulou and P. F. Wahid, "Time Domain Simulation of Circularly Polarized Phased Array Microstrip Antennas", to be presented in IEEE AP/S International Symposium, Orlando, Florida, July 1999.

57. J. Gómez-Tagle, C. G. Christodoulou and P. F. Wahid, "FDTD Analysis of Finite-Sized Phased Array Microstrip Antennas", UCF, June 1998.

58. R. P. Jedlicka et al, "Measured Mutual Coupling Between Microstrip Antennas", IEEE Trans. Antennas Prop., vol. 29, no. 1, pp. 147 – 149, Jan. 1981.

59. D. M. Pozar, "Input Impedance and Mutual Coupling of Rectangular Microstrip Antennas", IEEE Trans. Antennas Prop., vol. 30, no. 6, pp. 1191 – 1196, Nov. 1982.

60. R. Luebbers and K. Kunz, "Finite Difference Time Domain Calculations of Antenna Mutual Coupling", IEEE Trans. Electromagnetic Compatibility, vol. 34, no. 3, pp. 357 – 359, Aug. 1992.

61. K. Fujimoto and J. R. James, "Mobile Antenna Systems Handbook", First Edition, Artech House Inc., 1994.

62. R. Telikepalli et al, "Wide Band Microstrip Phased Array for Mobile Satellite Communications", IEEE Trans. Microwave Theory Tech., vol. 43, no. 7, pp. 1758 – 1763, July 1995.

63. K. Ogawa and T. Uwano, "A Diversity Antenna for Very Small 800-MHz Band Portable Telephones", IEEE Trans. Antennas Prop., vol. 42, no. 9, pp. 1342 – 1345, Sep. 1994.

64. T. S. Rappaport, "Wireless Communications: Principles and Practice", First Edition, Prentice Hall Inc., 1996.

65. J. Huang and A. C. Densmore, "Microstrip Yagi Array Antenna for Mobile Satellite Vehicle Application", IEEE Trans. Antennas Prop., vol. 39, no. 7, Jul. 1991.

66. M. F. Pasik, "Application of the PML Absorbing Boundary Condition to the Analysis of Patch Antennas", Electromagnetics Journal, vol. 16, pp. 435 – 449, 1996.

67. G. M. Turner, "Phased Array Antenna Analysis using the Finite Difference Time Domain Method", Ph. D. Dissertation, University of Central Florida, Dec. 1997.

68. K. H. Lee and S. R. Laxpati, "FDTD Analysis of an Inifinite Array of Microstrip Patches", IEEE AP-S Int. Symp. Dig., pp. 1284 – 1287, Jul. 1996

69. P. Harms et al, "Implementation of the Periodic Boundary Condition in the Finite Difference Time domain Algorithm for FSS Structures", IEEE Trans. Antennas Prop., vol. 42, no. 9, pp. 1317 – 1324, Sep. 1994.

70. A. C. Cangellaris et al, "A Hybrid Spectral/FDTD Method for the Electromagnetic Analysis of Guided Waves in Periodic Structures", IEEE Microwave Guided Wave Letters, vol. 3, no. 10, pp. 375 – 377, Oct. 1993.

71. J. Ren et al, "Floquet Based FDTD Analysis of Two Dimensional Phased Array Antennas", IEEE Microwave Guided Wave Letters, vol. 4, no. 4, pp. 109 – 111, Apr. 1994.

72. D. T. Prescott and N. V. Shuley, "Extensions to the FDTD Method for the Analysis of Infinitely Periodic Arrays", IEEE Microwave Guided Wave Letters, vol. 4, no. 10, pp. 352 – 354, Oct. 1994.

73. A. Alexanian et al, "Three Dimensional FDTD Analysis of Quasi Optical Arrays Using Floquet Boundary Conditions and Berenger's PML", vol. 6, no. 3, pp. 138 – 140, Mar. 1996.

74. G. M. Turner and C. G. Christodoulou, "FDTD Analysis of Periodic Phased Array Antennas", to be published IEEE Trans. Antennas Prop.

75. D. M. Pozar, "Analysis of Finite Phased Arrays of Printed Dipoles", IEEE Trans. Antennas Prop., vol. 33, no. 10, pp. 1045-1053, Oct. 1985.

76. D. M. Pozar, "Finite Phased Arrays of Rectangular Microstrip Patches", IEEE Trans. Antennas Prop., vol. 34, no. 5, pp. 658-665, May 1986.

77. K. Uehara and K. Kagoshima, "Rigorous Analysis of Microstrip Phased Array Antennas using a new FDTD Method", Electronics Letters, vol. 30, no. 2, pp. 100 – 101, Jan. 1994.

78. D. Crouch, "On the Use of Symmetry to Reduce the Computational Requirements for FDTD Analyses of Finite Phased Arrays", Microwave Opt. Tech. Letters, vol. 13, no. 3, pp. 123 – 128, Oct. 1996.

79. D. M. Pozar, "Considerations for Millimeter Wave Printed Antennas", IEEE Trans. Antennas Prop., vol. AP-31, pp. 740-747, no. 5, Sept. 1983.

80. D. M. Pozar, "Scan Blindness in Infinite Phased Arrays of Printed Dipoles", IEEE Trans. Antennas Prop., IEEE Trans. Antennas Prop., vol. AP-32, pp. 602-610, no. 6, June 1984.

81. D. M. Pozar and D. H. Schaubert, "Analysis of an Infinite Array of Rectangular Microstrip Patches with Idealized Probe Feeds", IEEE Trans. Antennas Prop., vol. AP-32, pp. 1101-1107, no. 10, October 1984.

82. C. Liu et al, "Performance of Probe-Fed Microstrip-Patch Element Phased Arrays", IEEE Trans. Antennas Prop., vol. AP-36, pp. 1501-1509, Nov. 1988.

83. B. Jang et al, "Analysis of Finite-Phased Arrays of Aperture-Coupled Stacked Microstrip Antennas", IEEE Trans. Antennas Prop., vol. 45, pp. 1201-1204, no. 8, Aug. 1997.

84. E. H. Newman, "Two Methods for the Measurement of Antennas Efficiency", IEEE Trans. Antennas Prop., pp. 457-461,vol. 23, no. 4, July 1975.

85. A. C. Ludwig, "The definition of Cross Polarization", IEEE Trans. Antennas Prop., vol. AP-21, pp. 116-119, Jan. 1973.

86. R. J. Luebbers and K. Kunz, "FDTD Modeling of Thin Impedance Sheets", IEEE Trans. Antennas Prop., vol. 40, no. 3, pp. 349 – 351, Mar. 1992.